Development of Highly Reliable Plasma Discharge Devices with (Mg,Ca)O Protective Layers

Takeda, Eiji

(Degree)
博士（工学）

(Date of Degree)
2019-09-25

(Date of Publication)
2020-09-01

(Resource Type)
doctoral thesis

(Report Number)
甲第7602号

(URL)
https://hdl.handle.net/20.500.14094/D1007602

博　士　論　文

Development of Highly Reliable Plasma Discharge Devices with (Mg,Ca)O Protective Layers

(Mg,Ca)O 保護膜を用いたプラズマ放電デバイスの信頼性向上に関する研究

令和元年7月

神戸大学大学院工学研究科

武　田　　英　治

Doctoral Dissertation

博士論文

Development of Highly Reliable Plasma Discharge Devices with (Mg,Ca)O Protective Layers

(Mg,Ca)O 保護膜を用いたプラズマ放電デバイスの信頼性向上に関する研究

July, 2019

令和元年7月

Graduate School of Engineering, Kobe University

神戸大学大学院工学研究科

Eiji Takeda

武田 英治

Contents

Chapter 1

General Introduction **1**

1.1 Ultraviolet Radiation by Xe Discharge 1

1.2 Plasma Discharge Device with Xe Gas 3

1.2.1 Principle of Operation 3

1.2.2 Display Applications 6

1.2.3 Lighting Applications 8

1.2.4 Chemical and Biological Applications 8

1.3 Improvement of Energy Efficiency 10

1.4 Electron Emission from Dielectric Cathode Layer 12

1.5 High-γ Material for Dielectric Cathode Layer 15

1.6 Complex Oxide Cathode Layer with High γ 16

1.6.1 SrO-based Oxide 16

1.6.2 CaO-based Oxide 17

1.6.3 MgO-based Oxide 19

1.7 (Mg,Ca)O Protective Layer 21

1.8 Chapter Overview and Goals of This Thesis 25

References 27

Chapter 2

Annealing process for recovery of carbonated (Mg,Ca)O protective layer for plasma discharge device **45**

2.1 Introduction 46

2.2 Experimental Methods 47

2.3 Results and Discussion 51

2.4 Conclusions 64

References 66

Chapter 3

Shrinkage and expansion of discharge area by (Mg,Ca)O protective layer for plasma discharge device **71**

3.1 Introduction 72

3.2 Experimental Methods 73

3.3 Results and Discussion 75

3.4 Conclusions 92

References 94

Chapter 4

Degradation of phosphor excitation efficiency by adsorption of organic compounds on phosphors by VUV irradiation **101**

4.1 Introduction 102

4.2 Experimental Methods 103

4.3 Results and Discussion 104

4.4 Conclusions 111

References 112

Chapter 5

Degradation of phosphor excitation efficiency by re-deposition of the sputtered protective layer on the phosphors **115**

5.1 Introduction 116

5.2 Experimental Methods 117

5.3 Results and Discussion 119

5.4 Conclusions 135

References 136

Chapter 6

Overall Conclusion **141**

Acknowledgments **145**

List of Achievements **147**

Chapter 1

General Introduction

1.1 Ultraviolet Radiation by Xe Discharge

Glow discharge by Hg vapor was frequently used as a ultraviolet (UV) light source in the past. Hg discharge provides high UV emission and a high UV radiation generation efficiency, leading to wide-spreading applications to lighting units by wavelength conversion from UV to visible light with internal phosphors [1]. However, deleterious effects to human health and global environment by Hg released from the fluorescent lamps would be an serious problem to be solved [2].

As a recent international trend for restricting a use of Hg, the United Nations treaty 'The Minamata Convention on Mercury' was adopted on October 10, 2013 in Kumamoto, Japan and entered into force on August 16, 2017 to prevent anthropogenic emissions and releases of Hg and its compounds for sustainable global environment and human health. Until now, 128 countries signed the convention and 110 countries ratified it [3]. The aim of this convention is the complete abolition of manufacturing, importation, and exportation of Hg-used products until 2020, which currently urges countries all over the world to promptly develop and expand the use of Hg-free products.

During the past decade, light emitting diodes (LEDs) have commonly been used as a Hg-free light source. LEDs have a high luminous efficiency (over 100 lm/W) and a long lifespan (over

100,000 h) [4], but they are still expensive for the complete substitution and difficult to be used in a large size. Therefore, dielectric barrier discharge (DBD) by noble gas plasma is much attracted as such applications because plasma discharge devices have significant size expansion potential and could be fabricated at a reasonable production cost [5]. Among noble gases, Xe is often employed for the following reasons; (1) a high UV radiation generation efficiency, (2) UV radiation at long wavelength for low phosphor damages and a high wavelength conversion efficiency, and (3) low visible radiation for suppression of color mixing with phosphor emission [6]. Figure 1.1 shows the example of Xe emission spectra in a UV region at various pressures of discharge gas [7]. Xe discharge can generate vacuum UV (VUV) emission mainly at 147 and 173 nm. The sharp peak at 147 nm results from the transition from the Xe resonance level $Xe_r^*(^3P_1)$ to the ground state, while the broad peak at 173 nm arises from the excited molecular dimers $Xe_2^*(^1\Sigma_u^+)$ and $Xe_2^*(^3\Sigma_u^+)$ [8,9]. The 147 nm to 173 nm emission ratio is modified by varying a pressure or a Xe density in discharge gas. The mixture of Xe and halogen gas makes the UV emission peak-narrower and wavelength-longer [7], but halogen gases are harmful in common with Hg. Thus, it is required to use the discharge only by noble gas plasma for the realization of a human- and environment-friendly device.

The problem to use Xe discharge compared with Hg discharge is a UV radiation generation efficiency. Figure 1.2 shows a comparison of luminous efficiencies of Hg or Xe discharge fluorescent lamps having the similar electrode configurations [6]. In Xe discharge, a Xe atom at a ground state absorbs the radiations arising from the relaxation of nearby excited Xe. Furthermore, excited Xe can be deactivated by collisions with free electrons. Due to these self-absorption and de-excitation phenomena, the luminous efficiency by Xe discharge is less than that by Hg discharge and saturated at a high discharge current density. Therefore, the enhancement of a UV radiation generation efficiency in Xe discharge devices is highly demanded to

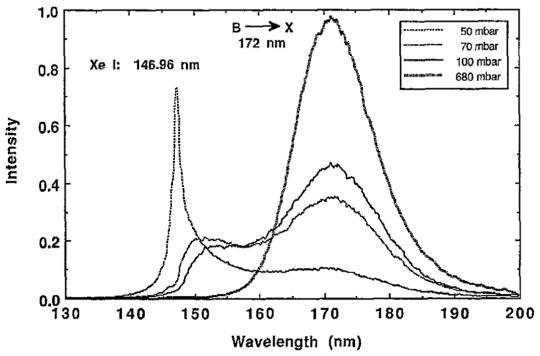

Figure 1.1: Emission spectra from Xe discharge in a UV region at various pressures of discharge gas [7].

compete with Hg discharge devices as well as with LEDs.

1.2 Plasma Discharge Device with Xe Gas

1.2.1 Principle of Operation

Various practical devices using Xe plasma have already been developed, as examples of not only cylindrical fluorescent lamps but also flat panel plasma discharge devices such as plasma displays, planar lighting fixtures, and large-sized sterilization, purification, and medical units. In this section, the common operational principle is described and then the recent researches and developments for these flat panel devices are introduced.

Figures 1.3(a)-1.3(c) illustrate the schematics of operational behaviors in flat panel plasma discharge devices in the 1st, 2nd, and 3rd steps, respectively. Firstly, Xe planar discharge is

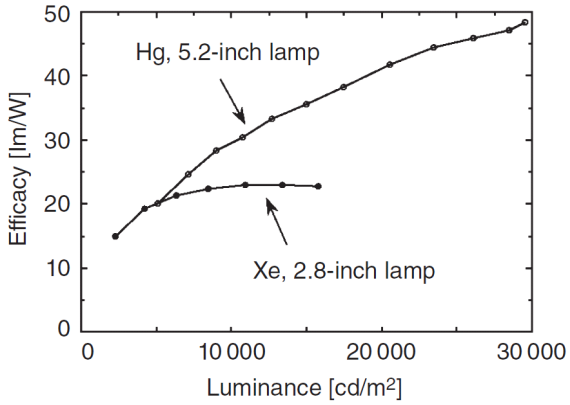

Figure 1.2: Comparison of luminous efficiencies of fluorescent lamps having the similar electrode configurations by Hg or Xe discharge [6].

generated by applying a sufficient voltage to coplanar electrodes and then VUV light is radiated from the Xe discharge, as illustrated in Fig. 1.3(a). An electron emission from a dielectric cathode layer plays an important role in firing and sustaining the discharge. Appropriate pressure and buffer gas species in discharge gas are also significant issues to generate the efficient discharge and VUV radiation. Ne or Ar is often added as buffer gas to reduce a discharge voltage by the Penning effect [10]. Secondly, internal phosphors are excited by VUV, and visible, near UV (NUV), or deep UV (DUV) light is emitted from the phosphors, as illustrated in Fig. 1.3(b). Main issues in this step are a phosphor excitation efficiency by VUV and a quantum luminescence efficiency of phosphors. Lastly, light emission from the phosphors is extracted out of the device, as illustrated in Fig. 1.3(c). In this step, an aperture ratio of the device structure, transmittance of the panel at the emission side, and reflectance of the panel at the opposite side are key considerations.

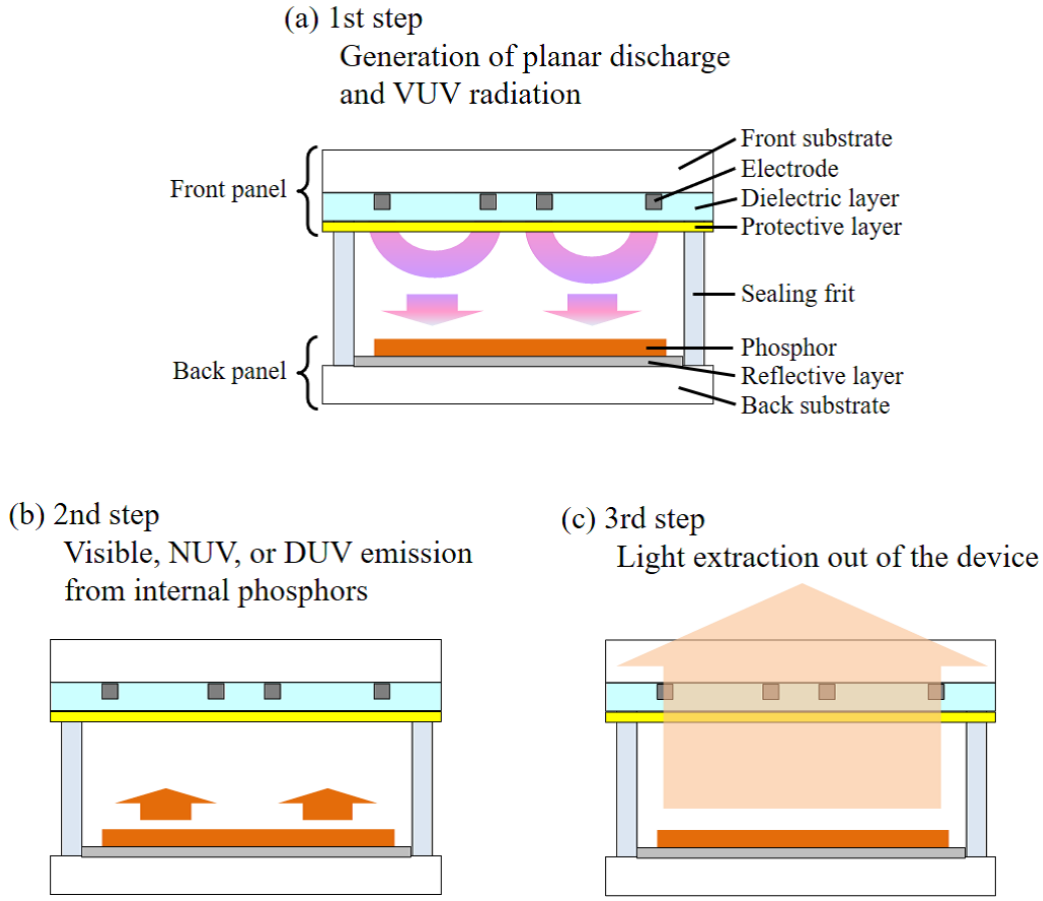

Figure 1.3: Schematics of operational behaviors of flat panel plasma discharge devices with Xe planar discharge. (a) In the 1st step, Xe discharge is generated by applying a voltage to coplanar electrodes and then VUV light is radiated from the Xe discharge. (b) In the 2nd step, internal phosphors are excited by VUV, and visible, NUV, or DUV light is emitted from the phosphors. (c) In the 3rd step, light emission from the phosphors is extracted out of the device.

1.2.2 Display Applications

A plasma display panel (PDP) is one of the most widespread applications of Xe DBD [11-13]. Since the PDP invention at the University of Illinois in 1964 [14], the specifications such as a luminous efficiency, luminance, definition, and size expansion have dramatically been improved. Not only 42-inch full-high definition (FHD) PDPs [15,16] but also 103-inch FHD [17], 150-inch 4K2K [18], and 145-inch 8K4K PDPs (shown in Fig. 1.4(a)) [19] were demonstrated. Moreover, curved and super-large-sized displays up to 180-inch panels for ambient applications of digital signages were realized by a plasma tube array (PTA) technology as shown in Fig. 1.4(b) [20]. PDPs are good at size expansion, image quality, color reproducibility, and moving picture resolution [12,21], but one of the weak points is a luminous efficiency (up to 5 lm/W) [12]. The lifespans of PDPs are reported to 30,000 $\sim$ 100,000 h [22]. Flexible transparent plasma displays have also been demonstrated, which will create new display applications available in any situation in the future [23-25].

One of the recent applications of a PDP technology is a plasma panel sensor (PPS) for radioactive detection [26]. The detection of radiation is based on modification of the discharge firing due to partial ionization of discharge gas induced by incident radiation. Merits of a PPS compared with a conventional radiation sensor are potentials of cost-lowering, portability (no cooling systems), size expansion, and constant monitoring of a spatial distribution of radioactive contamination. Friedman *et al*. carried out the pioneering work of a PPS with a direct current (DC) PDP technology in 2005 [27]. The PPS technology has demonstrated the detection of not only X-ray [28,29] but also β-ray, γ-ray, muon, proton, and neutron [30-32]. Except for a DC-type, a PPS with an alternating current (AC) PDP technology was recently developed [33], which will open affordable PPS applications for simple inspection of hot spots and distributed foods having radioactive contamination because an AC-type PDP has substantially

Figure 1.4: Photographs of super large-sized PDPs; (a) 145-inch 8K4K PDP [19] and (b) curved 180-inch PTA [20].

been developed and widely been commercialized.

1.2.3 Lighting Applications

A plasma flat lamp (PFL) emitting visible light is an interest of this subsection because of a great advantage of size expansion potential for flat panel plasma discharge devices against LEDs. Since the pioneering proposal of a flat fluorescent lamp with Xe DBD by Urakabe *et al.* in 1996 [34], many groups have improved the PFLs with high luminance and a high luminous efficiency even in the 2010s [35-37]. Oh *et al.* demonstrated the greatly improved luminance (up to 22100 cd/m^2) and luminous efficiency (up to 94 lm/W) by optimizing the electrode configuration [38]. The lifespan of PFLs reaches $\sim$ 100,000 h [5]. The first application of PFLs was a backlight for a liquid crystal display [6,39], but in recent years, general lighting systems using Xe planar discharge, such as interior lights, outdoor billboards and illuminations, emergency lights of crowd area, architectural lighting installations, and airport lighting systems, have been industrialized [40]. The flexible PFLs have also been developed [41], which will lead to upcoming unique lighting applications with a high degree of freedom of design and installation.

1.2.4 Chemical and Biological Applications

VUV emission from plasma discharge devices is often used for photodissociation of compounds because the light whose wavelength is shorter than approximately 200 nm is required to break the chemical bonds of strongly bound molecules [5]. O_3 generation and the decomposition of organic compounds by VUV irradiation have been applied to the surface cleaning of a substrate, surface modification for functionalization, disinfection, and odor eliminating for a

long time [42]. Recently, Zukawa *et al*. demonstrated the higher decomposition ability of an organic dye using VUV radiation by a planar Xe DBD device than by a conventional excimer lamp [43]. By employing phosphors emitting at NUV or DUV, UV PFLs have also been developed, and the diligent researches and developments on chemical and biological applications have been performed in recent years. In a sterilization purpose, the frequently-used region in wavelength is UVC, which effectively destroys the deoxyribonucleic acid (DNA) of harmful viruses and bacteria [44]. Zukawa *et al*. developed a plate-type UVC light source with MgO phosphors and demonstrated the effective virus inactivation comparable to that of a conventional Hg lamp [45]. Awamoto *et al*. demonstrated the effective bacteria inactivation using a luminous array film (LAFi) with broadband UVC phosphors [46]. These sterilization and disinfection effects without chemical substances by plasma discharge devices can be applied to cleaning water [47,48], air, foods [49], and facilities [50] in a large area even by single irradiation.

In a medical application, narrow band (NB) UVB light is used for skin phototherapy. The phototherapy effects have a strong dependence on irradiation wavelength and are most enhanced at approximately 300 nm, while erythema reactions due to skin damages induced by UV irradiation is enhanced as the radiated wavelength is shorter than approximately 310 nm [51,52]. Thus, NB UVB at approximately 300 to 310 nm is often employed for low erythema reaction and effective phototherapy. Morita *et al*. proposed the flat-type and portable NB UVB device by employing $YAl_3(BO_3)_4$:Gd^{3+} phosphors emitting at 312 nm for psoriasis treatment [53]. Guo and Awamoto *et al*. demonstrated the area-selectable NB UVB light source with Gd-doped UVB phosphors emitting at 311 nm for skin phototherapy by a LAFi technology [54,55]. It is also demonstrated that the fertility of animals and the growth of plants are enhanced by UVB irradiation [56]. Besides the above-mentioned developments, numerous applications in various fields with the photophysical, photochemical, and photobiological effects by plasma discharge

Figure 1.5: Photograph of a skin phototherapy system with UV LAFi emitting at 311 nm NB UVB [54].

devices have currently been studied, which are reviewed in Refs. [42,57,58].

1.3 Improvement of Energy Efficiency

As described in Section 1.1, enhancement of an energy efficiency of plasma discharge devices is strongly required to replace Hg discharge devices with Xe discharge devices. In this section, the energy efficiency of each operational step in Xe plasma discharge devices is discussed based

Table 1.1: Estimated energy balance in PDP operation with Ne:Xe mixed discharge gas [12]. The percentage of the dissipated energy at each step indicated in the fist column with respect to the total energy applied to the panel is presented in the second column, while the percentage of the energy loss between the successive steps described in the fist column is given in the third column.

Energy	%	Loss
Electric energy dissipated in discharge	100	
	↓	60% in ion heating (from models)
Energy dissipated in electron heating	$\rho = 40$	
	↓	50% in xenon ionization, neon excitation and ionization (from models)
Energy dissipated in xenon excitation	$\eta_{Xe} = 20$	
	↓	25% transition loss (e.g. infrared emission), quenching (from models)
Energy dissipated in UV production	$\eta_{UV} = 15$	
	↓	50% VUV photons not collected by phosphors (estimation)
UV energy reaching the phosphors	7.5	
	↓	67% UV to visible photon energy conversion loss (estimation)
Visible photons production	2.5	
	↓	40% visible photons not collected on front face (estimation)
Photons reaching the user	1.5	

on the example of a PDP as a model Xe DBD device. Table 1.1 shows the approximate energy balance in the PDP operation with Ne:Xe mixed discharge gas estimated by Boeuf [12]. Although the estimation can be applied only in a limited situation and modified in the case of other plasma discharge devices due to a different device dimension, the values in Table 1.1 help us to understand the key factors to improve the energy efficiency. Large energy losses are evident even at the early stages of the device operation such as ion or electron heating and Ne or Xe excitation.

If it is assumed that DC glow discharge where ionization takes place by the negative glow whose field is zero for a simplified discussion, the energy fractions dissipated to ion and elec-

tron heating in the sheath with respect to total heating of electrons and ions can be expressed approximately as $1/(1+\gamma)$ and $\gamma/(1+\gamma)$, respectively, where γ is an ion-induced secondary electron emission coefficient of a cathode layer [59]. Thus, increasing γ leads to decreasing ion heating and naturally increasing electron heating, resulting in the improvement of the energy efficiency of plasma discharge devices. Therefore, a dielectric electron emitter with high γ must be a key material to realize plasma discharge devices with a high energy efficiency by increasing electron heating.

Another approach to enhance the efficiency is increasing a Xe content in Ne:Xe mixed discharge gas. As shown in Fig. 1.6, the luminous efficiency of a plasma discharge device increases as the Xe content increases due to the enhancement of VUV radiation generation [60-62]. However, increasing a Xe content also leads to the increase of the discharge firing voltage [60-62], which depends strongly on γ of a cathode layer [63]. Thus, a dielectric electron emitter with high γ also plays an important role in realizing both an increased luminous efficiency and a decreased discharge voltage.

1.4 Electron Emission from Dielectric Cathode Layer

In order to improve the energy efficiency of plasma discharge devices, development of a dielectric electron emitter with high γ is essential as described in Section 1.3. To protect the electrode and dielectric layer against sputtering by discharge, an oxide protective layer is formed at the surface of the dielectric layer in plasma discharge devices. MgO is commonly used as the protective layer because of its relatively high electron emission property, chemical stability, and resistance against sputtering by discharge [12]. MgO with (111) preferred orientation shows the highest γ among the possible crystal structures due to the negative electron affinity of the (111) surface [64]. An electron emission from MgO can be explained by the Auger neutralization

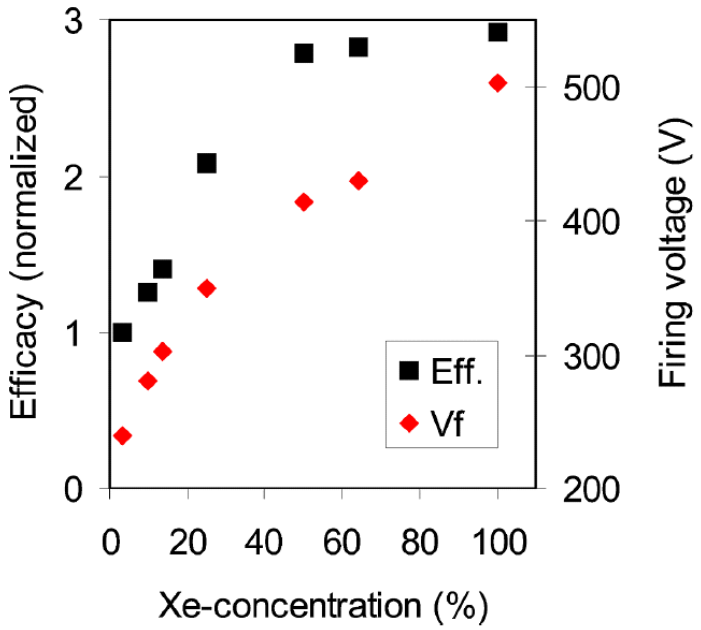

Figure 1.6: Luminous efficiencies and discharge firing voltages of plasma discharge devices as a function of a Xe content [61]. The data of the luminous efficiencies are normalized with respect to the value obtained by 3.5% Xe content trial.

process [65,66]. Figure 1.7 shows a schematic energy diagram of the electron emission processes from bulk MgO by the Auger neutralization with Ne^+ and Xe^+. The wide band gap for bulk MgO indicates that an electron emission is effective via Ne^+, but not via Xe^+. However, the band gap at the surface in a thin film is reduced owing to crystal structure imperfections, which generate extra states near the band edges and then narrow the band gap at the surface as shown in Fig. 1.8 [67,68]. Therefore, an electron emission from the surface states of MgO can be slightly effective, even for Xe^+. In addition, F-type centers which act as deep electron traps are created in MgO due to oxygen vacancies. The F-type centers at the ground state are lo-

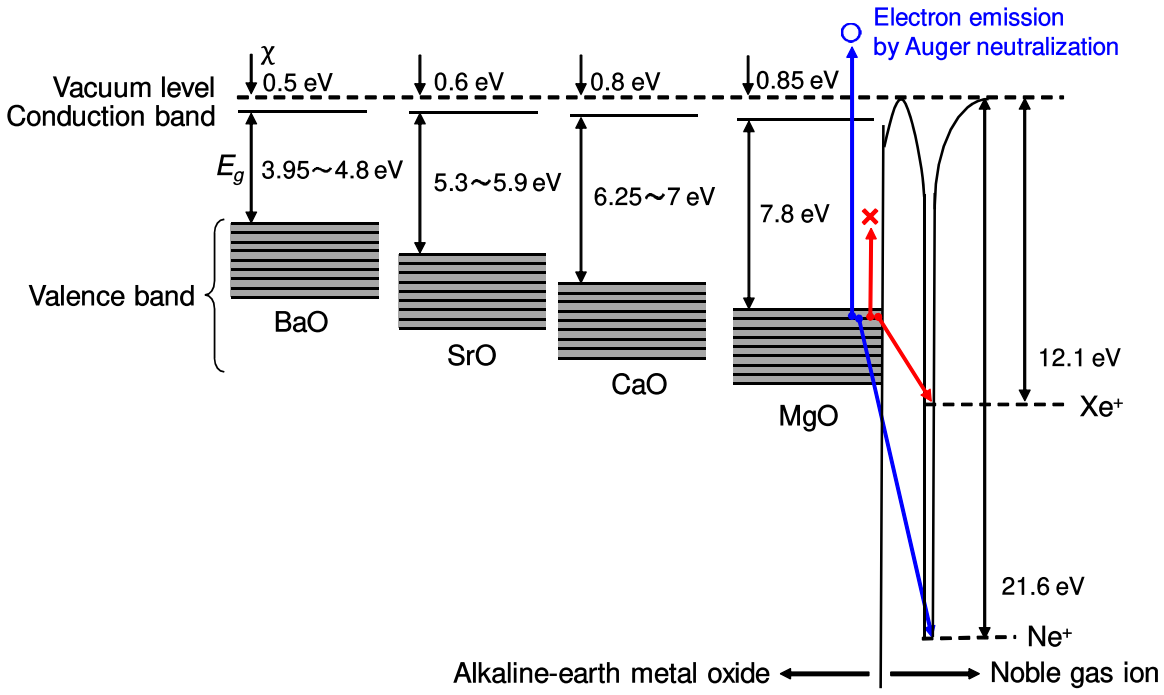

Figure 1.7: Schematic energy diagram for electron emission processes from bulk MgO by the Auger neutralization via Ne^+ and Xe^+. Energy levels of bulk CaO, SrO, and BaO are also shown.

cated at approximately 5.1 eV below the lower edge of the conduction band [69]. The electrons trapped at the F-type centers at the surface also contribute to electron emissions via Xe^+ by the Auger neutralization [70]. However, in spite of these effects, MgO does not have high γ for Xe^+ enough to improve the energy efficiency of plasma discharge devices with a high Xe content. Therefore, higher-γ materials than conventional MgO are necessary to realize a low discharge voltage and a high energy efficiency for a high Xe content in plasma discharge devices.

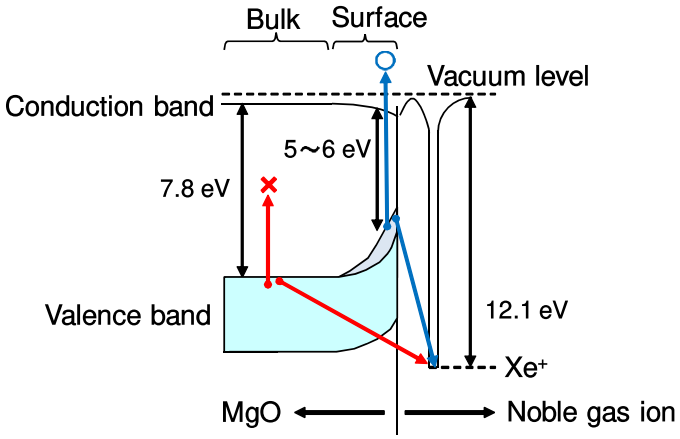

Figure 1.8: Schematic of modified band gap at the surface of MgO.

1.5 High-γ Material for Dielectric Cathode Layer

As higher-γ materials for protective layers in plasma discharge devices, other alkaline-earth metal oxides, i.e., CaO, SrO, and BaO, can be candidates [71,72]. Figure 1.7 shows energy levels of bulk CaO, SrO, and BaO for the comparison with that of MgO. In an electron emission process by the Auger neutralization, a wider band gap indicates lower γ if the electron affinity is equivalent. CaO, SrO, and BaO have narrower band gaps and lower electron affinities in this order [72,73], which leads to high γ for Xe^+ due to the efficient electron emission by the Auger neutralization process [65,66]. However, related to lowering the Madelung potentials at the surfaces, the reactivity of the surface O^{2-} of these materials is strongly enhanced [74,75]. Therefore, these materials are easily react to H_2O and CO_2 in air atmosphere and form hydroxylation and carbonation chemically [76]. This reaction results in widening of the band gaps and degradation of γ for Xe^+ [77], which is a major reason of difficulty to realize the practical

applications for plasma discharge devices with protective layers of single alkaline-earth metal oxide except for MgO.

In order to suppress H_2O- and CO_2-contamination, a structure with double protective layers (a CaO [78] or SrO [79] layer covered with a MgO layer as a barrier material) was proposed. The thickness of several tens to a hundred and several tens of nm is required for the MgO barrier layer. A demerit of this method is a long pre-aging time; over 200 h are needed to erode out the MgO layer and then stabilize the discharge voltage low [78]. Another solution to overcome the problems of the single alkaline-earth metal oxide is introducing a complex based on an alkaline-earth metal oxide. Although the compounds with a low electron affinity or a narrow band gap except for an alkaline-earth metal oxide (RbBr, RbI, CsI, Cs_2O [80], LaF_3 [81], and LaB_6 [82]) have also been studied, their applications are rather limited because of its low producibility, instability, and high cost. Hereafter, the researches and developments on complexes based on alkaline-earth metal oxides are focused on.

1.6 Complex Oxide Cathode Layer with High γ

1.6.1 SrO-based Oxide

A mixed crystal of SrO and CaO ((Sr,Ca)O) is one of the most extensively studied materials for a high-γ protective layer from the 1970s to the 2010s. Shinoda *et al*. first proposed the (Sr,Ca)O protective layers for plasma discharge devices and demonstrated the lowest firing voltages among the conceivable complex oxide protective layers in 1979 [83]. Uchiike *et al*. studied the optimal composition of the (Sr,Ca)O to obtain the best performance of the plasma discharge devices [84]. The (Sr,Ca)O protective layer has been investigated as an alternative of a conventional MgO layer by Kajiyama *et al*. even in the 2010s [85,86]. However, they

still suffer from the high chemical reactivity of SrO, which precludes practical applications in spite of the long-standing researches on (Sr,Ca)O protective layers. In order to realize (Sr,Ca)O protective layers for large-sized devices, Yano *et al*. proposed the procedure called as "all-in-vacuum" [87]. In this procedure, all processes after deposition of a protective layer, such as annealing, panel alignment, panel sealing, and gas filling, are carried out in vacuum to prevent the adsorption of impurity gases on the panel. However, this procedure is hard to be applied in the actual production due to the high cost and the small throughput.

In order to prevent the carbonation and suppress the degradation of electron emission properties of SrO, addition of a covalent element was attempted. The group IV elements, such as Ti, Zr, Hf, and Ce, have no *d* electrons, and exhibit tetravalent covalent nature in common with carbon. Fukui *et al*. demonstrated the improved discharge properties and chemical stability for SrO containing Zr ((Sr,Zr)O) [88]. As shown in Fig. 1.9(a), Yamauchi *et al*. found that the most suitable metal in the above-mentioned group IV elements is Ce for doping into SrO ((Sr,Ce)O) to obtain the reduced discharge voltages; at Ce concentration of approximately 60 at.%, the adsorption of impurity gas is greatly suppressed (see Fig. 1.9(b)) [89]. They also investigated the characteristics of 3- to 42-inch panels with (Sr,Ce)O protective layers. However, because of an inherited chemical reactivity of SrO, the discharge voltages were not well improved in a larger-sized device, which has more adsorbed impurity species on the panel.

1.6.2 CaO-based Oxide

A $12CaO{\cdot}7Al_2O_3$ (C12A7) electride, whose crystal structure is shown in Fig. 1.10(a), can be a candidate material for a protective layer with high γ because it has a low work function ($\sim$ 2.4 eV). As illustrated in Fig. 1.10(b), a free oxygen ion can be replaced by two electrons in a unit cell of C12A7 [90]. The low work function of C12A7 is due to the mid-gap states created by the

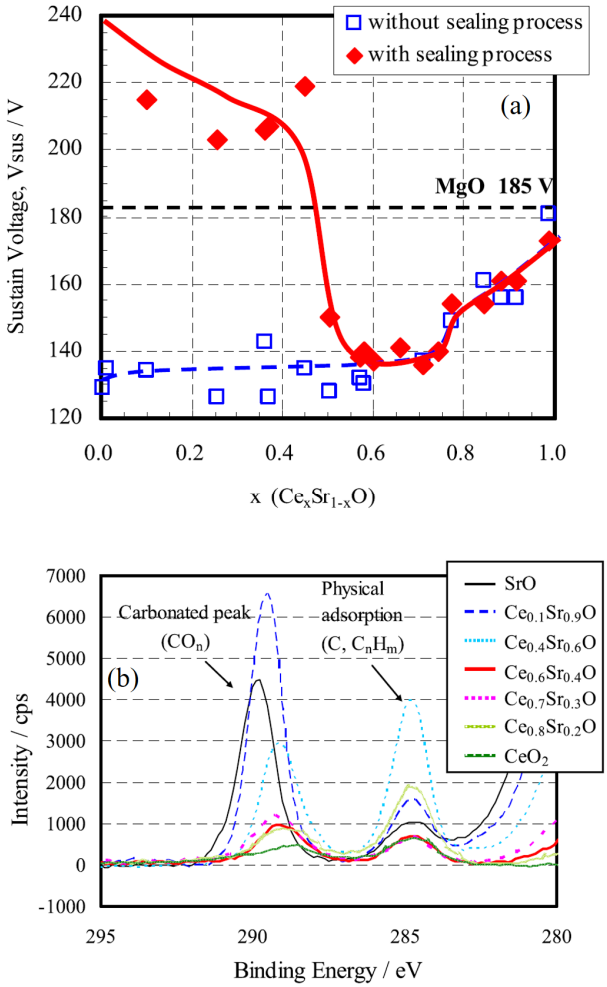

Figure 1.9: (a) Discharge sustaining voltages of PDPs with (Sr,Ce)O protective layers compared with the case of a conventional MgO protective layer [89]. (b) C 1s X-ray photoelectron spectra of (Sr,Ce)O films annealed at 500°C in air compared with the cases of SrO and CeO_2 films [89].

occupied electrons in the cages. Since the C12A7 invention as an excellent electron emitter by Hosono *et al*. [91], a C12A7 electride has been studied for the applications to fluorescent lamps [92,93] and plasma displays [94,95]. In these devices, the potential of reducing a discharge voltage with a C12A7 cathode layer is clearly demonstrated compared with a conventional cathode layer. The reduced discharge voltage arises from the efficient electron emission from the mid-gap level by the Auger neutralization via Xe^+, as described in Fig. 1.10(c). However, a C12A7 electride does not have the thermal stability high enough to be used as a cathode layer for plasma discharge devices. This means that further researches and developments of alloying elements are still required for improvement of the thermal stability [94].

1.6.3 MgO-based Oxide

Numerous dopants into a MgO thin film have been studied to enhance an electron emission property by forming impurity or defect states in the band gap because MgO-based protective layers have sufficient chemical stability [96]. Doping alkali metals (Li [97], Na [98], and K [99]) and Al [100] creates the defect states arising from vacancies at anion and cation sites in a MgO film, respectively. Other representative elements (H [101], Be [102], Si [103], Zn [104], Ge [105], and Cs [106]), transition metal elements (Sc [107], Ti [108], Cr [109], Fe [110], Ni [111], Y [100], Zr [112], Mo [113], Ru [105], Ta [114], and Ce [113]), and compounds (LaB_6 [115]) have also widely been investigated as the dopants. Although these dopants can enhance an electron emission property and then reduce a discharge voltage compared with a pure MgO, the doped-MgO films do not have high γ for Xe^+ enough to improve the device efficiency due to insufficient density of states of the impurity or defect levels when used as protective layers in plasma discharge devices with a high Xe content.

In order to satisfy both chemical stability and appropriate γ for Xe^+, mixed crystals of MgO

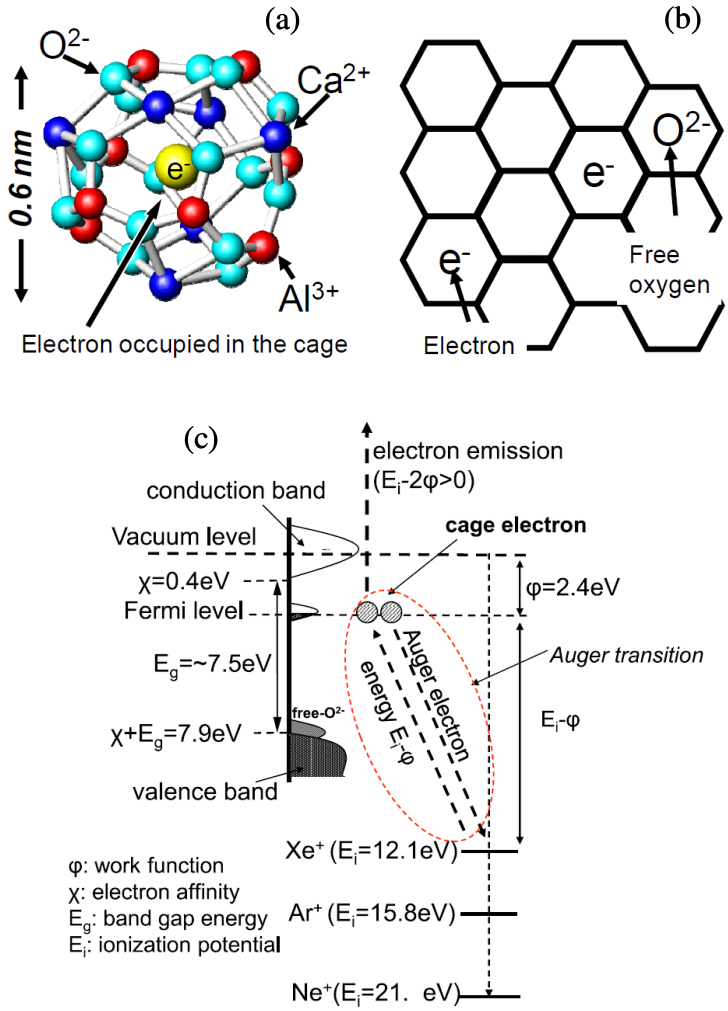

Figure 1.10: (a) Crystal structure of a C12A7 electride with occupied electrons in the cage [92]. (b) Illustration of a C12A7 electride unit cell where an O^{2-} ion is replaced by two electrons [92]. (c) Schematic energy diagram for an electron emission process from a C12A7 electride by the Auger neutralization via noble gas ions [93].

and other alkaline-earth metal oxides, such as (Mg,Ca)O [116-126], (Mg,Sr)O [83,100,126-128], (Mg,Ca,Sr)O [127,129], and (Mg,Ba)O [126,130], have been studied. Modification of the energy band structure by the complexes were demonstrated by the calculation [118] and experiment [128] as shown in Figs. 1.11(a) and 1.11(b), respectively. The modified band structure is expected to result in high-γ properties. Among these complexes, a (Mg,Ca)O material is the most extensively studied from the 1990s to the 2010s, and considered to have the highest potential as a feasible high-γ protective layer. However, a trade-off between maintaining chemical stability by the increase of a MgO concentration and enhancing γ for Xe^+ by the increase of a CaO, SrO, or BaO concentration is obvious. Therefore, the optimal composition should be adjusted according to the conditions of production, discharge gas, and operation for each plasma discharge device.

1.7 (Mg,Ca)O Protective Layer

As described in Section 1.6, a (Mg,Ca)O mixed crystal is the most promising material in the above-mentioned complex oxides for a high-γ protective layer as an alternative of a conventional MgO layer. Cho *et al*. pioneeringly studied the (Mg,Ca)O for plasma discharge devices in 1999 [116,117] and the ardent researches and developments on a (Mg,Ca)O protective layer are still carried out in recent years [124-126]. Using (Mg,Ca)O for protective layers, lower sustaining and firing discharge voltages than conventional MgO have been realized even for large-sized devices such as a 42-inch FHD panel (Zukawa *et al*. in Fig. 1.12(a)) [120] and a 50-inch FHD panel (Lee *et al*. in Fig. 1.12(b)) [123] in production conditions close to those of conventional plasma discharge devices.

One of the remaining problems for a (Mg,Ca)O protective layer is that a discharge voltage is also degraded by hydroxylation or carbonation due to the inherited chemical nature of CaO.

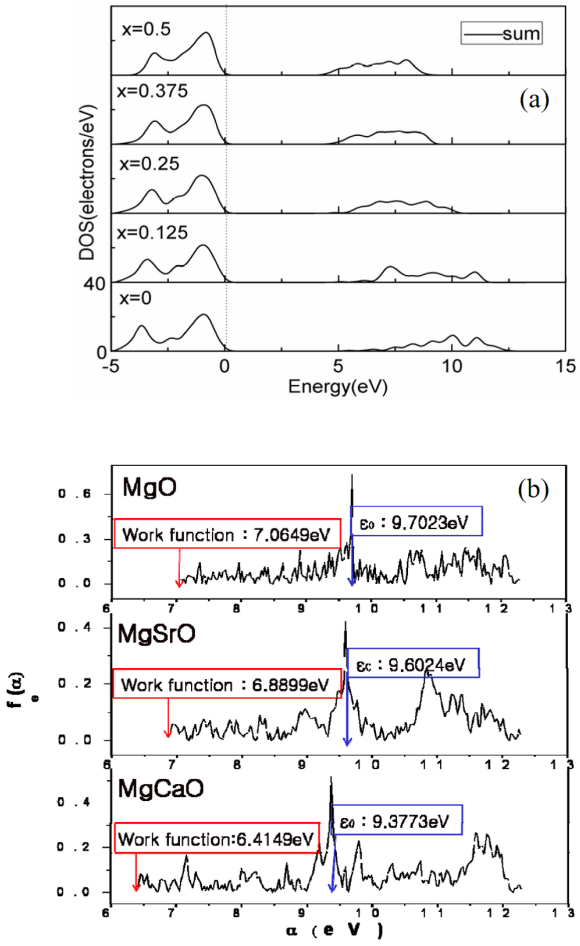

Figure 1.11: (a) Total density of state of (Mg,Ca)O for different values of Ca concentration x derived from the first principle calculation [118]. (b) Electron energy band structures of MgO, (Mg,Sr)O, and (Mg,Ca)O films obtained by the secondary electron emission measurements [128]. ε_0 is the center of the valence band.

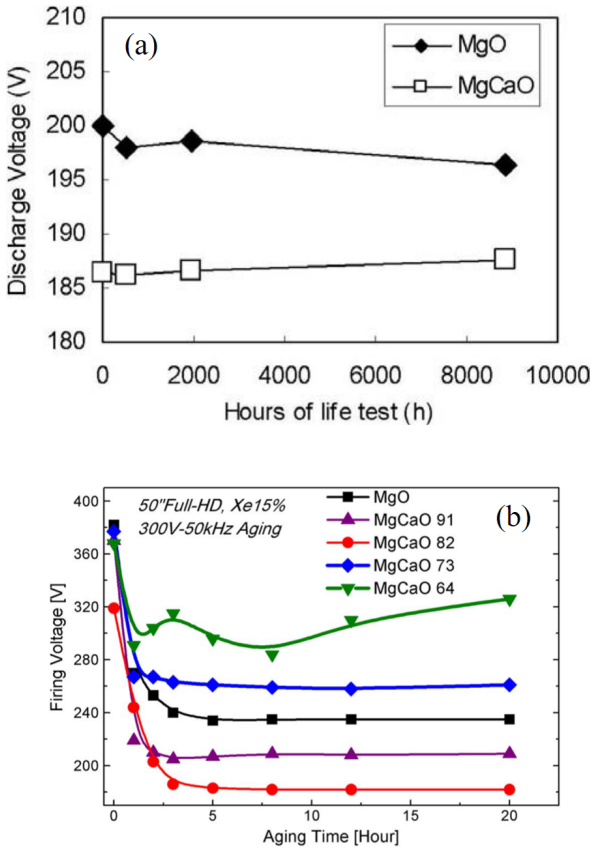

Figure 1.12: (a) Discharge sustaining voltages of a 42-inch FHD panel [120] and (b) discharge firing voltages of 50-inch FHD panels [123] having (Mg,Ca)O protective layers compared with the cases of a MgO protective layer.

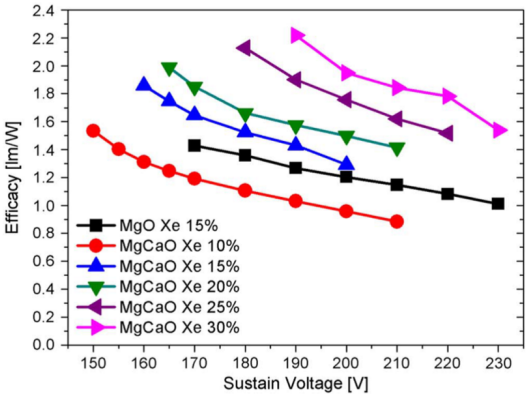

Figure 1.13: Luminous efficiencies of 50-inch FHD panels having (Mg,Ca)O protective layers compared with the case of a MgO protective layer [123].

By these chemical reactions, the discharge voltages can be modified unstably as shown in Fig. 1.12(b). Yan *et al*. reported the hydroxylation and carbonation reactions which probably occur at the surface of a (Mg,Ca)O protective layer [119]. Motoyama *et al*. indicated that the amount of carbon at the surface is related to the discharge voltage for a (Mg,Ca)O protective layer with different CaO concentrations by analyzing the depth profiles of photoelectron signals from carbon [122]. However, the quantitative relationship between a discharge voltage and the chemical state of the (Mg,Ca)O protective layer has yet to be clarified well. Moreover, an applicable process to realize the optimal performance of the (Mg,Ca)O protective layer for the production of plasma discharge devices has never been proposed.

In addition to a discharge voltage, a discharge behavior and a luminous efficiency are also key factors for plasma discharge devices. Lee *et al*. demonstrated that enhancement of the luminous efficiency could be realized even for large-sized devices with (Mg,Ca)O protective layers due to an improved electron emission property compared with a conventional MgO layer, as shown

in Fig. 1.13 [123]. However, these results are limited at the initial state of the operation, and the degradation of a discharge behavior and a luminous efficiency by prolonged aging for (Mg,Ca)O protective layers have yet to be investigated well. Moreover, a suitable process and a device structure to improve the properties of plasma discharge devices with (Mg,Ca)O protective layers have never been proposed.

1.8 Chapter Overview and Goals of This Thesis

The goal of this thesis is to contribute to the realization of a low discharge voltage, a high luminous efficiency, and a long lifespan for plasma discharge devices with (Mg,Ca)O protective layers. In order to accomplish this goal, the mechanisms for the degradation of a discharge voltage, a discharge property, and a luminous efficiency were aimed to be clarified. Moreover, an appropriate process and a device structure to suppress the degradation were discussed. Hereafter, the overviews of the following chapters are described.

In Chapter 2, the author investigates the chemical states related to a discharge voltage when (Mg,Ca)O films are used as protective layers for plasma discharge devices. Analysis of the surface of the (Mg,Ca)O protective layer enables the quantitative assignment of the chemical states of the (Mg,Ca)O protective layer, which is related to a discharge voltage. The effects of the exposure environment after deposition on the progression of chemical reactions which affect the discharge voltage are also studied. An annealing process applicable to recovery of the (Mg,Ca)O protective layer and to reduce the discharge voltage is also investigated.

In Chapter 3, the modification of discharge behaviors by prolonged aging for flat panel plasma discharge devices with (Mg,Ca)O protective layers is investigated. The author demonstrates the shrinkage and expansion of the discharge area for the devices with the (Mg,Ca)O protective layers after prolonged aging. Analyzing the surface of the sputtered protective layers enables

the modification mechanisms of the discharge behaviors to be identified. Moreover, the effective pixel structures to suppress the degradation of the device efficiency due to the modification of discharge behaviors are proposed.

In Chapter 4, the degradation mechanism of a phosphor excitation efficiency in plasma discharge devices with (Mg,Ca)O protective layers by prolonged aging is investigated based on photoluminescence experiments. The author finds that loss of luminance occurs as a result of the absorbance of VUV radiation by organic residues. The consequent formation of byproducts reduces a phosphor excitation efficiency by absorbing the shorter wavelength VUV light. The results indicate that annealing to remove organic species adsorbed on the protective layer and degassing the panels are significantly important to suppress the degradation of a luminous efficiency as well as a discharge voltage in plasma discharge devices with (Mg,Ca)O protective layers.

In Chapter 5, another degradation mechanism of a phosphor excitation efficiency in plasma discharge devices with (Mg,Ca)O protective layers is presented. The results demonstrate that the extent of re-deposition of the sputtered protective layer on the phosphors increases as the device ages, thus reducing the luminance via the absorption of the shorter wavelength VUV radiation. To suppress this degradation, it is quantitatively indicated that engineering the discharge gas conditions, such as the composition and the pressure, and improving the sputtering resistance of a (Mg,Ca)O film are highly required for the decrease of the sputtering rate of the protective layer.

In Chapter 6, the overall results are summarized and a brief outlook for further improvement and reliability of the performance of plasma discharge devices with (Mg,Ca)O protective layers is presented.

References

[1] C. Meyer, H. Nienhuis, Discharge Lamps, Kluwer Technische Boeken BV., Deventer, 1988, pp. 69-140.

[2] T. W. Clarkson, Mercury: Major Issues in Environmental Health, Environ. Health Perspect. 100 (1992) 31-38.

[3] http://www.mercuryconvention.org/

[4] M. Schratz, C. Gupta, T. J. Struhs, K. Gray, Reducing energy and maintenance costs while improving light quality and reliability with LED lighting technology, Conf. Rec. 2013 Annu. IEEE Pulp Paper Ind. Tech. Conf. (2013) 43-49.

[5] U. Kogelschatz, Dielectric-barrier Discharges: Their History, Discharge Physics, and Industrial Applications, Plasma Chem. Plasma Process. 23 (2003) 1-46.

[6] T. Shiga, Mercury-free Fluorescent Lamp Backlights, in: S. Kobayashi, S. Mikoshiba, S. Lim (Eds.), LCD Backlights, John Wiley & Sons, Hoboken, 2009, pp. 171-180.

[7] B. Gellert, U. Kogelschatz, Generation of Excimer Emission in Dielectric Barrier Discharges, Appl. Phys. B 52 (1991) 14-21.

[8] Y. Ikeda, J. P. Verboncoeur, P. J. Christenson, C. K. Birdsall, Global modeling of a dielectric barrier discharge in Ne-Xe mixtures for an alternating current plasma display panel, J. Appl. Phys. 86 (1999) 2431-2441.

[9] K. Tachibana, S. Feng, T. Sakai, Spatiotemporal behaviors of excited Xe atoms in unit discharge cell of ac-type plasma display panel studied by laser spectroscopic microscopy, J. Appl. Phys. 88 (2000) 4967-4974.

[10] Y. P. Raizer, Gas Discharge Physics, Springer Science+Business Media, Berlin Heidelberg, 1997, pp. 52-75.

[11] H. Uchiike, T. Hirakawa, Color Plasma Displays, Proc. IEEE 90 (2002) 533-539.

[12] J. P. Boeuf, Plasma display panels: physics, recent developments and key issues, J. Phys. D: Appl. Phys. 36 (2003) R53-R79.

[13] L. F. Weber, History of the Plasma Display Panel, IEEE Trans. Plasma Sci. 34 (2006) 268-278.

[14] H. G. Slottow, Plasma Displays, IEEE Trans. Electron Devices 23 (1976) 760-772.

[15] M. Shibata, N. Itokawa, H. Koizumi, J. Oota, T. Matsui, N. Iwase, Y. Kobayashi, T. Torinari, H. Ikeda, I. Furukawa, High-Luminance 42-in. Full High-Definition PDP, SID Int. Symp. Dig. Tech. Pap. 37 (2006) 159-162.

[16] H. Tachibana, K. Ogawa, T. Nakajima, T. Nakagawa, M. Fujitani, K. Sumida, World's First 42-in. 1080p HD PDP, Proc. 14th Int. Disp. Workshops 3 (2007) 2117-2120.

[17] R. Murai, K. Ueda, S. Masuda, K. Ogawa. M. Suzuki, S. Ikeda, World largest 103-in. 1080p PDP, Proc. 13th Int. Disp. Workshops 3 (2006) 1797-1798.

[18] H. Ashida, T. Murakoso, Y. Wada, M. Okawa, T. Yamamoto, T. Ando, N. Kimura, S. Ikeda, Development of World's Largest (150-in. Diagonal) Advanced High Definition PDP, SID Int. Symp. Dig. Tech. Pap. 39 (2008) 476-479.

[19] K. Ishii, T. Usui, Y. Murakami, Y. Motoyama, M. Seki, Y. Noguchi, T. Furutani, T. Nakakita, T. Yamashita, Developments of a 145-inch Diagonal Super Hi-Vision Plasma Display Panel, SID Int. Symp. Dig. Tech. Pap. 43 (2012) 71-74.

[20] T. Kosako, B. Guo, H. Tanaka, H. Hirakawa, K. Awamoto, T. Shinoda, Progress in Luminous Array Film （LAFi) with Plasma Tube Technology for Seamless Tilling Super-large-area Display, SID Int. Symp. Dig. Tech. Pap. 44 (2013) 49-52.

[21] I. Kawahara, Advances in Moving Picture Quality of Recent PDPs, Proc. 17th Int. Disp. Workshops 2 (2010) 943-946.

[22] F. K. Opara, M. I. Aririguzo, E. C. Agbaraji, Comparative analysis and performance features of plasma, LCD and CRT screens: operating features, merit and recommendations, Acad. Res. Int. 2 (2012) 140-150.

[23] C. Jang, K. Kim, K. C. Choi, Toward Flexible Transparent Plasma Display: Optical Characteristics of Low-Temperature Fabricated Organic-Based Display Structure, IEEE Electron Device Lett. 33 (2012) 74-76.

[24] W.-S. Song, K.-H. Lee, Y. R. Do, H. Yang, Utilization of All Hydrothermally Synthesized Red, Green, Blue Nanophosphors for Fabrication of Highly Transparent Monochromatic and Full-Color Plasma Display Devices, Adv. Funct. Mater. 22 (2012) 1885-1893.

[25] S. M. Lee, D. Kim, D. Y. Jeon, K. C. Choi, Nanoplasmon-Enhanced Transparent Plasma Display Devices, Small 8 (2012) 1350-1354.

[26] Y. Silver, R. Ball, J. R. Beene, Y. Benhammou, M. Ben-Moshe, J. W. Chapman, T. Dai, E. Etzion, C. Ferretti, N. Guttman, P. S. Friedman, D. S. Levin, S. Ritt, R. L. Varner, C. Weaverdyck, B. Zhou, Development of a plasma panel radiation detector: recent progress and key issues, 2011 IEEE Nucl. Sci. Symp. Conf. Rec. (2011) 1881-1885.

[27] P. S. Friedman, A New Class of Low Cost, High Performance Radiation Detectors, 2005 IEEE Nucl. Sci. Symp. Conf. Rec. (2005) 2815-2822.

[28] M.-S. Yun, S.-H. Cho, K.-M. Oh, M.-W. Kim, S.-H. Jung, G.-W. Jang, S.-U. Heo, C. Kwon, S.-H. Nam, Measurement of the properties of a flat-panel gas X-ray detector, Nucl. Instrum. Methods Phys. Res. A 607 (2009) 162-165.

[29] H. Lee, K. Lee, S. Eom, H. Park, J. Kang, Simulation Study of Plasma Display Panel-Based Flat Panel X-Ray Detector, IEEE Trans. Nucl. Sci. 60 (2013) 908-912.

[30] P. S. Friedman, R. Ball, J. R. Beene, Y. Benhammou, E. H. Bentefour, J. W. Chapman, E. Etzion, C. Ferretti, N. Guttman, D. S. Levin, M. B. Moshe, Y. Silver, R. L. Varner, C. Weaverdyck, B. Zhou, Plasma Panel Sensors for Particle and Beam Detection, 2012 IEEE Nucl. Sci. Symp. Med. Imaging Conf. Rec. (2012) 1775-1780.

[31] P. Friedman, R. Ball, J. Beene, Y. Benhammou, M. Ben-Moshe, H. Bentefour, J. W. Chapman, E. Etzion, C. Ferretti, D. Levin, Y. Silver, R. Varner, C. Weaverdyck, B. Zhou, Plasma panel-based radiation detectors, J. Soc. Inf. Disp. 21 (2013) 46-54.

[32] R. Ball, J. R. Beene, M.Ben-Moshe, Y. Benhammou, B. Bensimon, J. W. Chapman, E. Etzion, C. Ferretti, P. S. Friedman, D. S. Levin, Y. Silver, R. L. Varner, C. Weaverdyck, R. Wetzel, B. Zhou, T. Anderson, K. McKinny, E. H. Bentefour, Development of a plasma panel radiation detector, Nucl. Instrum. Methods Phys. Res. A 764 (2014) 122-132.

[33] R. Murai, M. Murata, Y. Shintani, Application of AC plasma display panels to radiation detectors, J. Soc. Inf. Disp. 24 (2016) 90-98.

[34] T. Urakabe, S. Harada, T. Saikatsu, M. Karino, A Flat Fluorescent Lamp with Xe Dielectric Barrier Discharges, J. Light Vis. Environ. 20 (1996) 20-25.

[35] O. Kwon, B. J. Oh, K.-W. Whang, Discharge characteristics of mercury-free flat fluorescent lamps with various electrode configurations analysed through a two-dimensional

fluid model simulation, J. Phys. D: Appl. Phys. 45 (2012) 275202-1-12.

[36] K. Wang, J. Li, S.-Q. Wang, Optimization of Xenon Gas Discharge Flat Panel Lamps, Adv. Mat. Res. 571 (2012) 256-260.

[37] B. Caillier, T. Beaudette, L. Therese, P. Belenguer, P. Guillot, Studies and optimizations of a commercial mercury-free Dielectric Barrier Discharge (DBD) flat lamp, Eur. J. Electr. Eng. 16 (2013) 565-582.

[38] B. J. Oh, O. Kwon, J.-C. Jung, I. W. Seo, K.-W. Whang, The Effects of Electrode Configuration on the Luminance and Luminous Efficacy of Mercury-Free Flat Fluorescent Lamp, IEEE Trans. Plasma Sci. 39 (2011) 1963-1968.

[39] M. Fiegler, K. Ziemssen, B. Homberg, A High Resolution 5 Megapixel LCD Monitor for Medical Applications with Mercury-Free Flat Panel Lamp Backlighting (PLANON®), SID Int. Symp. Dig. Tech. Pap. 34 (2003) 172-175.

[40] http://www.youyang.co.kr/

[41] J. M. Cho, K. H. Lee, C. I. Cheon, W. S. Choi, J. S. Kim, N. I. Cho, Electron-beam deposition of MgO on plastic substrate and manufacturing flexible flat fluorescent lamp, J. Soc. Inf. Disp. 17 (2009) 765-770.

[42] U. Kogelschatz, Ultraviolet excimer radiation from nonequilibrium gas discharges and its application in photophysics, photochemistry and photobiology, J. Opt. Technol. 79 (2012) 484-493.

[43] T. Zukawa, Y. Sasaki, T. Kurosawa, N. Kamiko, Photolysis of Indigo Carmine solution by planar vacuum-ultraviolet (147 nm) light source, Chemosphere 214 (2019) 123-129.

[44] M. Pirnie, K. G. Linden, J. P. Malley, Ultraviolet Disinfection Guidance Manual for the Final Long Term 2 Enhanced Surface Water Treatment Rule, U.S. EPA, Washington, D.C., 2006, pp. 2-1-38.

[45] T. Zukawa, Y. Sasaki, H. Tsujimoto, N. Kamiko, E. Nakamura, Development of a mercury-free plate-type ultraviolet light source, 2016 Int. Ultraviolet Assosi. World Congr. Proc. (2016).

[46] K. Awamoto, H. Hirakawa, J. Takahashi, T. Hidaka, T. Shinoda, Development of the Flexible Surface Light Source Using Luminous Array Film Technology, Proc. 23rd Int. Disp. Workshops 1 (2016) 504-507.

[47] S. Al-Gharabli, P. Engeβer, D. Gera, S. Klein, T. Oppenländer, Engineering of a highly efficient $Xe_2{}^*$-excilamp (xenon excimer lamp, λ_{max} = 172 nm, η = 40 %) and qualitative comparison to a low-pressure mercury lamp (LP-Hg, λ = 185/254 nm) for water purification, Chemosphere 144 (2016) 811-815.

[48] R. Prakash, A. M. Hossain, U. N. Pal, N. Kumar, K. Khairnar, M. K. Mohan, Dielectric Barrier Discharge based Mercury-free plasma UV-lamp for efficient water disinfection, Sci. Rep. 7 (2017) 17426-1-8.

[49] N. Koca, M. Urgu, T. E. Saatli, Ultraviolet Light Applications in Dairy Processing, in: N. Koca (Ed.), Technological Approaches for Novel Applications in Dairy Processing, IntechOpen, London, 2018, pp. 3-22.

[50] R. Dippenaar, J. Smith, Impact of pulsed xenon ultraviolet disinfection on surface contamination in a hospital facility's expressed human milk feed preparation area, BMC Infect. Dis. 18 (2018) 91-1-6.

[51] M. Berneburg, M. Röcken, F. Benedix, Phototherapy with Narrowband vs Broadband UVB, Acta Derm Venereol 85 (2005) 98-108.

[52] A. Morita, Current developments in phototherapy for psoriasis, J. Dermatol. 45 (2018) 287-292.

[53] A. Morita, Y. Shintani, E. Nishida, H. Kato, H. Yoshida, M. Minamoto, Y. Yamaguchi, A. Maeda, Feasibility and accuracy of a newly developed hand-held device with a flat-type fluorescent lamp for measuring the minimal erythema dose for narrow-band UVB therapy, Photodermatol. Photoimmunol. Photomed. 25 (2009) 41-44.

[54] B. Guo, K. Awamoto, H. Hirakawa, T. Nishimoto, A flexible Luminous Array Film (LAFi) as a radiation area selectable Hg-free ultra-narrow band UVB light source, Proc. 21st Int. Disp. Workshops 1 (2014) 615-617.

[55] K. Awamoto, H. Hirakawa, B. Guo, T. Shinoda, Current Status of the Flexible Surface Light Source Development using LAFi Technology, Proc. 22th Int. Disp. Workshops 2 (2015) 960-961.

[56] E. A. Sosnin, Y. V. Chudinova, I. A. Victorova, I. I. Volotko, Application of excilamps in agriculture and animal breeding (Review), Proc. SPIE 9810 (2015) 98101K-1-7.

[57] T. Oppenländer, Excilamp Photochemistry, in: A. G. Griesbeck, M. Oelgemöller, F. Ghetti (Eds.), CRC Handbook of Organic Photochemistry and Photobiology, Third ed. Vol. 1, CRC Press, Boca Raton, 2012, pp. 21-48.

[58] I. Adamovich, S. D. Baalrud, A. Bogaerts, P. J. Bruggeman, M. Cappelli, V. Colombo, U. Czarnetzki, U. Ebert, J. G. Eden, P. Favia, D. B. Graves, S. Hamaguchi, G. Hieftje, M. Hori, I. D. Kaganovich, U. Kortshagen, M. J. Kushner, N. J. Mason, S. Mazouffre, S.

M. Thagard, H.-R. Metelmann, A. Mizuno, E. Moreau, A. B. Murphy, B. A. Niemira, G. S. Oehrlein, Z. Lj Petrovic, L. C. Pitchford, Y.-K. Pu, S. Rauf, O. Sakai, S. Samukawa, S. Starikovskaia, J. Tennyson, K. Terashima, M. M. Turner, M. C. M. van de Sanden, A. Vardelle, The 2017 Plasma Roadmap: Low temperature plasma science and technology, J. Phys. D: Appl. Phys. 50 (2017) 323001-1-46.

[59] R. Ganter, Th. Callegari, L. C. Pitchford, J. P. Boeuf, Efficiency of AC plasma display panels from diagnostics and models, Appl. Surf. Sci. 192 (2002) 299-308.

[60] J. Meunier, Ph. Belenguer, J. P. Boeuf, Numerical model of an ac plasma display panel cell in neon-xenon mixtures, J. Appl. Phys. 78 (1995) 731-745.

[61] G. Oversluizen, T. Dekker, M. F. Gillies, S. T. de Zwart, High-Xe-content high-efficacy PDPs, J. Soc. Inf. Disp. 12 (2004) 51-55.

[62] Z. Liu, W.-B. Hu, C.-L. Liu, Luminance and Luminous Efficacy Improvement of Mercury-Free Flat Fluorescent Lamp With Arclike Electrode, IEEE Trans. Plasma Sci. 38 (2010) 2860-2866.

[63] H. Uchiike, K. Miura, N. Nakayama, T. Shinoda, Y. Fukushima, Secondary Electron Emission Characteristics of Dielectric Materials in AC-Operated Plasma Display Panel, IEEE Trans. Electron Devices 23 (1976) 1211-1217.

[64] E.-H. Choi, J.-Y. Lim, Y.-G. Kim, J.-J. Ko, D.-I. Kim, C.-W. Lee, G.-S. Cho, Secondary electron emission coefficient of a MgO single crystal, J. Appl. Phys. 86 (1999) 6525-6527.

[65] H. D. Hagstrum, Theory of Auger Neutralization of Ions at the Surface of a Diamond-Type Semiconductor, Phys. Rev. 122 (1961) 83-113.

[66] M. O. Aboelfotoh, J. A. Lorenzen, Influence of secondary-electron emission from MgO surfaces on voltage-breakdown curves in Penning mixtures for insulated-electrode discharges, J. Appl. Phys. 48 (1977) 4754-4759.

[67] H. Kajiyama, K. Suesada, S. Miyamoto, K. Tsutsumi, M. Kitagaki, Surface Electronic States of MgO Induced by Auger Neutralization Process, SID Int. Symp. Dig. Tech. Pap. 42 (2011) 501-504.

[68] Q. Li, Y. Tu, L. Yang, K. Dai, J. Wang, H. Tolner, First-principles Study of Secondary Electron Emission of Modified MgO Surfaces in Plasma Displays, SID Int. Symp. Dig. Tech. Pap. 44 (2013) 134-136.

[69] G. H. Rosenblatt, M. W. Rowe, G. P. Williams, Jr., R. T. Williams, Y. Chen, Luminescence of F and F^+ centers in magnesium oxide, Phys. Rev. B 39 (1989) 10309-10318.

[70] Y. Motoyama, Y. Hirano, K. Ishii, Y. Murakami, F. Sato, Influence of defect states on the secondary electron emission yield γ from MgO surface, J. Appl. Phys. 95 (2004) 8419-8424.

[71] P. S. Wagener, The Oxide-Coated Cathode Vol. 2, Chamoman & Hall Ltd., London, 1951, pp. 214-235.

[72] J. W. Lee, Kinetic Energy Distribution of Auger Electrons of MgO, CaO, SrO and BaO Induced by Auger Neutralization of He^+, Ne^+, Ar^+ and Xe^+ Ions, New Phys.: Sae Mulli 67 (2017) 1168-1173.

[73] B. Baumeier, P. Krüger, J. Pollmann, Bulk and surface electronic structures of alkaline-earth metal oxides: Bound surface and image-potential states from first principles, Phys. Rev. B 76 (2007) 205404-1-9.

[74] G. Pacchioni, C. Sousa, F. Illas, F. Parmigiani, P. S. Bagus, Measures of ionicity of alkaline-earth oxides from the analysis of *ab initio* cluster wave functions, Phys. Rev. B 48 (1993) 11573-11582.

[75] G. Pacchioni, J. M. Ricart, F. Illas, Ab Initio Cluster Model Calculations on the Chemisorption of CO_2 and SO_2 Probe Molecules on MgO and CaO (100) Surfaces. A Theoretical Measure of Oxide Basicity, J. Am. Chem. Soc. 116 (1994) 10152-10158.

[76] M. B. Jensen, L. G. M. Pettersson, O. Swang, U. Olsbye, CO_2 Sorption on MgO and CaO Surfaces: A Comparative Quantum Chemical Cluster Study, J. Phys. Chem. B 109 (2005) 16774-16781.

[77] M. Sakai, S. Hatta, Y. Fukui, Y. Honda, M. Okafuji, Y. Yamauchi, M. Nishitani, Y. Tanaka, Analysis of the Deterioration of Secondary Electron Emission Coefficient of Protective Layers Formed by Alkaline-Earth Oxides for Plasma Display Panels, Proc. 15th Int. Disp. Workshops 3 (2008) 1881-1884.

[78] M. Hasegawa, S. Fukuta, K. Betsui, Air Stable High-γ Discharge Protective Layer Covered with Barrier Material, Proc. 16th Int. Disp. Workshops 3 (2009) 1941-1944.

[79] H.-Y. Jung, T.-H. Lee, O. Kwon, H.-W. Cheong, S. O. Steinmüller, J. Janek, K.-W. Whang, Realization of High Luminous Efficacy at Low Voltages in the Plasma Display Panel With SrO-MgO Double Layer, IEEE Electron Device Lett. 31 (2010) 686-688.

[80] T. J. Vink, A. R. Balkenende, R. G. F. A. Verbeek, H. A. M. van Hal, S. T. de Zwart, Materials with a high secondary-electron yield for use in plasma displays, Appl. Phys. Lett. 80 (2002) 2216-2218.

[81] W. T. Lee, S. J. Im, J. G. Han, S. Yu. D. Y. Lee, J. W. Lee, J. M. Kim, E. H. Choi, LaF_3/MgO Protective Layer in AC-Plasma Display Panels, Jpn. J. Appl. Phys. 42 (2003) 4501-4503.

[82] J. Deng, B. Q. Zeng, X. J. Wang, Z. L. Lin, K. C. Qi, G. C. Cao, Improvement of Discharge Properties by Printing LaB_6 Films on MgO Protective Layers in Plasma Display Panel, IEEE Electron Device Lett. 34 (2013) 1026-1028.

[83] T. Shinoda, H. Uchiike, S. Andoh, Low-Voltage Operated AC Plasma-Display Panels, IEEE Trans. Electron Devices 26 (1979) 1163-1167.

[84] H. Uchiike, K. Sekiya, T. Hashimoto, T. Shinoda, Y. Fukushima, Optimum Composition of CaO, SrO Dielectric Materials in AC Plasma Display Panels, IEEE Trans. Electron Devices 30 (1983) 1735-1742.

[85] G. Uchida, S. Uchida, T. Akiyama, H. Kajiyama, T. Shinoda, Effect of high Xe-concentration in a plasma display panel with a SrCaO cold cathode, J. Appl. Phys. 107 (2010) 103311-1-7.

[86] D. Zhu, L. Song, X. Zhang, H. Kajiyama, Vacuum ultra-violet emission of plasma discharges with high Xe partial pressure using a cathode protective layer with high secondary electron emission, J. Appl. Phys. 115 (2014) 063302-1-7.

[87] T. Yano K. Uchida, G. Uchida, T. Shinoda, H. Kajiyama, Discharge Characteristics of PDPs with the Ternary Oxides Protective Layers Manufactured by Using All-In-Vacuum Process, SID Int. Symp. Dig. Tech. Pap. 41 (2010) 739-741.

[88] Y. Fukui, Y. Honda, Y. Yamauchi, M. Okafuji, M. Sakai, M. Nishitani, Y. Takata, Discharge properties and chemical stability of SrZrO films, J. Soc. Inf. Disp. 18 (2010)

1090-1094.

[89] Y. Yamauchi, Y. Fukui, Y. Honda, M. Okafuji, M. Sakai, M. Nishitani, Y. Yamauchi, Effect of Impurity in Discharge Gas on High γ Properties of Newly Developed CeSrO Film for Novel Plasma Display Panel, IEICE Trans. Electron. E95-C (2012) 1761-1768.

[90] M. Ono-Kuwahara, S. Webster, S. Ito, H. Honoso, Highly Efficient Field Emission from Spin-Coated Electride Powder, SID Int. Symp. Dig. Tech. Pap. 37 (2006) 1642-1645.

[91] S. Matsuishi, Y. Toda, M. Miyakawa, K. Hayashi, T. Kamiya, M. Hirano, I. Tanaka, H. Hosono, High-Density Electron Anions in a Nanoporous Single Crystal: $[Ca_{24}Al_{28}O_{64}]^{4+}$ $(4e^{-})$, Science 301 (2003) 626-629.

[92] N. Miyakawa, T. Watanabe, S. Watanabe, K. Ito, S. Ito, H. Hosono, S. Mikoshiba, A Use of Electrically Conductive Oxide Ceramic ($12CaO{\cdot}7Al_2O_3$ Electride) Electrode having Low Work Function and Low Sputtering Yield for Fluorescent Lamps, SID Int. Symp. Dig. Tech. Pap. 42 (2011) 762-765.

[93] S. Watanabe, T. Watanabe, K. Ito, N. Miyakawa, S. Ito, H. Hosono, S. Mikoshiba, Secondary electron emission and glow discharge properties of $12CaO{\cdot}7Al_2O_3$ electride for fluorescent lamp applications, Sci. Technol. Adv. Mater. 12 (2011) 034410-1-8.

[94] M.-Y. Lee, Y.-S.Kim, Electron Emission from 12CaO $7Al_2O_3$ Electride in Glow Discharge of PDP, Proc. 13th Int. Disp. Workshops 2 (2006) 1169-1172.

[95] S. Webster, M. Ono, S. Ito, H. Kajiyama, T. Shinoda, H. Hosono, Electron emission characteristics of hydrogen doped $12CaO{\cdot}7Al_2O_3$ electride for PDP, Proc. 14th Int. Disp. Workshops 2 (2007) 795-798.

[96] H. Tolner, Fundamental Aspects of Exoemission in Plasma Display Panels, SID Int. Symp. Dig. Tech. Pap. 38 (2007) 1425-1429.

[97] S. I. Ahn, H. Uchiike, S. E. Lee, K. Kim, S. J. Kwon, The Effect of Li-Ion-Doped Porous MgO Film on Operational Memory Margin of ac-Plasma Display Panel, Jpn. J. Appl. Phys. 46 (2007) 6022-6026.

[98] S. I. Ahn, S. E. Lee, S. H. Ryu, K. C. Choi, S. J. Kwon, H. Uchiike, A study on the secondary electron emission from Na-ion-doped MgO films in relation to the discharge characteristics of plasma display panels, Thin Solid Films 517 (2009) 1706-1709.

[99] S. I. Ahn, S. H. Ryu, S. E. Lee, S. H. Moon, K. C. Choi, The Effect of Potassium-Doped MgO Films on Discharge Characteristics in AC-Plasma Display Panel, Jpn. J. Appl. Phys. 46 (2007) 3579-3582.

[100] R. Kim, Y. Kim, J.-W. Park, Influence of densification of the protective layer on the discharge voltage in AC plasma display panel, Vacuum 61 (2001) 37-43.

[101] G. S. Lee, J. Y. Lee, Y. B. Cheon, K. B. Kim, J. J. Kim, S. H. Sohn, Influence of hydrogen-doped MgO thin films on the discharge characteristics in plasma display panels, Thin Solid Films 519 (2011) 3037-3042.

[102] E. Y. Jung, C.-S. Park, S. H. Sohn, The Influence of the Defect States on the Secondary Electron Emission from the $Mg_{1-x}Be_xO$ Protective Layer of AC Plasma Display Panels, Mol. Cryst. Liq. Cryst. 564 (2012) 43-49.

[103] C. H. Ha, J. K.Kim, K.-W. Whang, The Operation Characteristics of an Alternating Current Plasma Display Panel With Si-Doped MgO Protecting Layer, IEEE Trans. Electron Devices 55 (2008) 992-996.

[104] Q. Li, Y. Tu, H. Tolner, L. Yang, Plasma discharge efficiency increase by using a small bandgap protective layer material- first-principles study for $Mg_{1-x}Zn_xO$, J. Appl. Phys. 109 (2011) 093307-108.

[105] J. W. Lee, Defect States of Zr-, Ru-, Si- and Ge-doped MgO Calculated by Using First-Principles Method for Auger Neutralization, New Phys.: Sae Mulli 66 (2016) 1354-1358.

[106] S. J. Rhoa, S. M. Jeonga, H. K. Baika, K. M. Song, The structural, optical and secondary electron emission properties of MgO and Mg-O-Cs thin films prepared by ion beam assisted deposition, Thin Solid Films 355-356 (1999) 55-59.

[107] E. Y. Jung, C.-S. Park, T. E. Hong, S. H. Sohn, Effects of Sc- and Zr-doped MgO layers on electron emission and discharge characteristics of alternating-current plasma display panels, Jpn. J. Appl. Phys. 53 (2014) 036002-1-4.

[108] R. Kim, Y. Kim, J.-W. Park, Electrical properties of evaporated MgO-TiO_2 protective layer for AC PDP, J. Mat. Sci. 36 (2001) 1469-1473.

[109] J. W. Lee, J.-H. Ko, Defect states of transition metal-doped MgO for secondary electron emission of plasma display panel, J. Inf. Disp. 15 (2014) 157-161.

[110] J.-W. Ok, D.-K. Lee, D.-H. Kim, H. J. Lee, H.-J. Lee, C.-H. Park, The effect of Fe-doped magnesium oxide thin film in alternative current plasma display panel, Thin Solid Films 517 (2009) 4152-4155.

[111] A. Nakao, Y. Tanaka, A. Ide-Ektessabi, Discharge properties of a micro plasma cell with an MgO-NiO protecting layer, Surf. Coat. Technol. 203 (2009) 2731-2734.

[112] J. Wang, H. Wua, Z. Song, K. Xu, C. Liu, Microstructure and discharge properties of Mg-Zr-O protective films in plasma display panel, Appl. Surf. Sci. 256 (2009) 603-607.

[113] A. Kumar, S. Thota, D. Deva, J. Kumar, Ion-induced secondary electron emission, optical and hydration resistant behavior of MgO, Mg-Mo-O and Mg-Ce-O thin films, Thin Solid Films 556 (2014) 260-269.

[114] Y. Kim, Y.-U. Lee, J.-W. Park, Effect of the Addition of Ta_2O_5 on the Voltage Characteristics and the Memory Coefficient of the MgO Protective Layer for AC Plasma Display Panel, J. Korean Phys. Soc. 39 (2001) S120-S124.

[115] J. Deng, B. Zeng, Y. Wang, X. Wang, Z. Lin, K. Qi, G. Cao, Fabrication and characteristics of LaB_6-doped MgO protective layer for plasma display panels, Mat. Lett. 134 (2014) 51-55.

[116] J. Cho, R. Kim, K.-W. Lee, G.-Y. Yeom, J.-Y. Kim, J.-W. Park, Effect of CaO addition on the firing voltage of MgO films in AC plasma display panels, Thin Solid Films 350 (1999) 173-177.

[117] J. Cho, R. Kim, K.-W. Lee, C. Son, G.-Y. Yeom, H. J. Kim, J.-Y. Kim, J.-W. Park, Low-voltage characteristics of MgO-CaO films as a protective layer for AC plasma display panels by e-beam evaporation, J. Mat. Sci. 34 (1999) 5055-5059.

[118] Q. F. Li, Y. Tu, L. Yang, H. Tolner, A First Principles Study in $Ca_xMg_{1-x}O$ Protective Layer for Plasma Display Panels, SID Int. Symp. Dig. Tech. Pap. 41 (2010) 1558-1560.

[119] Q. Yan, X. Deng, Z. Lu, F. Xing, X. Zhang, C. Tang, H. Wei, High Luminous Efficacy PDP Using $Ca_xMg_{1-x}O$ Protecting Layer, SID Int. Symp. Dig. Tech. Pap. 42 (2011) 633-636.

[120] T. Zukawa, K. Yoshino, Y. Oe, H. Kawarazaki, K. Aoto, Y. Tanaka, R. Murai, Development of MgCaO Protective Layer of Plasma Display Panels for Decreased Discharge Voltage, SID Int. Symp. Dig. Tech. Pap. 43 (2012) 165-167.

[121] S. Jeong, J.-S. Kim, Y.-S. Kim, Effects of Sealing Conditions and CaO Contents on Aging Behavior of AC-PDP with (Mg,Ca)O Protective Layer, SID Int. Symp. Dig. Tech. Pap. 44 (2013) 131-133.

[122] Y. Motoyama, D. Kato, N. Saito, M. Seki, Carbonation reaction of (Ca, Mg)O protective layer on plasma display panel, J. Soc. Inf. Disp. 21 (2013) 41-45.

[123] T.-H. Lee, H.-W. Cheong, O. Kwon, K.-W. Whang, Application of MgCaO Cathode Layer to Plasma Display Panel for High Luminous Efficacy, IEEE Trans. Electron Devices 60 (2013) 301-304.

[124] Q. Yan, K. Kotera, H. Zhao, H. Liu, H. Zhou, Y. Tang, X. Deng, Calcium Magnesium Oxide Nano-crystal (Nano-CMO) for Improving Uniformity of High Xe Content PDP, SID Int. Symp. Dig. Tech. Pap. 45 (2014) 208-211.

[125] C.-S. Park, E. Y. Jung, H.-S. Tae, Improvement of luminous efficiency using Li-doped MgO layer coated by MgCaO crystal powders in plasma display panels, Mol. Cryst. Liq. Cryst. 645 (2017) 130-137.

[126] J. W. Lee, Calculation of the Secondary Electron Emission Coefficients of MgO, MgBeO, MgCaO, MgSrO and MgBaO Induced by Auger Neutralization of He^+, Ne^+, Ar^+ and Xe^+ Ions, New Phys.: Sae Mulli 68 (2018) 939-944.

[127] S.-K. Kwon, S.-S. Yang, J.-H. Kim, B.-H. Ha, C.-H. Bae, J.-W. Seo, J.-W. Woo, J.-S. Ahn, Y.-L. Cho, Y.-K. Jung, S.-G. Choi, High Luminous Efficacy and Low Power Consumption

Plasma TV, SID Int. Symp. Dig. Tech. Pap. 42 (2011) 741-744.

[128] K. A. Lee, B. K. Min, Y. S. Byeon, J. H. Choi, R. J. Jung, H. S. Uhm, E. H. Choi, Measurement of Energy Band Structure of MgO, MgSrO and MgCaO Thin Film by their Secondary Electron Emission Coefficient due to Auger Neutralization, J. Phys.: Conf. Ser. 417 (2013) 012009-1-11.

[129] R. Kim, Y. Kim, J. Cho, J.-W. Parka, Luminous efficiency and secondary electron emission characteristics of alternating current plasma display panels with MgO-SrO-CaO protective layers, J. Vac. Sci. Technol. A 18 (2000) 2493-2496.

[130] H. K. Yu, W.-K. Kim, J.-L. Lee, J. S. Kim, J. H. Ryu, The Effect of Doping to MgO Protection Layer on Secondary Electron Emission Property, SID Int. Symp. Dig. Tech. Pap. 37 (2006) 544-546.

Chapter 2

Annealing process for recovery of carbonated (Mg,Ca)O protective layer for plasma discharge device

The carbonation behavior and decarbonation annealing of a protective (Mg,Ca)O layer for flat panel plasma discharge devices were investigated in this chapter. Compared with a conventional MgO protective layer, the (Mg,Ca)O protective layer showed both high and low discharge voltages. Quantitative X-ray photoelectron spectroscopy analyses indicated that the high discharge voltages were caused by Ca carbonation. The progression of Ca carbonation was enhanced by exposure to air containing H_2O but not by exposure to dry air. In addition, once (Mg,Ca)O is carbonated, it is impossible to decarbonate Ca by annealing in air at the temperature applied during the production process. Annealing in vacuum is proposed as an effective method to promote the decarbonation of Ca and maintain a low discharge voltage for plasma discharge devices with (Mg,Ca)O protective layers.

2.1 Introduction

Improvement of the degraded discharge voltage of plasma discharge devices with (Mg,Ca)O protective layers is a focal issue of this chapter. As described in Chapter 1, (Mg,Ca)O is the most perspective material as a protective layer in a plasma discharge device [1-6]. Motoyama *et al*. demonstrated the air-stability of a (Mg,Ca)O protective layer for a lower discharge voltage than a conventional MgO layer in a 2-inch panel [7]. However, in the case of larger-size devices, the discharge voltage is greatly increased by hydroxylation and carbonation owing to the large amount of residual impurities in the panel than in smaller-size devices. The low gaseous conductance for degassing during the panel sealing process results in the increase of residual impurities in larger-sized devices [8].

Yan *et al*. reported the issues of a manufacturing process for introducing a (Mg,Ca)O protective layer [9,10]. They pointed out that a special process was required for the production of plasma discharge devices with (Mg,Ca)O protective layers compared with the case of a conventional MgO protective layer. In order to reduce the discharge voltage, the sealing processes under N_2 atmosphere [11] and high sealing temperature [12] were proposed. These sealing processes are certainly effective for suppressing carbonation, but ineffective for decomposition of the carbonated species formed prior to the sealing process due to high decarbonation temperature for $CaCO_3$ [12]. Therefore, a suitable process to obtain the best performance of the (Mg,Ca)O protective layer for the production of plasma discharge devices has yet to be proposed. Moreover, extensive quantitative analyses of the relationship between the discharge voltage and the chemical state of the (Mg,Ca)O protective layer have never been performed.

In present work, the chemical states of a (Mg,Ca)O protective layer related to the discharge voltage are investigated. In order to assess the modification of the discharge voltage, PDPs are used as model Xe DBD devices. The chemical state related to the discharge voltage is

quantitatively assigned by analyzing the surface of the (Mg,Ca)O protective layer. The exposure environment after deposition which affects the progression of the chemical reaction is also investigated. An annealing process applicable to recovering the (Mg,Ca)O protective layer in the panel with a high discharge voltage is also proposed.

2.2 Experimental Methods

To investigate the effects of a (Mg,Ca)O protective layer on the discharge voltage in plasma discharge devices, 42-inch AC PDPs with FHD were produced. MgO and (Mg,Ca)O films were deposited as protective layers on the dielectric layers of the front panels by electron beam evaporation. During the deposition, the substrate temperature was kept at 350°C, and O_2 gas was continuously supplied to the chamber with the flow rate of 20 sccm. The evaporation targets for (Mg,Ca)O were sintered mixtures of MgO and CaO. Two kinds of the target pellets, i.e. rectangular and cylindrical shapes, were prepared as shown in Figs. 2.1(a) and 2.1(b), respectively; the latter was practically employed due to lower splashes of the pellets during electron beam irradiation with high current density. The thickness of the deposited protective layers was 800 nm. Figures 2.2(a) and 2.2(b) show a scanning electron microscope (SEM; S-4600, HITACHI) image ($\times$ 100,000) at the surface of the deposited (Mg,Ca)O film and X-ray diffraction (XRD; X'Pert PRO MPD, Malvern Panalytical) profiles of the (Mg,Ca)O film and the sintered pellet mixed with MgO and CaO, respectively. The resulting films were tricornered at the surface and showed (111) preferred orientation. The XRD peak position of (111) plane of a (Mg,Ca)O film is linearly modified depending on a CaO concentration between the (111) peak positions of MgO and CaO according to the Vegard's law [13,14]. Thus, the CaO concentration of the (Mg,Ca)O protective layer in this study was confirmed as approximately 12 mol% by their (111) peak positions. MgO powders were dispersed on the protective layers to improve

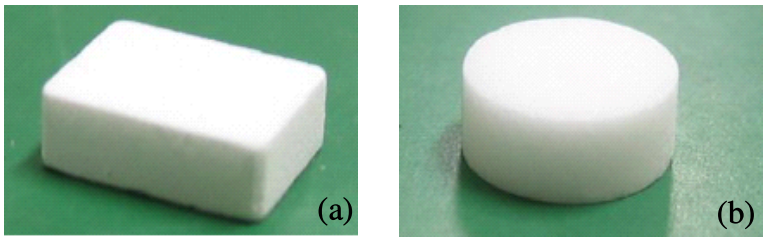

Figure 2.1: The evaporation targets for (Mg,Ca)O deposition; (a) rectangular and (b) cylindrical in shape.

the statistical discharge delay [15]. The panels were sealed with N_2 gas supplied to the space between the front and back panels. The Xe content used in the discharge gas was 100%. The pressure of Xe discharge gas in the panels was set to 225 Torr. The specifications of the test panels used in this study are shown in Table 2.1.

The panels were kept in dry air after the deposition of the MgO and (Mg,Ca)O films to suppress H_2O adsorption on the samples. In addition, the panels were dismantled only in dry air and the samples were cut into the pieces at the size of a few cm^2 to be kept in sealed packages filled with N_2 gas until the measurements. The dew point of the dry air was controlled to approximately $-40°C$. The exposure time to normal air containing H_2O after unsealing the packages prior to introducing the samples into the vacuum chamber of the measurement system was less than 15 s.

The chemical states of C, O, Mg, and Ca in (Mg,Ca)O were characterized by X-ray photoelectron spectroscopy (XPS; PHI Quantera SXM, ULVAC PHI). The samples were excited by a monochromatic X-ray source with an Al Kα line at 1486.7 eV. The spot size of incident X-rays was 50 μm in diameter. The photoelectron signals from the samples were detected at a take-off

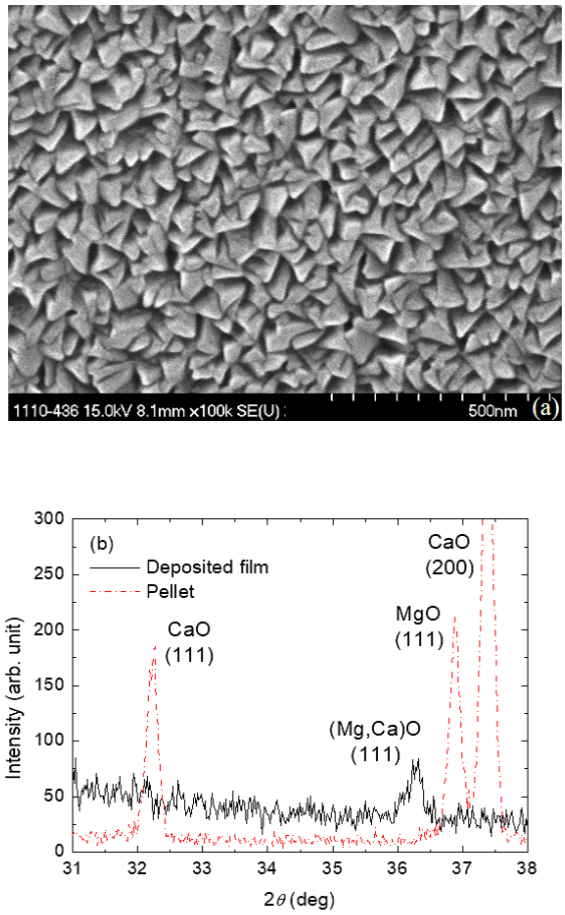

Figure 2.2: (a) SEM image (× 100,000) at the surface of the deposited (Mg,Ca)O film and (b) XRD profiles of the (Mg,Ca)O film and the sintered pellet mixed with MgO and CaO.

Table 2.1: Specifications of the test panels used in this study.

Front Panel	
ITO electrode width	110 μm
Bus electrode width	65 μm
Electrode gap	80 μm
Dielectric layer thickness	39 μm
Protective layer thickness	800 nm
Back Panel	
Address electrode width	65 μm
Dielectric layer thickness	10 μm
Barrier rib height	120 μm
Barrier rib width	40 μm
Phosphor thickness	12 μm
Pixel size	$480 \times 160\ \mu m^2$

angle of 45° using a concentric hemispherical analyzer with pass energies of 69 eV for C-, O-, and Mg-related photoelectrons and 140 eV for Ca-related photoelectrons. The surfaces of the samples were neutralized by a combination of electrons and an Ar^+ beam to suppress charging effects during the XPS measurements [16]. Software for XPS analysis (MultiPak, ULVAC PHI) was used to subtract background signals for all photoelectron spectra according to the Shirley background [17]. Binding energies for the spectra were corrected by shifting the binding energy of hydrocarbon-related peaks at the C 1s photoelectron line to 284.8 eV [18]. C-, O-, Mg-, and Ca-related photoelectron signal intensities were corrected by setting the relative sensitivity factors over the regions being assessed to 21.479, 50.3, 13.546, and 76.596 provided by the MultiPak software, respectively.

2.3 Results and Discussion

A discharge sustaining voltage (V_{sus}) and a luminous efficiency were measured for panels with MgO and (Mg,Ca)O protective layers produced under various conditions. A high luminous efficiency of approximately 1.6 lm/W was obtained for both MgO and (Mg,Ca)O protective layers. This is attributed to the enhancement of a VUV generation efficiency due to the setting of the Xe content in the discharge gas to 100%. V_{sus} with a conventional MgO protective layer was stable at approximately 250 V; however, the variation in V_{sus} was much larger for the (Mg,Ca)O protective layer than for the conventional MgO layer. There were also panels with higher V_{sus}, while lower V_{sus} was realized as expected; the difference between the minimum and maximum V_{sus} values was approximately 85 V.

To investigate the reason for the above-mentioned variation in V_{sus}, the panels with various V_{sus} values were dismantled and the surfaces of the (Mg,Ca)O protective layers were analyzed by XPS. One of the difficulties in the analysis of protective layer surfaces is the effects of the adsorption of impurity gas from the air during the dismantling of the panels until the samples are introduced into the measurement chamber. To suppress the adsorption of H_2O in particular, the samples were dismantled in dry air and stored in a N_2 atmosphere until the measurements. In addition, to take into account both chemical and physical adsorptions, not only Mg- and Ca-related photoelectron spectra but also C- and O-related photoelectron spectra were measured, and the relationship between V_{sus} values and the adsorption states obtained from each spectrum was investigated. The C 1s, O 1s, Mg 2p, and Ca 2s photoelectron spectra results for panel Nos. 1, 2, and 3 with respective V_{sus} values of 210, 237, and 262 V are shown in Figs. 2.3(a)-2.3(d), respectively. The production conditions of these panels are summarized in Table 2.2. The C 1s and O 1s photoelectron spectra were measured to quantify the amounts of C=O, C−H (or C−C), and O−H bonding states adsorbed on the (Mg,Ca)O protective layer. The chemical

Table 2.2: Production conditions and V_{sus} values for panel Nos. 1, 2, and 3.

Condition	Panel No. 1	Panel No. 2	Panel No. 3
CaO conc. (mol%)	12	12	12
Annealing atmosphere prior to panel sealing	Vacuum	Air	Air
Annealing atmosphere during panel sealing	N_2	N_2	Air
V_{sus} (V)	210	237	262

states of Mg and Ca were characterized by analyzing Mg 2p and Ca 2s photoelectron spectra. Mg 2p photoelectrons provide one of the most intense lines for Mg, whereas Ca 2s photoelectrons do not provide such an intense line for Ca. The kinetic energy of Ca 2p photoelectrons, which show the most intense line for Ca, overlaps with that of Mg KLL Auger electrons when using the Al Kα line as an X-ray excitation source; therefore, the Ca 2s photoelectron line was analyzed instead. The spectra were normalized with respect to the peak values of Mg-related signals in Fig. 2.3(a) and each photoelectron peak in Figs. 2.3(b)-2.3(d).

Figure 2.3(a) shows three peaks obtained in C 1s photoelectron spectra. The peaks with binding energies of approximately 290 and 285 eV can be assigned to C=O and C−H (or C−C) bonding states, respectively [19,20]. Mg-related Auger electron lines appear as a broad peak at approximately 282 eV in the case of Al Kα X-ray excitation [21]. The O 1s photoelectron spectra in Fig. 2.3(b) have peaks with shoulders on the high-binding-energy side. The bonding states of O atoms at binding energies of approximately 529, 531, and 532 eV are assigned to Mg or Ca oxidation, O−H, and C=O bonding states, respectively [20,22]. The Mg 2p photoelectron spectra shown in Fig. 2.3(c) have a chemical state assigned to Mg oxidation at a binding energy of 49 eV [20], which remains almost unchanged, despite the change in V_{sus}. On the other hand,

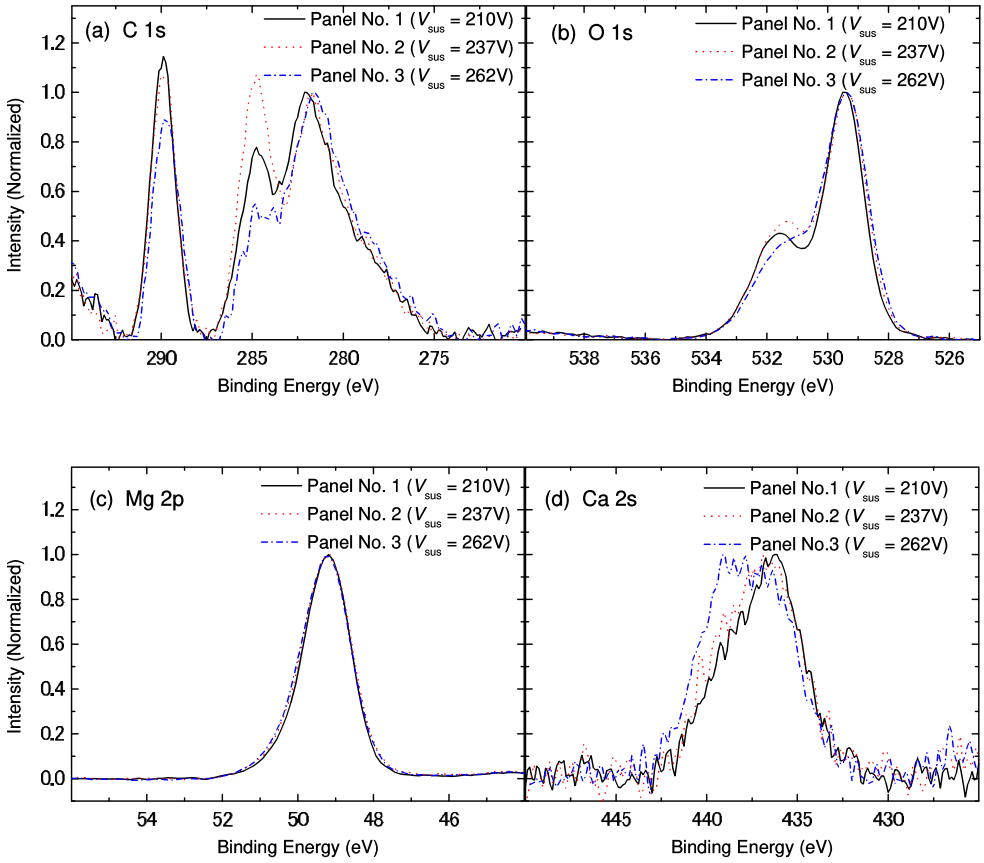

Figure 2.3: (a) C 1s, (b) O 1s, (c) Mg 2p, and (d) Ca 2s photoelectron spectra for (Mg,Ca)O protective layers from panel Nos. 1, 2, and 3 with V_{sus} values of 210, 237, and 262 V, respectively.

the Ca 2s photoelectron spectra shift to higher binding energies with increasing V_{sus}, as shown in Fig. 2.3(d). It is assumed that this shift to a higher binding energy of approximately 439 eV in the Ca 2s photoelectron spectra is related to the carbonation state of Ca [22,23] owing to the relatively high chemisorption nature of CO_2 toward Ca [24,25]. The lower binding energy of the Ca 2s photoelectron line at approximately 436 eV is attributed to the oxidation state of Ca [22].

By fitting the spectra in Figs. 2.3(a) and 2.3(b) with Gaussian functions, the amounts of the C=O, C−H (or C−C), and O−H bonding states adsorbed on the (Mg,Ca)O protective layers can be calculated. Although the amount of the C=O bonding state can be obtained from both C 1s and O 1s photoelectron spectra, it was calculated from the C 1s spectra. The ratio of Ca carbonation $[G_c/(G_o + G_c)]$ can also be estimated by fitting the Ca 2s photoelectron spectra with two Gaussian functions for the oxidation (G_o) and carbonation states (G_c). Figures 2.4(a)-2.4(c) show the relationship between V_{sus} values and the amounts of the C=O, C−H, and O−H bonding states adsorbed on the (Mg,Ca)O protective layer, respectively. These amounts are normalized according to the sum of the Mg and Ca signals, because the absolute values of the spectra can be varied among the samples due to the charging effects. The relationship between V_{sus} values and the Ca carbonation ratio $G_c/(G_o + G_c)$ is also shown in Fig. 2.4(d), where the dotted line is a linear fit. The relationship between V_{sus} values and the amounts of the C=O, C−H, and O−H bonding states is very poor, while V_{sus} values well correlate with the Ca carbonation ratio. Figure 2.4(d) shows that, as the Ca carbonation is enhanced, V_{sus} increases. The analysis of the depth profiles of photoelectron signals from carbon has revealed that the amounts of carbon at the surface is related to the discharge voltage for a (Mg,Ca)O protective layer with different CaO concentrations [26]. The obtained results in this study directly demonstrate that the (Mg,Ca)O protective layer in the panel does not carbonate at

Mg sites, but predominantly at Ca sites; the carbonation ratio is clearly related to the discharge voltage, even at the same CaO concentration.

As shown in Figs. 2.4(a) and 2.4(d), V_{sus} values well correlate with Ca carbonation ratio but not with the amounts of C=O bonding state. The reason for this is thought to be as follows. The spectral shift in Ca 2s photoelectron spectra is caused only by chemical adsorption, because the Ca bonding state is modified only by chemical reactions. In contrast, C 1s photoelectron signals arise from both physical and chemical adsorptions, and it is difficult to separate the spectra from each other. The amount of adsorption of impurity species varies with exposure time in air from the dismantling of the panels until the measurements are performed, especially in the case of rapid physical adsorption. Therefore, the amounts of the C=O bonding state which are not originally present in the panels may largely be detected in C 1s photoelectron spectra. It can also be explained similarly why V_{sus} values do not well correlate with the amounts of the C−H and O−H bonding states as shown in Figs. 2.4(b) and 2.4(c) because the photoelecton signals from their bonding states are also caused by physical adsorption. Therefore, it is considered that Ca 2s photoelectron spectra are more suitable for the quantification of the amount of the adsorption in the panels because chemical adsorption proceeds more slowly than physical adsorption.

Considering the results shown in Fig. 2.4(d), the good correlation between V_{sus} values and the amounts of carbonated (Mg,Ca)O can be explained by an electron emission with the Auger neutralization [27,28]. Figure 2.5 shows a schematic energy diagram of the electron emission processes from bulk MgO by the Auger neutralization for Ne^+ and Xe^+. In these processes, a wider band gap indicates lower γ if the electron affinity is equivalent. The wide band gap for bulk MgO indicates that an electron emission is effective via Ne^+, but not via Xe^+. However, the band gap at the surface in a thin film is reduced owing to crystal structure imperfections, which generate extra states in the band gap. Therefore, an electron emission from the surface

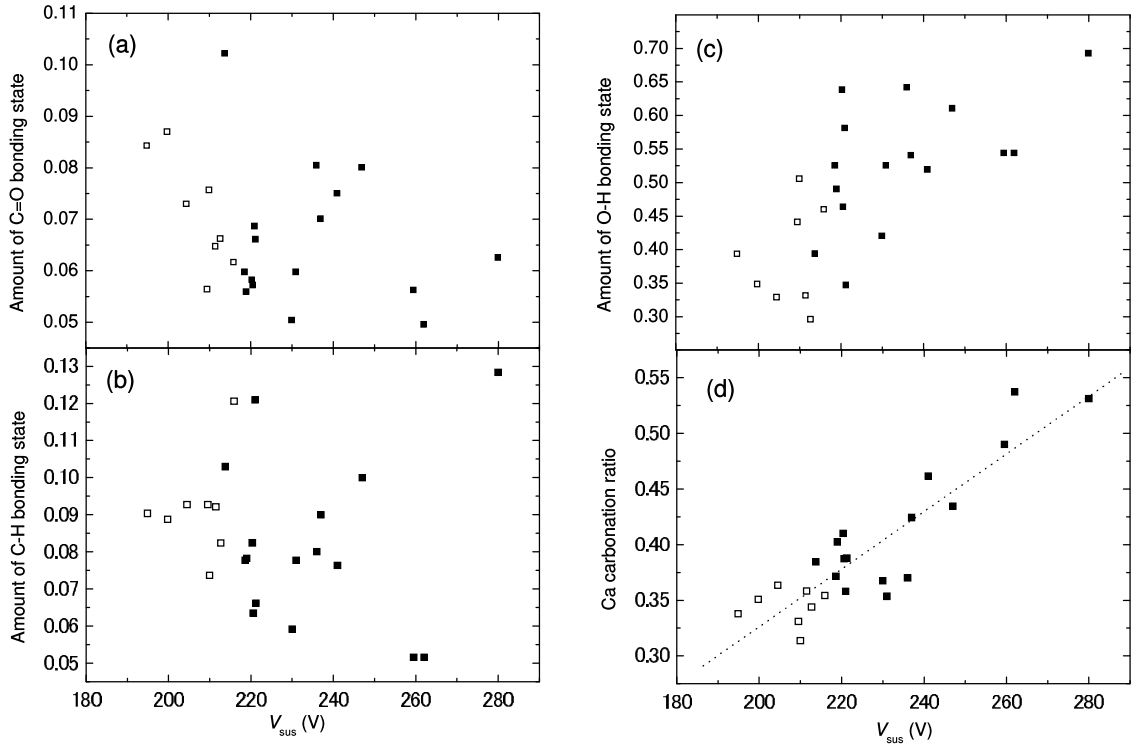

Figure 2.4: Relationship between V_{sus} values and the amounts of the (a) C=O, (b) C−H, and (c) O−H bonding states normalized with respect to sum of the Mg and Ca amounts, and (d) the Ca carbonation ratio $G_{\mathrm{c}}/(G_{\mathrm{o}}+G_{\mathrm{c}})$ on (Mg,Ca)O protective layers. Squares correspond to experimentally obtained data, while the dotted line shows a linear fit. Open symbols correspond to data from the panels annealed in vacuum, while closed symbols to data obtained under other annealing conditions.

state of MgO can be slightly effective, even for Xe^+. The band gaps of MgO, $MgCO_3$, CaO, and $CaCO_3$ were estimated by computational simulations of the density of states using the WIEN2k program [29]. Although these values are somewhat different from the actual values because of the limits of the band theory calculations, the relative changes in band gaps from the oxidation states to the carbonation states for Mg and Ca can be discussed. The relative band gaps of MgO:CaO, MgO:$MgCO_3$, and CaO:$CaCO_3$ were determined to be 1:0.77, 1:1.04, and 1:1.38, respectively. A comparison of MgO with CaO indicates that the higher γ for CaO is explained by its narrower band gap. The degradation of γ is noticeable owing to the formation of a much wider band gap by the carbonation of CaO than by that of MgO. These results suggest that the band gap is narrower for (Mg,Ca)O than for MgO, which leads to higher γ, but the band gap is significantly increased by carbonation, which results in lower γ and higher V_{sus}.

To understand the progression of the chemical carbonation of Mg and Ca in various atmospheres, (Mg,Ca)O films were exposed to N_2, dry air, and normal air atmospheres for 14 days immediately after deposition, and the surfaces were then analyzed by XPS. The Mg 2p and Ca 2s photoelectron spectra are shown in Figs. 2.6(a) and 2.6(b), respectively. The spectra are also normalized with respect to the peak values. The $G_c/(G_o + G_c)$ ratios obtained from Fig. 2.6(b) are shown in Table 2.3. The Mg 2p photoelectron peaks show that the carbonation of Mg proceeds only in the air atmosphere [30]. This carbonation can be reversed by annealing in air at 350°C. The possible reason why the V_{sus} of a conventional panel with a MgO protective layer is stable is the reversal from the carbonation to oxidation of Mg by annealing in air, even if the carbonation of Mg proceeds.

On the other hand, the Ca 2s photoelectron peaks indicate that the chemical state of Ca remains unchanged only in the N_2 atmosphere. Although Ca carbonation proceeds readily in normal air, the carbonation is suppressed to some extent in dry air. Therefore, it is suggested

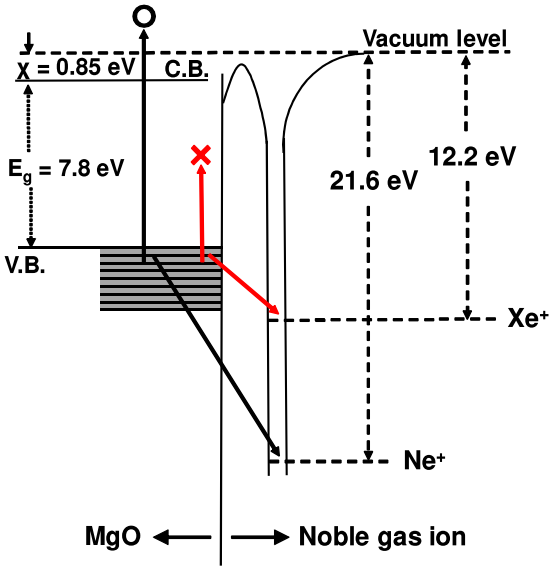

Figure 2.5: Schematic energy diagram for electron emission processes from bulk MgO by the Auger neutralization via Ne^+ and Xe^+.

that H_2O in air enhances Ca carbonation because it has been reported that moisture is often added to the CaO carbonation process to increase the reaction rate owing to the formation of the $Ca(OH)_2$ intermediate [31,32]. In addition, the carbonation of Ca is not reversed by oxidation owing to annealing in air at 350°C, but is enhanced slightly. Extreme ultraviolet photoelectron spectroscopy (EUPS) measurements of MgO and CaO showed that the amount of CO_2 adsorbed was increased by annealing in air for CaO, but not for MgO [33]. Metastable de-excitation spectroscopy (MDS) measurements showed that the ionization potential was almost unchanged for MgO, but significantly increased for CaO by annealing in air [34]. The results of the annealing of (Mg,Ca)O thin films in air in this study are similar to those of MgO and CaO films measured by EUPS and MDS. It is suggested that the reversal of Ca carbonation

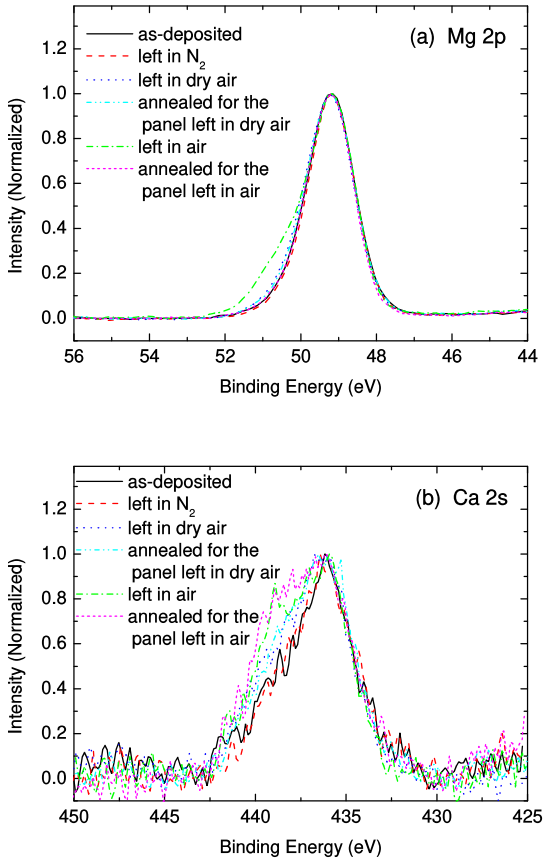

Figure 2.6: (a) Mg 2p and (b) Ca 2s photoelectron spectra of (Mg,Ca)O films after exposure to N_2, dry air, and normal air atmospheres for 14 days after deposition. Spectra of the as-deposited sample and the samples annealed in air at 350°C after exposure to dry air and normal air atmospheres are also shown.

Table 2.3: Ca carbonation ratios $[G_c/(G_o + G_c)]$ obtained from Fig. 2.6(b).

Condition	G_c / (G_o + G_c)
As-deposited	0.29
Left in N_2	0.3
Left in dry air	0.35
Annealed for the panel left in dry air	0.37
Left in air	0.45
Annealed for the panel left in air	0.49

by annealing in air is impossible, which is the reason why the V_{sus} of panels with (Mg,Ca)O protective layers is unstable because there are differences in the degree of Ca carbonation under various production conditions and exposure time in the atmosphere after (Mg,Ca)O deposition. This is considered to be critical for (Mg,Ca)O protective layers because detailed control of exposure time in the atmosphere after deposition, i.e., the degree of Ca carbonation, is difficult during the production.

It is thus necessary to introduce a process to overcome this problem to the production of the (Mg,Ca)O protective layer. The decarbonation and carbonation behaviors of air-annealed (Mg,Ca)O films were investigated using various additional annealing procedures in N_2, vacuum, N_2:H_2O, N_2:CH_4, and N_2:CO_2 atmospheres at 500°C. The pressure for vacuum annealing was in the range from 10^{-5} to 10^{-4} Torr. N_2 and the mixture gases were continuously supplied during annealing with the flow rate of 10 L/min. The N_2:H_2O gas flow was realized by bubbling pure water with N_2 gas. Figures 2.7(a) and 2.7(b) show the Mg 2p and Ca 2s photoelectron spectra of the (Mg,Ca)O films with the additional annealing after annealing in air, respectively; the

spectrum for annealing in air indicates the initial chemical state of this trial. The $G_c/(G_o+G_c)$ ratios obtained from Fig. 2.7(b) are shown in Table 2.4. For both Mg and Ca, the photoelectron spectral shift to higher binding energy was more significant after annealing in the N_2:CO_2 atmosphere. Annealing in the N_2:CH_4 or N_2:H_2O atmosphere leads to larger chemical shift to high binding energy for Ca than for Mg. The spectral changes induced by annealing in the N_2:CO_2 atmosphere are due to the carbonation of Mg and Ca [22,23,30]. The chemical state of Ca is also changed, even in the N_2:CH_4 or N_2:H_2O atmosphere. It has been reported that the ionization potential of CaO is changed by the adsorption of H_2O or CO_2, as confirmed by MDS measurements [35]. The degree of increase of the ionization potential by H_2O or CO_2 adsorption is similar to that of the chemical shift to high binding energy after annealing in N_2:CO_2 or N_2:H_2O gas. This suggests that the change in the chemical bonding state of Ca by H_2O or CO_2 chemisorption leads to an increase in ionization potential. Similarly, it is considered that the ionization potential is increased by the changes in the chemical bonding states of Ca due to CH_4 chemisorption [36]. These results indicate that not only CO_2 gas but also moisture and organic compound gases remaining in the annealing atmosphere should be removed as much as possible to suppress an increase in ionization potential and the degradation of γ of the (Mg,Ca)O protective layer.

On the other hand, carbonation can be reversed by annealing both in N_2 atmosphere and in vacuum. Annealing in vacuum was the most effective process for the decarbonation of the (Mg,Ca)O films, because the activation energy for the decarbonation of $CaCO_3$ is modified and the actual pressure of the thermally desorbed CO_2 is greatly reduced to less than the equilibrium pressure between the carbonation and decarbonation reactions especially in vacuum [26,37]. In Fig. 2.4(d), data from panels with (Mg,Ca)O protective layers annealed in vacuum are also plotted with open symbols. These data are obtained at V_{sus} values from 195 to 215 V in the region

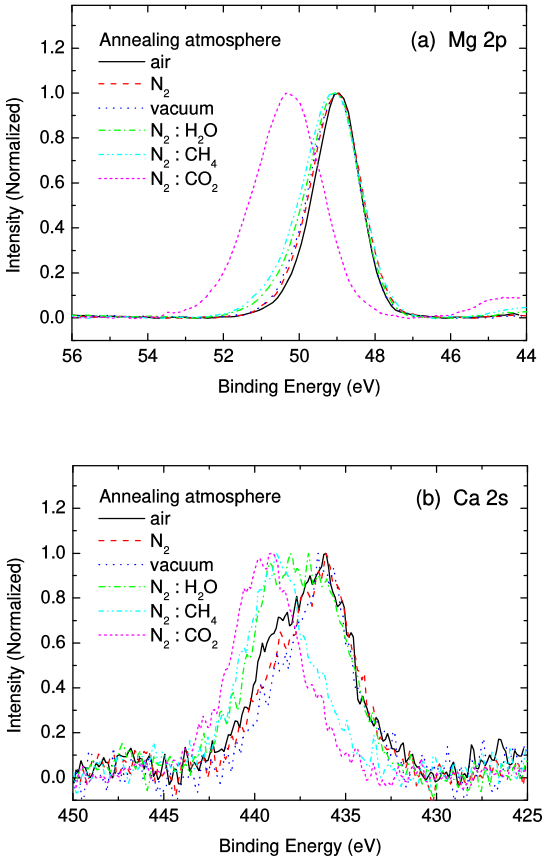

Figure 2.7: (a) Mg 2p and (b) Ca 2s photoelectron spectra of (Mg,Ca)O films with the additional annealing in N_2, vacuum, N_2:H_2O, N_2:CH_4, and N_2:CO_2 atmospheres after annealing in air. The spectrum for annealing in air indicates the initial chemical state of this trial. The annealing temperatures were 350°C in air and 500°C in the other atmospheres.

Table 2.4: Ca carbonation ratios $[G_c/(G_o+G_c)]$ obtained from Fig. 2.7(b).

Annealing atmosphere	G_c / $(G_o + G_c)$
Air	0.43
N_2	0.35
Vacuum	0.29
N_2:H_2O	0.57
N_2:CH_4	0.86
N_2:CO_2	0.97

of low carbonation ratio of the (Mg,Ca)O protective layer. Although V_{sus} was also changed by the species adsorbed on the front or back panel and by the process conditions for panel sealing [11,12], it is demonstrated that annealing of a carbonated (Mg,Ca)O protective layer in vacuum is effective for reducing V_{sus} owing to the decarbonation of Ca.

In the conventional production processes for plasma discharge devices, organic residues can be removed by annealing the panel in air. As described above, organic residues should be removed because the chemical states and γ at the (Mg,Ca)O surface are modified by the organic compounds desorbed during the panel sealing process at high temperatures. However, annealing in vacuum is considered to be ineffective for removing organic residues owing to a lack of O_2. In Fig. 2.8, C 1s photoelectron spectra are shown for the samples annealed in vacuum and in air and vacuum combination after organic contamination. Photoelectron signals related to organic contaminants are mainly detected at a binding energy of approximately 285 eV [19,20]. Thus, significant organic contamination remains on the surface in the case of annealing only in vacuum. However, the amounts of organic contaminants are reduced for the sample annealed in air and vacuum combination. Therefore, annealing only in vacuum cannot be an alternate

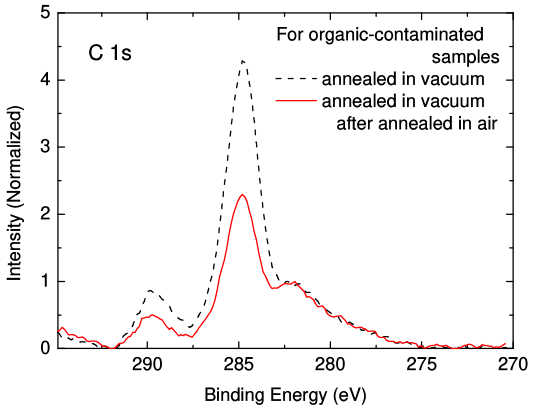

Figure 2.8: C 1s photoelectron spectra of (Mg,Ca)O films annealed in vacuum and in air and vacuum combination after immersion in a solution of α-terpineol. The annealing temperatures were 350°C in air and 500°C in vacuum.

process to annealing in air. It is proposed that the best performance of plasma discharge devices with (Mg,Ca)O protective layers can be realized by the addition of annealing in vacuum before the panel sealing process.

2.4 Conclusions

The quantitative relationships between a discharge sustaining voltage V_{sus} and Ca carbonation ratio, and the decarbonation annealing process of carbonated (Mg,Ca)O protective layers in plasma discharge devices were investigated. There were panels with high V_{sus}, while low V_{sus} was also realized as expected. The results of XPS analyses show that the increase of V_{sus} arises from carbonation of Ca. To suppress Ca carbonation, dry air is a more suitable atmosphere

than humid air for exposure. The carbonation of Ca cannot be reversed by annealing in the air atmosphere at an accessible temperature; therefore, annealing in vacuum is proposed for the decarbonation of (Mg,Ca)O protective layers, which results in the lowering of V_{sus}. The additional process of annealing in vacuum after annealing in air should be performed immediately before panel sealing for the production with (Mg,Ca)O protective layers to satisfy both the removal of organic residues on the protective layer during production and the decarbonation of (Mg,Ca)O films.

References

[1] J. Cho, R. Kim, K.-W. Lee, G.-Y. Yeom, J.-Y. Kim, J.-W. Park, Effect of CaO addition on the firing voltage of MgO films in AC plasma display panels, Thin Solid Films 350 (1999) 173-177.

[2] T. Zukawa, K. Yoshino, Y. Oe, H. Kawarazaki, K. Aoto, Y. Tanaka, R. Murai, Development of MgCaO Protective Layer of Plasma Display Panels for Decreased Discharge Voltage, SID Int. Symp. Dig. Tech. Pap. 43 (2012) 165-167.

[3] T.-H. Lee, H.-W. Cheong, O. Kwon, K.-W. Whang, Application of MgCaO Cathode Layer to Plasma Display Panel for High Luminous Efficacy, IEEE Trans. Electron Devices 60 (2013) 301-304.

[4] Q. Yan, K. Kotera, H. Zhao, H. Liu, H. Zhou, Y. Tang, X. Deng, Calcium Magnesium Oxide Nano-crystal (Nano-CMO) for Improving Uniformity of High Xe Content PDP, SID Int. Symp. Dig. Tech. Pap. 45 (2014) 208-211.

[5] C.-S. Park, E. Y. Jung, H.-S. Tae, Improvement of luminous efficiency using Li-doped MgO layer coated by MgCaO crystal powders in plasma display panels, Mol. Cryst. Liq. Cryst. 645 (2017) 130-137.

[6] J. W. Lee, Calculation of the Secondary Electron Emission Coefficients of MgO, MgBeO, MgCaO, MgSrO and MgBaO Induced by Auger Neutralization of He^+, Ne^+, Ar^+ and Xe^+ Ions, New Phys.: Sae Mulli 68 (2018) 939-944.

[7] Y. Motoyama, D. Kato, M. Seki, An AC PDP with an Air-Stable CaMgO Prorective Layer, Proc. 17th Int. Disp. Workshops 2 (2010) 959-960.

[8] R. M. Caloi, C. Carretti, Getters and gettering in plasma display panels, J. Vac. Sci. Technol. A 16 (1998) 1991-1997.

[9] Q. Yan, Z. Lu, F. Xing, X. Zhang, C. Tang, L. Chen, X. Deng, D. Peng, Processing issues of $Ca_xMg_{1-x}O$ (CMO) protecting layer for high luminous efficacy PDP, Proc. 18th Int. Disp. Workshops 1 (2011) 229-230.

[10] Q. Yan, K. Kotera, P. Wang, Z. Lu, F. Xing, C. Tang, L. Chen, D. Xue, X. Deng, Manufacture issues of implementing $Ca_xMg_{1-x}O$ protecting layer for high efficiency AC PDP, Proc. 19th Int. Disp. Workshops 2 (2012) 692-695.

[11] H.-N. Choi, S.-Y. Kim, Y.-H. Kim, S. Jeong, Y.-S. Kim, Characteristics of (Mg, Ca)O Thin Film Layer Sealed under Nitrogen Atmosphere, SID Int. Symp. Dig. Tech. Pap. 42 (2011) 637-640.

[12] S. Jeong, J.-S. Kim, Y.-S. Kim, Effects of Sealing Conditions and CaO Contents on Aging Behavior of AC-PDP with (Mg,Ca)O Protective Layer, SID Int. Symp. Dig. Tech. Pap. 44 (2013) 131-133.

[13] L. Vegard, Die Konstitution der Mischkristalle und die Raumfüllung der Atome, Z. Phys. 5 (1921) 17-26.

[14] A. R. Denton, N. W. Ashcroft, Vegard's law, Phys. Rev. A 43 (1991) 3161-3164.

[15] M. Amatsuchi, A. Hirota, H. Lin, T. Naoi, E. Otani, H. Taniguchi, K. Amemiya, Discharge Time Lag Shortening by Using a New Material Layer in AC PDP, Proc. 12th Int. Disp. Workshops 1 (2005) 435-438.

[16] P. E. Larson, M. A. Kelly, Surface charge neutralization of insulating samples in x-ray photoemission spectroscopy, J. Vac. Sci. Technol. A 16 (1998) 3483-3489.

[17] D. A. Shirley, High-Resolution X-Ray Photoemission Spectrum of the Valence Bands of Gold, Phys. Rev. B 5 (1972) 4709-4714.

[18] P. Swift, Adventitious Carbon - The Panacea for Energy Referencing?, Surf. Interface Anal. 4 (1982) 47-51.

[19] S. L. Stipp, M. F. Hochella Jr., Structure and bonding environments at the calcite surface as observed with X-ray photoelectron spectroscopy (XPS) and low energy electron diffraction (LEED), Geochim. Cosmochim. Acta 55 (1991) 1723-1736.

[20] F. Khairallah, A. Glisenti, XPS Study of MgO Nanopowders Obtained by Different Preparation Procedures, Surf. Sci. Spect. 13 (2006) 58-71.

[21] J. C. Fuggle, L. M. Watson, D. J. Fabian, S. Affrossman, X-ray excited Auger and photoelectron spectra of magnesium, some alloys of magnesium and its oxide, J. Phys. F: Met. Phys. 5 (1975) 375-383.

[22] R. Nowosielski, A. Bajorek, R. Babilas, Corrosion behavior of bioresorbable Ca-Mg-Zn bulk metallic glasses, J. Non-Cryst. Solids 447 (2016) 126-133.

[23] M. Engelhard, D. Baer, Vacuum Cleaved Calcium Carbonate by XPS, Surf. Sci. Spect. 6 (1999) 153-159.

[24] D. Ochs, M. Brause, B. Braun, W. Maus-Friedrichs, V. Kempter, CO_2 chemisorption at Mg and MgO surfaces: a study with MIES and UPS(He I), Surf. Sci. 397 (1998) 101-107.

[25] D. Ochs, B. Braun, W. Maus-Friedrichs, V. Kempter, CO_2 chemisorption at Ca and CaO surfaces: a study with MIES, UPS(HeI) and XPS, Surf. Sci. 417 (1998) 406-414.

[26] Y. Motoyama, D. Kato, N. Saito, M. Seki, Carbonation reaction of (Ca, Mg)O protective layer on plasma display panel, J. Soc. Inf. Disp. 21 (2013) 41-45.

[27] H. D. Hagstrum, Theory of Auger Neutralization of Ions at the Surface of a Diamond-Type Semiconductor, Phys. Rev. 122 (1961) 83-113.

[28] M. O. Aboelfotoh, J. A. Lorenzen, Influence of secondary-electron emission from MgO surfaces on voltage-breakdown curves in Penning mixtures for insulated-electrode discharges, J. Appl. Phys. 48 (1977) 4754-4759.

[29] M. Sakai, S. Hatta, Y. Fukui, Y. Honda, M. Okafuji, Y. Yamauchi, M. Nishitani, Y. Tanaka, Analysis of the Deterioration of Secondary Electron Emission Coefficient of Protective Layers Formed by Alkaline-Earth Oxides for Plasma Display Panels, Proc. 15th Int. Disp. Workshops 3 (2008) 1881-1884.

[30] S. Ardizzone, C. L. Bianchi, M. Fadoni, B. Vercelli, Magnesium salts and oxide: an XPS overview, Appl. Surf. Sci. 119 (1997) 253-259.

[31] V. Manovic, E. Anthony, Steam Reactivation of Spent CaO-Based Sorbent for Multiple CO_2 Capture Cycles, Environ. Sci. Technol. 41 (2007) 1420-1425.

[32] L. Zhang, B. Zhang, Z. Yang, M. Guo, The Role of Water on the Performance of Calcium Oxide-Based Sorbents for Carbon Dioxide Capture: A Review, Energy Technol. 3 (2015) 10-19.

[33] T. Nakayama, M. Terauchi, K. Yoshino, T. Tsujita, M. Nishitani, T. Ishituka, T. Tomie, Y. Morita, Characterization of Protective Layer Materials for Plasma Display Panels by the EUPS Observation, Proc. 17th Int. Disp. Workshops 3 (2010) 1963-1966.

[34] K. Yoshino, Y. Morita, T. Nagatomi, M. Terauchi, T. Tsujita, Y. Doi, T. Nakayama, Y. Yamauchi, M. Nishitani, M. Kitagawa, Y. Takai, Y. Yamauchi, Investigation of Effects of Heating in Air on Ionization Potential of MgO and CaO Films using Metastable De-excitation Spectroscopy, SID Int. Symp. Dig. Tech. Pap. 42 (2011) 641-644.

[35] K. Yoshino, Y. Morita, T. Nagatomi, M. Terauchi, T. Tsujita, Y. Doi, T. Nakayama, Y. Yamauchi, M. Nishitani, M. Kitagawa, Y. Yamauchi, Y. Takai, Changes in ionization potentials of MgO and CaO films upon heating in air and vacuum investigated by metastable de-excitation spectroscopy, Appl. Surf. Sci. 259 (2012) 135-141.

[36] H.-Q. Yang, C.-W. Hu, S. Qin, Theoretical study on the reaction mechanism of CH_4 with CaO, Chem. Phys. 330 (2006) 343-348.

[37] K. H. Stern, E. L. Weise, High Temperature Properties and Decomposition of Inorganic Salts. Part 2. Carbonates, Nat. Stand. Ref. Data Ser., Nat. Bur. Stand. (U.S.) 30, U.S. GPO, Washington, D.C., 1969, pp. 4-10.

Chapter 3

Shrinkage and expansion of discharge area by (Mg,Ca)O protective layer for plasma discharge device

In this chapter, the modification of the discharge area in flat panel plasma discharge devices having (Mg,Ca)O protective layers on prolonged aging was demonstrated. The discharge area shrank and the discharge intensity reduced during aging. The CaO concentration increased at the layer surface by the preferential sputtering of MgO, which is promoted by higher Xe levels in the discharge gas. These results indicate that a modified distribution of the secondary electron emission property at the surface due to the compositional change leads to the shrinkage of the discharge area. This work also demonstrates that reducing the permittivity of the dielectric layer under the protective layer expands the discharge area, thus suppressing the degradation of the discharge intensity in the plasma discharge devices.

3.1 Introduction

The scope of this chapter is temporal changes in a discharge behavior and a luminous efficiency of plasma discharge devices with complex oxide protective layers by prolonged aging. As described in Chapter 1, mixed crystals of alkaline-earth metal oxides have been studied for a long time in order to satisfy both chemical stability and high γ for Xe^+ as alternatives of a conventional MgO material. Enhancement of a luminous efficiency by using the complex oxide protective layer, such as (Mg,Ca)O [1-3], (Mg,Sr)O [4], and (Sr,Ca)O [5-7], has been reported. However, these results are limited at the initial state of the operation. Therefore, it is very meaningful to investigate the degradation of a discharge behavior and a luminous efficiency by prolonged aging when complex oxide protective layers are used.

In the case of a conventional MgO protective layer, the temporal change in a luminous efficiency mainly arises from the degradation of phosphors due to surface damages induced by both VUV irradiation and ion sputtering during panel aging [8-10]. Modifications of a discharge behavior and a discharge efficiency in the panel with a MgO protective layer by the aging are relatively limited because it has been reported that little degradation of γ occurs by sputtering the surface of the protective layer [11,12]. However, the effects on a discharge efficiency and panel characteristics modification by prolonged aging for the complex oxide protective layers have yet to be investigated. Moreover, a suitable process and a device structure to improve the properties of plasma discharge devices with the complex oxide protective layers have never been proposed.

In this work, the modifications of a discharge behavior and a luminous efficiency by prolonged aging for flat panel plasma discharge devices with complex oxide protective layers are investigated. PDPs were employed to evaluate the discharge modification. The shrinkage and expansion of the discharge area for the devices with the complex oxide protective layers af-

ter prolonged aging are demonstrated. Analyzing the surface of the sputtered protective layers enables the modification mechanisms of the discharge behaviors to be identified. Moreover, the effective pixel structures to suppress the degradation of the device efficiency due to the modification of discharge behaviors are also proposed.

3.2 Experimental Methods

The discharge behavior of plasma discharge devices with complex oxide protective layers during aging was investigated using 42-inch FHD AC PDPs. (Mg,Ca)O was employed as the complex oxide protective layer because this is currently considered to be the most promising material in devices having high Xe concentrations in the discharge gas (so as to achieve both an increased VUV radiation generation efficiency and a low discharge voltage) [1-3,13]. The improved performance by (Mg,Ca)O is due to higher γ compared to those of MgO for not only plasma displays but also other plasma discharge devices. A (Mg,Ca)O film with a thickness of 800 nm was deposited on the dielectric layer by electron beam evaporation. The permittivity and thickness of the dielectric layer (ε_d and d_d) were 11.3 and 39 μm, respectively. The evaporation targets were sintered mixtures of MgO and CaO. The CaO concentrations in the resulting films were in the range from 3.0 to 17.8 mol% depending on the ratio of the two oxides in the target. Following (Mg,Ca)O deposition, MgO powders were dispersed on the protective layer to improve the statistical discharge delay [14]. A Ne:Xe mixture was used as a discharge gas, with the Xe concentration of 15% and at the pressure in the panel of 450 Torr. The specifications of the test panels used in this study are provided in Table 3.1. Panel aging tests were carried out under accelerated conditions, although the aging times reported herein correspond to the actual operational time spans. The panels were dismantled and then cut into the pieces at the size of a few cm^2 for the following measurement.

Table 3.1: Specifications of the test panels used in this study.

Front Panel	
ITO electrode width	110 μm
Bus electrode width	65 μm
Electrode gap	80 μm
Dielectric layer thickness	39 μm
Protective layer thickness	800 nm
Back Panel	
Address electrode width	65 μm
Dielectric layer thickness	10 μm
Barrier rib height	120 μm
Barrier rib width	40 μm
Phosphor thickness	12 μm
Pixel size	480 × 160 μm^2

The CaO concentrations at the surfaces of the (Mg,Ca)O protective layers were estimated by XPS (PHI Quantera SXM, ULVAC PHI). The samples were excited by a monochromatic X-ray source with an Al Kα line at 1486.7 eV. The sample surfaces were neutralized with a combination of electrons and an Ar^+ beam to suppress charging effects during the XPS measurements [15]. The photoelectron signals from the samples were detected at a take-off angle of 45° using a concentric hemispherical analyzer with pass energies of 69 eV for Mg-related photoelectrons and 140 eV for Ca-related photoelectrons. Mg 2p and Ca 2s photoelectron spectra were analyzed to calculate the CaO concentration. Mg 2p photoelectrons provide one of the most intense lines for Mg. For Ca, Ca 2s line was employed because the kinetic energy of the most intense Ca 2p lines overlaps with that of Mg KLL Auger electrons when using an Al Kα line as an X-ray excitation source. Mapping measurements of the CaO concentration were carried out by scanning a focused X-ray beam with a spot size of 18 μm at 20 μm intervals. A

software package intended for XPS analysis (MultiPak, ULVAC PHI) was used to subtract the Shirley background signals for all photoelectron spectra [16]. Mg 2p and Ca 2s photoelectron signal intensities were corrected by setting the relative sensitivity factors over the regions being assessed to 13.546 and 76.596 provided by the MultiPak software, respectively.

3.3 Results and Discussion

2500 h aging tests were carried out using panels with (Mg,Ca)O protective layers and the discharge behaviors before and after the aging were compared. Figures 3.1(a) and 3.1(b) show discharge images of panel pixels with (Mg,Ca)O protective layers before and after the aging at the same applied voltage, respectively. These images were obtained by capturing the near infrared emission primarily at 823 and 828 nm associated with $Xe(6p[3/2]_2) \rightarrow Xe(6s[3/2]_2)$ and $Xe(6p[1/2]_0) \rightarrow Xe(6s[3/2]_1)$ transitions [17], respectively, using a gated ICCD apparatus comprising an image intensifier (M7971-01, Hamamatsu Photonics) and a digital CCD camera (C8484, Hamamatsu Photonics). In these images, the white region represents the near infrared emission resulting from discharge, while the horizontal black lines are bus electrodes. Shrinkage of the discharge area after the prolonged aging is evident.

To assess the change in the discharge area quantitatively, the discharge area is defined as the number of ICCD camera pixels for which the signal was more than half the maximum infrared emission intensity within the panel. Figure 3.2 plots the relationship between the normalized discharge area and the normalized peak and integrated discharge intensities with respect to the initial area and intensity during aging. The solid and dotted lines correspond to linear fits for the peak and integrated intensities, respectively. As the discharge area shrinks, both the peak and integrated intensities become smaller. Therefore, the shrinkage of the discharge area is the cause of the reduction of the panel luminous efficiency. A luminous efficiency of a plasma

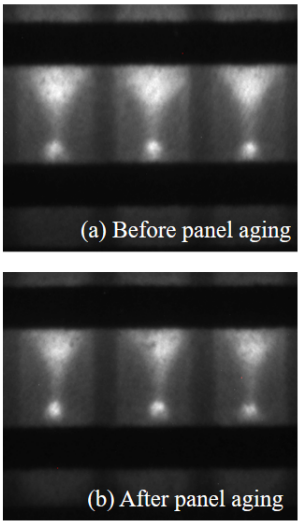

Figure 3.1: Images showing the near infrared emission associated with the Xe discharge from pixels in the panel with a (Mg,Ca)O protective layer (a) before and (b) after aging.

discharge device is also reduced in the case of a conventional MgO protective layer by aging. However, the shrinkage of the discharge area has never been observed.

The shrinkage of the discharge area associated with the (Mg,Ca)O protective layer was investigated by dismantling the aged panels and by analyzing the surfaces using optical microscopy and XPS. The results are shown in Figs. 3.3(a)-3.3(c) for panel aging times of 100, 800, and 2500 h, respectively. Discharge trace images acquired with a digital optical microscope (VHX-500, Keyence) are shown in the upper part, while maps of the surface CaO concentration obtained by XPS at the same areas are shown in the lower part. In the optical microscope images, the black dots are the dispersed MgO powders and the broad horizontal shadows are the embedded bus electrodes. The bulk CaO concentration in the (Mg,Ca)O protective layer in Fig. 3.3 is $\sim$ 11 mol%. It is evident that the surface CaO concentration is greater in the sputtered regions

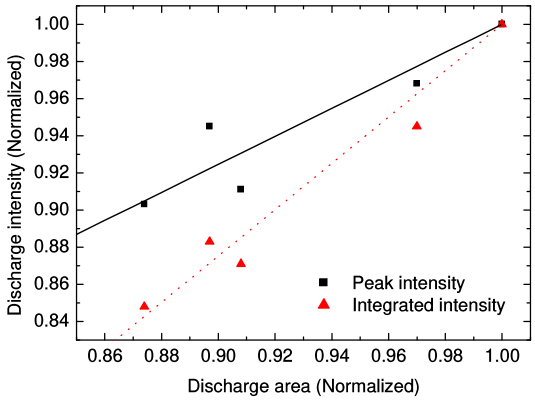

Figure 3.2: Discharge intensities (normalized with respect to the initial intensities) as a function of the discharge area (normalized with respect to the initial area). Squares and triangles correspond to the peak and integrated intensities, respectively, and solid and dotted lines indicate linear fits for the peak and integrated intensities, respectively.

and increases during aging.

γ of the protective layer is expected to be enhanced in the region of an increased CaO concentration [18]. In the region, high γ leads to localized sputtering of the protective layer, resulting in further local increase of the CaO concentration. This process proceeds until the CaO concentration becomes stable. In order to investigate the cause of the CaO concentration increase, CaO concentrations after 2500 h aging for (Mg,Ca)O with different initial CaO concentrations were evaluated. The results are plotted in Fig. 3.4. As expected, higher initial CaO concentration results in higher final CaO concentration.

If it is assumed that the increases of CaO concentrations are caused by the preferential sputtering between MgO and CaO within a (Mg,Ca)O protective layer as schematically illustrated

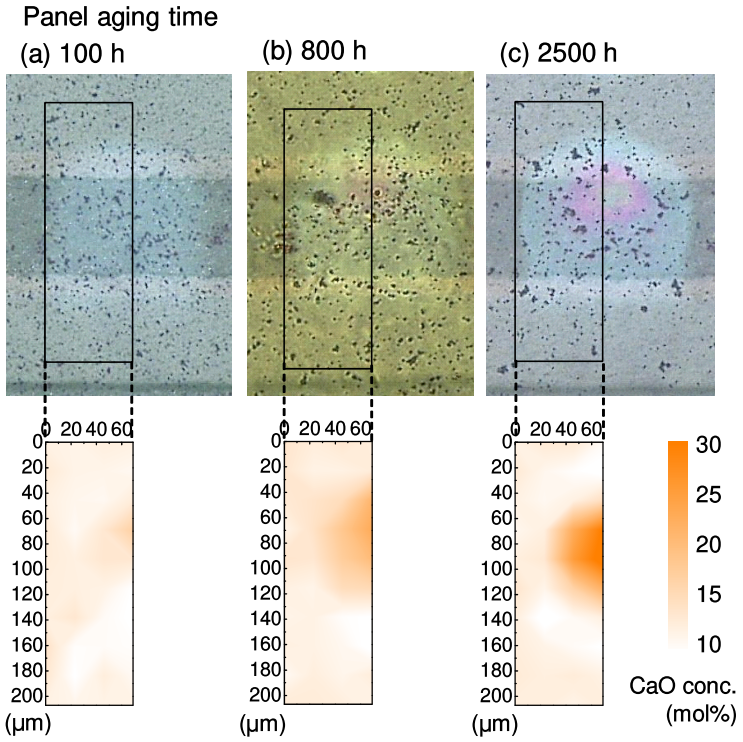

Figure 3.3: Optical microscope images and XPS maps of the CaO concentration in the discharge traces of (Mg,Ca)O protective layers following aging times of (a) 100, (b) 800, and (c) 2500 h.

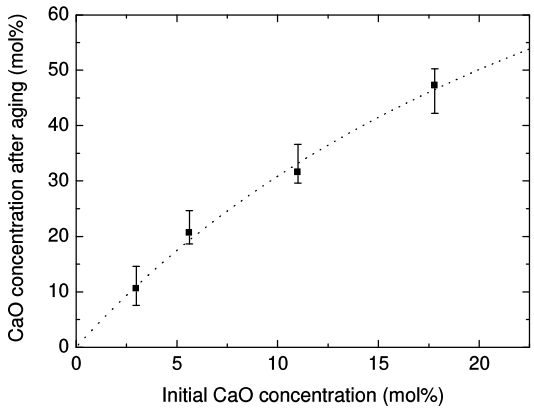

Figure 3.4: CaO concentration in (Mg,Ca)O protective layers after 2500 h aging, as a function of the initial CaO concentration. Square plots correspond to experimental data, while the dotted line indicates the results obtained by calculations using Eq. (3.6), setting Y_{MgO}/Y_{CaO} to 4.02.

in Fig. 3.5, the rate equations of temporal changes of MgO and CaO concentrations ($C_{MgO}(t)$ and $C_{CaO}(t)$, respectively) on the surface of the sputtered (Mg,Ca)O protective layer by the preferential sputtering can be expressed as [19]

$$\frac{dC_{MgO}(t)}{dt} = -C_{MgO}(t)w_{MgO} + N_{MgO}C_{MgO}(t)w_{MgO} + N_{MgO}C_{MgO}(t)w_{CaO}, \tag{3.1}$$

and

$$\frac{dC_{CaO}(t)}{dt} = -C_{CaO}(t)w_{CaO} + N_{CaO}C_{CaO}(t)w_{CaO} + N_{CaO}C_{CaO}(t)w_{MgO}, \tag{3.2}$$

where $C_{MgO}(t) + C_{CaO}(t) = 1$. N_{MgO} and N_{CaO} are the bulk concentrations of MgO and CaO, respectively, where $N_{MgO} + N_{CaO} = 1$. w_{MgO} and w_{CaO} are the sputtering rates of MgO and CaO, respectively. In addition, Eqs. (3.1) and (3.2) can be applied under the assumptions

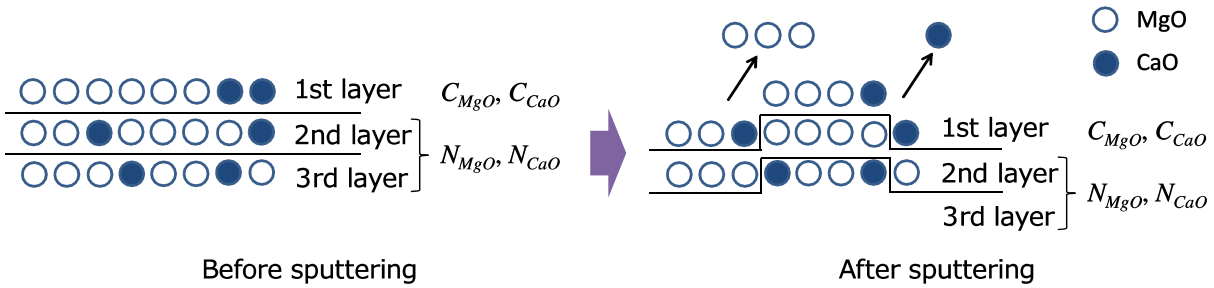

Figure 3.5: Schematic of the model of the preferential sputtering of a (Mg,Ca)O protective layer.

below. Firstly, a (Mg,Ca)O film is a mixture of MgO and CaO. Secondly, only the outermost layer is sputtered by a single sputtering cycle while the material below is not modified. Lastly, the sputtering yields of MgO and CaO (Y_{MgO} and Y_{CaO}, respectively) are independent of the ratio of MgO to CaO. The solutions of Eqs. (3.1) and (3.2) are expressed as

$$C_{MgO}(t) = N_{MgO}\exp(-t/\tau) + N_{MgO}w_{CaO}\tau\left[1-\exp(-t/\tau)\right], \tag{3.3}$$

and

$$C_{CaO}(t) = N_{CaO}\exp(-t/\tau) + N_{CaO}w_{MgO}\tau\left[1-\exp(-t/\tau)\right], \tag{3.4}$$

where $\tau = (N_{MgO}w_{CaO} + N_{CaO}w_{MgO})^{-1}$.

From Eqs. (3.3) and (3.4), the steady-state MgO-to-CaO concentration ratio (C_{MgO}/C_{CaO}) is expressed as

$$\frac{C_{MgO}(t\to\infty)}{C_{CaO}(t\to\infty)} = \frac{N_{MgO}}{N_{CaO}}\frac{w_{CaO}}{w_{MgO}} = \frac{N_{MgO}}{N_{CaO}}\frac{Y_{CaO}}{Y_{MgO}}, \tag{3.5}$$

which leads to

$$C_{CaO}(t\to\infty) = \left(\frac{1-N_{CaO}}{N_{CaO}}\frac{Y_{CaO}}{Y_{MgO}} + 1\right)^{-1}. \tag{3.6}$$

The dotted curve in Fig. 3.4 is the result of the fitting of the data with Eq. (3.6) by using Y_{MgO}/Y_{CaO} as a free fitting parameter. The best result is obtained when Y_{MgO}/Y_{CaO} is 4.02.

The MgO and CaO sputtering yields are affected by both the ionic species (Ne^+ and Xe^+) and the incident ion energies. Since the ions in the panel pixels have an energy distribution from several tens to a hundred and several tens of eV [20-22], the average sputtering yield (Y') for a given ion is expressed as [23]

$$Y' = \int_0^V Y(E)g(E)dE, \tag{3.7}$$

where $Y(E)$ is the sputtering yield as a function of an incident ion energy E, $g(E)$ is the normalized ion flux energy distribution with respect to the total ion flux, and V is the cathode fall potential, which is approximately equal to the voltage applied to the panel. If the mean free path for the symmetric charge transfer (l) is much shorter than the length of the cathode fall region (L), $g(E)$ can be expressed as [24]

$$g(E) = \frac{L}{2l}\frac{1}{V}\exp\left[-\left(\frac{L}{2l}\frac{E}{V}\right)\right]. \tag{3.8}$$

The mean free path l is obtained by $(N\sigma)^{-1}$ [23], where N is the discharge gas density and σ is the cross section of symmetric charge transfer between ions and their parent neutral atoms. The values of the σ are reported as 2.0×10^{-15} cm^2 for Ne-Ne^+ and 8.0×10^{-15} cm^2 for Xe-Xe^+ [21], thus the L/l values of Ne^+ and Xe^+ are 49.2 and 34.8 in the case of a Xe content in the discharge gas of 15% and a gas pressure of 450 Torr assuming L = 20 μm, respectively [23]. Figure 3.6 shows the estimated energy distributions for Ne^+ and Xe^+ fluxes arriving at the (Mg,Ca)O layer surface at the applied firing voltage of 360 V using Eq. (3.8). The energy distribution of the Ne^+ flux is less than that of the Xe^+ due to the greater probability of charge transfer collisions for Ne^+ [25]. Although the approximative values in Fig. 3.6 are somewhat different from the actual values especially at the high-energy region due to frequent charge

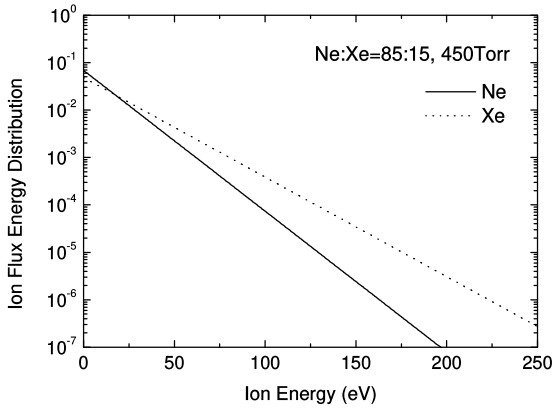

Figure 3.6: Estimated energy distributions for Ne^+ and Xe^+ fluxes arriving at the (Mg,Ca)O layer surface in the case of a Xe content in the discharge gas of 15% and a gas pressure of 450 Torr at the applied voltage of 360 V using Eq. (3.8).

exchange collisions, the effects are limited for the following calculations because of much low amounts of the ions with high energy [26].

The MgO and CaO sputtering yields for low-energy ion bombardment have experimentally been determined for various noble gas ions [27-29]. In these prior studies, the experimentally determined dependence of the sputtering yield on the normally incident ion energy ($Y(E)$) are fitted using the formula

$$Y(E) = a\left(1-\sqrt{\frac{E_0}{E}}\right)^{\frac{5}{2}}\left[1+b\left(\sqrt{\frac{E}{E_0}}-1\right)\right]. \tag{3.9}$$

In the case of Ne^+, a, b, and E_0 are 1.88, -0.148, and 66.7 eV for MgO, and 0.0284, 15, and 53.5 eV for CaO, respectively. In the case of Xe^+, a, b, and E_0 are 0.119, 8.96, and 58.4 eV for MgO, and 0.0781, 13.8, and 84.3 eV for CaO, respectively. MgO is sputtered to a greater extent

than CaO due to its lower molecular mass (i.e., 40.3 g/mol for MgO and 56.1 g/mol for CaO).

$Y(E)g(E)$ in Eq. (3.7) can be calculated from the $Y(E)$ data in Refs. [27,28] and the $g(E)$ values in Fig. 3.6. Figures 3.7(a) and 3.7(b) show the calculated $Y(E)g(E)$ of MgO and CaO for Ne^+ and Xe^+, respectively. It has wider distribution in Xe^+ than in Ne^+ due to larger amounts of high-energy Xe^+ as can be seen in Fig. 3.6, which indicates that Xe^+ has a greater effect on the sputtering yield of (Mg,Ca)O. The $Y(E)g(E)$ values for Ne^+ in present study are much lower than those in Ref. [23] even at the similar discharge gas conditions, which arises from the different sputtering yields applied to the calculations. The sputtering yields applied in this study have higher sputtering threshold energies and lower amounts in the low-energy region, where much more of the ion flux exist, resulting in the lower $Y(E)g(E)$ values in this work compared with those in Ref. [23].

The average sputtering yield per panel pixel ($Y'^{\,panel}$) can be expressed as

$$Y'^{\,panel} = Y'^{\,Ne^+} \frac{N_{Ne^+}}{N_{Ne^+} + N_{Xe^+}} + Y'^{\,Xe^+} \frac{N_{Xe^+}}{N_{Ne^+} + N_{Xe^+}}, \tag{3.10}$$

where $Y'^{\,Ne^+}$ and $Y'^{\,Xe^+}$ are the Y' values for Ne^+ and Xe^+ sputtering, respectively, and N_{Ne^+} and N_{Xe^+} are the quantities of Ne^+ and Xe^+ ions generated during discharge, respectively. The ion ratio during the discharge can be estimated by calculating the ionization coefficients for Ne and Xe using the Boltzmann equation solver (Bolsig+, Gerjan Hagelaar) [30]. Figure 3.8 plots the Xe^+ ratios during the discharge $[N_{Xe^+}/(N_{Ne^+} + N_{Xe^+})]$ at various Xe concentrations as a function of E/p, where E and p indicate the electric field intensity in a pixel and the pressure of the discharge gas, respectively. These plots demonstrate that the Xe^+ ratio increases when E/p decreases. The Xe^+ ratio can be estimated at 0.915 based on the values of Ne:Xe = 85:15 and E/p $\approx$ 100 V/cm/Torr in this study.

The results obtained using Eqs. (3.7) and (3.10) for MgO and CaO are summarized in Table 3.2. The Y_{MgO}/Y_{CaO} resulting from the data in Table 3.2 is 8.34, which is approximately 2 times

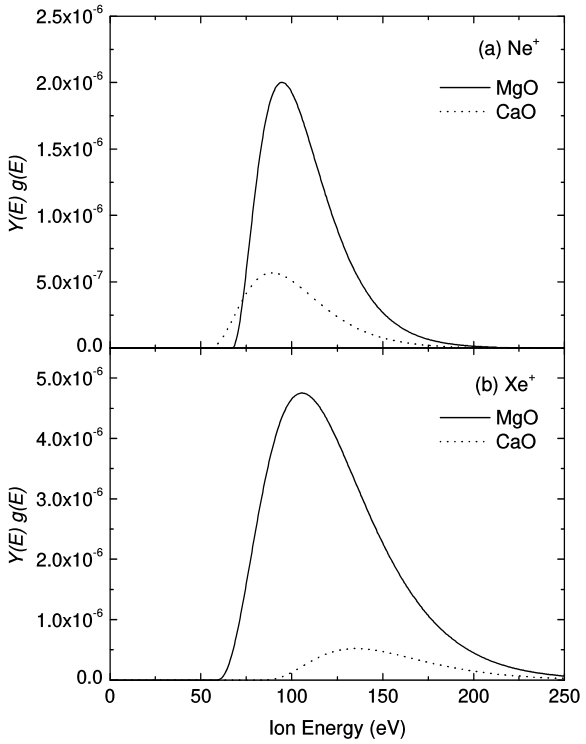

Figure 3.7: Calculated distribution of $Y(E)g(E)$ for MgO and CaO in conjunction with (a) Ne^+ and (b) Xe^+ sputtering.

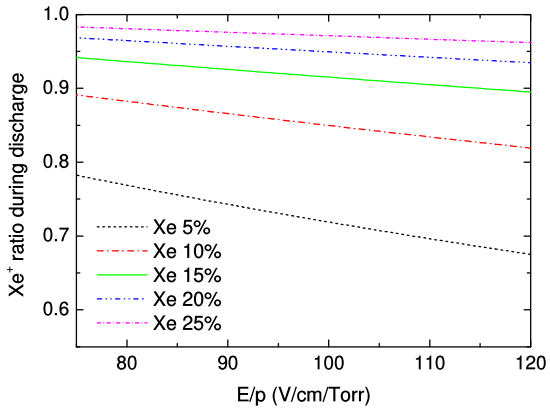

Figure 3.8: The Xe^+ ratios during the discharge $[N_{Xe^+}/(N_{Ne^+}+N_{Xe^+})]$ at various Xe concentrations as a function of E/p.

larger than the value obtained from Fig. 3.4. This difference is attributed to several effects. Firstly, the energetic ions in the pixels are predominantly distributed over the range of 10° to 30° with respect to the surface normal [31], while the ion incidence angle applied for the sputtering yield in this study is 0° with respect to the surface normal. This difference in the incidence angle may modify the sputtering yield [32]. Moreover, especially in the case of low-energy ion bombardment (during which numerous ion fluxes exist in the panel pixel), the sputtering yield is greatly modified by surface charging effects. Carbonation may also modify the MgO sputtering yield similar to the case of hydroxylation reported in Refs. [33,34]. This effect may be larger in CaO due to the high surface reactivity, leading to significant change in the CaO sputtering yield. Especially in (Mg,Ca)O, it has been demonstrated that carbonation species are predominantly adsorbed at Ca site, but not at Mg site as described in Chapter 2. However, it is

Table 3.2: Calculation results obtained using Eqs. (3.7) and (3.10) for MgO and CaO.

	Y'^{Ne^+}	Y'^{Xe^+}	Y'^{panel}
MgO	9.59×10^{-5}	3.55×10^{-4}	3.33×10^{-4}
CaO	3.11×10^{-5}	4.08×10^{-5}	4.00×10^{-5}

difficult to estimate these effects quantitatively because the amounts of the modification of the sputtering yield by ion bombardment with various incidence angles, by surface charging, and by carbonation have yet to be studied for MgO and CaO. Although the sputtering yield ratio from Table 3.2 is different from the estimated value in Fig. 3.4 because of these reasons, the good correlation between the experimental and calculated data upon setting Y_{MgO}/Y_{CaO} to 4.02 demonstrates that the increase in the CaO concentration is due to the preferential sputtering.

The effect of the Xe content on this preferential sputtering was assessed by determining Y_{MgO}/Y_{CaO} as a function of the Xe proportion in the Ne:Xe mixed discharge, based on Eq. (3.9). The estimated Xe^+ ratio during the discharge $[N_{Xe^+}/(N_{Ne^+} + N_{Xe^+})]$ at E/p = 100 V/cm/Torr and the normalized Y_{MgO}/Y_{CaO} value with respect to the maximum at an ion bombardment energy of 100 eV for both Ne^+ and Xe^+ are shown in Figs. 3.9(a) and 3.9(b), respectively. The Xe^+ ratio during the discharge reached $\sim$ 1 even at a 60% Xe content. A Xe^+ bombardment results in preferential MgO sputtering (relative to CaO sputtering) compared with Ne^+ because Xe^+ has a much heavier atomic mass (i.e., 20.2 g/mol for Ne and 131.3 g/mol for Xe). Therefore, Y_{MgO}/Y_{CaO} increases along with the Xe content but plateaus above 60% Xe.

As noted in Chapter 1, higher Xe levels increase the VUV output in plasma discharge devices, but also increase the discharge voltage [35-37]. Thus, high-γ materials such as (Mg,Ca)O have been studied as protective layers to suppress the increases in the discharge voltage [1-

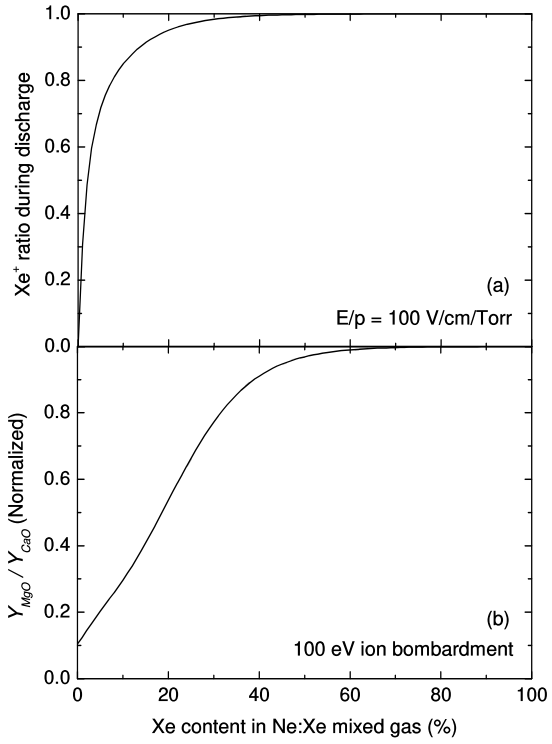

Figure 3.9: Estimated Xe^+ ratio during the discharge $[N_{Xe^+}/(N_{Ne^+}+N_{Xe^+})]$ as a function of the Xe content in the Ne:Xe mixed gas at E/p = 100 V/cm/Torr. (b) Normalized Y_{MgO}/Y_{CaO} values with respect to the maximum as a function of the Xe content in the Ne:Xe mixed gas at an ion bombardment energy of 100 eV for both Ne^+ and Xe^+ with normal incidence, using a formula and parameters described in Refs. [27,28].

3,13,38]. However, considering the above results, it is apparent that higher Xe levels modify the aging characteristics of panels with (Mg,Ca)O protective layers based on preferential sputtering. Preferential sputtering also appears for other complex oxide protective layers with high γ, including (Mg,Sr)O [38-41], (Mg,Ca,Sr)O [4,40], (Mg,Ba)O [38,42], and (Sr,Ca)O [5-7], whose sputtering yields and γ for each single metal oxide are clearly different. The degradation of the discharge intensity due to the shrinkage of the discharge area proceeds primarily as a consequence of the preferential sputtering during prolonged aging, even if the initial properties of the panels with complex metal oxide protective layers are improved by a high Xe content in the discharge gas. This is considered to be a critical point for the practical applications of complex oxide protective layers having high γ.

The practical application of complex oxide protective layers will require improved pixel structures to suppress the shrinkage of the discharge area. Thus, the discharge area modification upon prolonged aging was investigated while varying the initial discharge area. The initial discharge area depends on the geometry of the bus electrodes [43-45], ε_d or d_d [43,46,47], and so panels with various ε_d, d_d, and pixel sizes were fabricated and aged for 2500 h. Figures 3.10(a) and 3.10(b) show digital optical microscope images of the discharge traces of the protective layers for panels with dielectric layers having ε_d and d_d values of 11.3 and 39 μm, and 5.9 and 24 μm, respectively. The firing discharge voltage evidently increases by decreasing ε_d or increasing d_d [46]. When ε_d was changed from 11.3 to 5.9, d_d was adjusted to keep the equivalent firing voltage. Thus, the results shown in Fig. 3.10 were obtained under almost the same E/p. In Fig. 3.10, it is evident that wider regions were sputtered and the maximum sputtered depth decreased with decreasing ε_d and d_d. Simulations of the excited states of Xe and the dimer Xe_2^* have shown similar results. The full width at half maximum of the photon flux region becomes much wider upon decreasing ε_d while the region becomes narrower upon

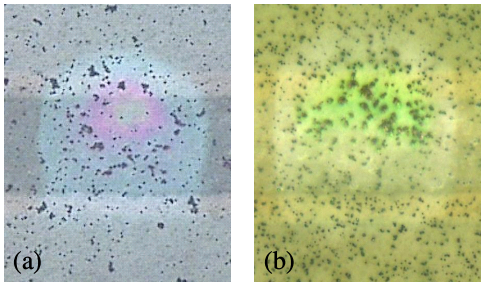

Figure 3.10: Optical microscope images of the discharge traces for panels with different dielectric layers under the (Mg,Ca)O protective layers after 2500 h aging. The permittivity and thickness of the dielectric layers are (a) 11.3 and 39 μm, and (b) 5.9 and 24 μm, respectively.

decreasing d_d [43]. The results shown in Fig. 3.10 demonstrate that the discharge area can be controlled by changing the dielectric layer.

The modification of the discharge area after 2500 h aging was assessed while adjusting the initial discharge area with various dielectric layers and pixel sizes. The results are shown in Fig. 3.11. The data above the dotted line demonstrate that the discharge area after aging is wider than the initial discharge area. Below the threshold value of the initial discharge area ($\sim$ 450 in this study), the discharge area after aging is decreased. In contrast, the discharge area after aging is increased above the threshold value. The shrinkage and expansion of the discharge area depending on the size of the initial discharge area are explained below.

Figure 3.12 presents a schematic of the initial discharge and γ distributions in a panel pixel after aging, for various ε_d and d_d values. In the case of ε_d = 11.3 and d_d = 39 μm, the initial discharge area becomes narrow. This leads to localized sputtering of the protective layer, thus increasing the CaO concentration and γ due to preferential sputtering. The edge regions exhibit

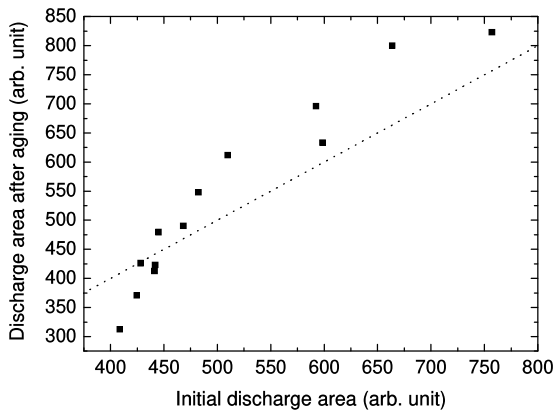

Figure 3.11: Relationship between the initial discharge area and the discharge area after 2500 h aging for panels with (Mg,Ca)O protective layers. The data above the dotted line show that the discharge area after aging is wider than the initial discharge area.

almost no sputtering, and so the difference in γ values between the edge and the center region becomes high, resulting in shrinkage of the discharge area. In contrast, if ε_d is reduced, the initial discharge area is widened. Not only the center regions but also the edge regions are sputtered by the wider discharge to generate higher γ, thus expanding the discharge area. Therefore, the initial discharge area must be sufficiently wide in order to suppress the shrinkage of the discharge area within the (Mg,Ca)O protective layer.

Finally, the effects of an initial discharge area on the panel luminous efficiency were investigated, which is determined by ε_d and d_d values. Figure 3.13 plots the luminous efficiencies (normalized with respect to the initial efficiencies) as a function of the aging time for ε_d and d_d values of 11.3 and 39 μm, and 5.9 and 24 μm. The solid and dotted lines correspond to fitting curves generated using exponential decay functions. The efficiency degradation is clearly

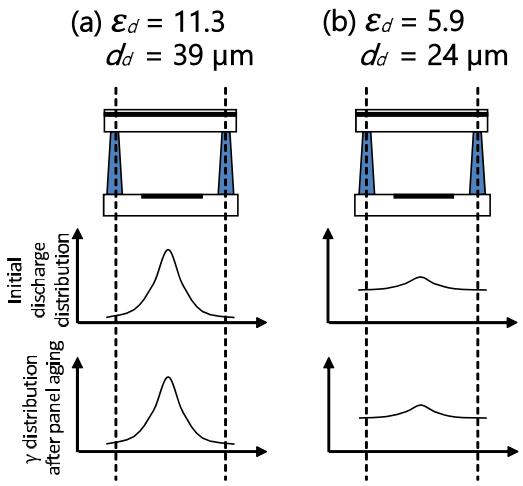

Figure 3.12: Schematic of the discharge and γ distributions in a panel pixel in the cases of (a) $\varepsilon_d = 11.3$, $d_d = 39$ μm and (b) $\varepsilon_d = 5.9$, $d_d = 24$ μm.

slowed down in smaller ε_d. The degradation of the panel luminous efficiency during aging is caused due to the deterioration of phosphors [8-10] and protective layers [11,12] by VUV or discharge irradiation, and the decreased phosphor excitation efficiency by prolonged aging (as described in Chapters 4 and 5 in detail). However, present work indicates that efficiency loss also arises from a contraction of the discharge area due to preferential sputtering of the protective layer, and can be suppressed by adjusting the initial discharge area due to the modification of ε_d and d_d values of the dielectric layer.

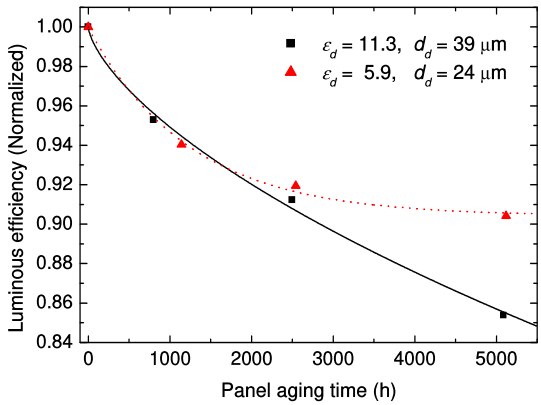

Figure 3.13: Normalized panel luminous efficiencies for ε_d and d_d values of 11.3 and 39 μm (squares), and 5.9 and 24 μm (triangles). Solid and dotted lines indicate fitting curves generated using exponential decay functions.

3.4 Conclusions

The discharge modification of panels with (Mg,Ca)O protective layers after prolonged aging was investigated. After aging, shrinkage of the discharge area was observed, and the CaO concentration increased in the sputtered regions on the (Mg,Ca)O protective layer. A comparison between the experimental and calculated data indicated that the CaO concentration increased due to the preferential sputtering of MgO in the protective layer in response to low-energy ion bombardment. Therefore, it is proposed that the reduced discharge arises from variations in the γ distribution in the panel pixels due to the change in the CaO concentration. This preferential sputtering is enhanced by a higher Xe content in the discharge gas and by a smaller E/p value. The discharge modification during prolonged aging due to variations in the initial discharge

area was also evaluated, which can be controlled by adjusting the characteristics of the dielectric layer under the protective layer. Reducing ε_d was found to expand the discharge area, thus suppressing degradation of the panel luminous efficiency.

References

[1] T.-H. Lee, H.-W. Cheong, O. Kwon, K.-W. Whang, Application of MgCaO Cathode Layer to Plasma Display Panel for High Luminous Efficacy, IEEE Trans. Electron Devices 60 (2013) 301-304.

[2] Q. Yan, K. Kotera, H. Zhao, H. Liu, H. Zhou, Y. Tang, X. Deng, Calcium Magnesium Oxide Nano-crystal (Nano-CMO) for Improving Uniformity of High Xe Content PDP, SID Int. Symp. Dig. Tech. Pap. 45 (2014) 208-211.

[3] C.-S. Park, E. Y. Jung, H.-S. Tae, Improvement of luminous efficiency using Li-doped MgO layer coated by MgCaO crystal powders in plasma display panels, Mol. Cryst. Liq. Cryst. 645 (2017) 130-137.

[4] R. Kim, Y. Kim, J. Cho, J.-W. Parka, Luminous efficiency and secondary electron emission characteristics of alternating current plasma display panels with MgO-SrO-CaO protective layers, J. Vac. Sci. Technol. A 18 (2000) 2493-2496.

[5] G. Uchida, S. Uchida, T. Akiyama, H. Kajiyama, T. Shinoda, Effect of high Xe-concentration in a plasma display panel with a SrCaO cold cathode, J. Appl. Phys. 107 (2010) 103311-1-7.

[6] T. Yano K. Uchida, G. Uchida, T. Shinoda, H. Kajiyama, Discharge Characteristics of PDPs with the Ternary Oxides Protective Layers Manufactured by Using All-In-Vacuum Process, SID Int. Symp. Dig. Tech. Pap. 41 (2010) 739-741.

[7] D. Zhu, L. Song, X. Zhang, H. Kajiyama, Vacuum ultra-violet emission of plasma discharges with high Xe partial pressure using a cathode protective layer with high secondary electron emission, J. Appl. Phys. 115 (2014) 063302-1-7.

[8] C. H. Ha, B. Y. Han, J. S. Yoo, H. S. Bae, K.-W. Whang, Characteristics of Phosphor Degradation in AC-Driven Plasma Display Panels, J. Electrochem. Soc. 155 (2008) J230-J234.

[9] K. Sawada, S. Adachi, Unique photoluminescence degradation/recovery phenomena in trivalent ion-activated phosphors, J. Appl. Phys. 118 (2015) 103106-1-7.

[10] L. Amidani, K. Korthout, J. J. Joos, M. van der Linden, H. F. Sijbom, A. Meijerink, D. Poelman, P. F. Smet, P. Glatzel, Oxidation and Luminescence Quenching of Europium in $BaMgAl_{10}O_{17}$ Blue Phosphors, Chem. Mater. 29 (2017) 10122-10129.

[11] H. K. Yu, W.-K. Kim, J.-L. Lee, E. C. Park, J. S. Kim, J. H. Ryu, Degradation Mechanism of Secondary Electron Emission in Plasma-Exposed MgO Films, Jpn. J. Appl. Phys. 48 (2009) 076003-1-4.

[12] C.-S. Park, H.-S. Tae, E.-Y. Jung, J. H. Seo, B. J, Shin, Influence of Ion Bombardment on Electron Emission of MgO Surface in AC Plasma Display Panel, IEEE Trans. Plasma Sci. 38 (2010) 2439-2444.

[13] T. Zukawa, K. Yoshino, Y. Oe, H. Kawarazaki, K. Aoto, Y. Tanaka, R. Murai, Development of MgCaO Protective Layer of Plasma Display Panels for Decreased Discharge Voltage, SID Int. Symp. Dig. Tech. Pap. 43 (2012) 165-167.

[14] M. Amatsuchi, A. Hirota, H. Lin, T. Naoi, E. Otani, H. Taniguchi, K. Amemiya, Discharge Time Lag Shortening by Using a New Material Layer in AC PDP, Proc. 12th Int. Disp. Workshops 1 (2005) 435-438.

[15] P. E. Larson, M. A. Kelly, Surface charge neutralization of insulating samples in x-ray photoemission spectroscopy, J. Vac. Sci. Technol. A 16 (1998) 3483-3489.

[16] D. A. Shirley, High-Resolution X-Ray Photoemission Spectrum of the Valence Bands of Gold, Phys. Rev. B 5 (1972) 4709-4714.

[17] E. Leyssenne, N. Sewraj, N. Merbahi, F. Marchal, M. C. Bordage, Visible and near infrared optical emission spectroscopic analysis of a pure xenon mono-filamentary dielectric barrier discharge, Proc. 31st Int. Conf. Phenom. Ionized Gases (2013).

[18] Y. Motoyama, D. Kato, N. Saito, M. Seki, Carbonation reaction of (Ca, Mg)O protective layer on plasma display panel, J. Soc. Inf. Disp. 21 (2013) 41-45.

[19] A. Galdikas, L. Praniavichius, Interactions of Ions with Condensed Matter, Horizons in World Physics Vol. 229, Nova Science Publishers, Inc., New York, 2000, pp. 37-60.

[20] Y. K. Shin, J. K. Lee, C. H. Shon, W. Kim, Ion Energy Distribution in Alternating-Current Plasma Display Panel Cell, Jpn. J. Appl. Phys. 38 (1999) L174-L177.

[21] G. J. M. Hagelaar, G. M. W. Kroesen, M. H. Klein, Energy distribution of ions and fast neutrals in microdischarges for display technology, J. Appl. Phys. 88 (2000) 2240-2245.

[22] L. C. Pitchford, J. Wang, D. Piscitelli, J. P. Boeuf. Ion and Neutral Energy Distributions to the MgO Surface and Sputtering Rates in Plasma Display Panel Cells, IEEE Trans. Plasma Sci. 34 (2006) 351-359.

[23] S. J. Yoon, I. Lee, Theory of the lifetime of the MgO protecting layer in ac plasma display panels, J. Appl. Phys. 91 (2002) 2487-2492.

[24] W. D. Davis, T. A. Vanderslice, Ion Energies at the Cathode of a Glow Discharge, Phys. Rev. 131 (1963) 219-228.

[25] D. Piscitelli, A. V. Phelps, J. de Urquijo, E. Basurto, L. C. Pitchford, Ion mobilities in Xe/Ne and other rare-gas mixtures, Phys. Rev. E 68 (2003) 046408-1-10.

[26] K. Yoshino, K. Nomoto, M. Goto, R. Murai, T. Tsujita, M. Terauchi, Y. Morita, M. Nishitani, M. Kitagawa, Effects of Ne/Xe Gas Mixture Ratio on Sputtering Rate of MgO Protective Layer, Proc. 18th Int. Disp. Workshops 2 (2011) 689-692.

[27] K. Hine, S. Yoshimura, K. Ikuse, M. Kiuchi, J. Hashimoto, M. Terauchi, M. Nishitani, S. Hamaguchi, Experimental evaluation of MgO sputtering yields by monochromatic Ne, Kr, or Xe ion beams, Thin Solid Films 517 (2008) 835-840.

[28] S. Yoshimura, K. Hine, M. Kiuchi, J. Hashimoto, M. Terauchi, Y. Honda, M. Nishitani, S. Hamaguchi, Experimental evaluation of CaO, SrO and BaO sputtering yields by Ne^+ or Xe^+ ions, J. Phys. D: Appl. Phys. 44 (2011) 255203-1-5.

[29] S. Yoshimura, K. Hine, M. Kiuchi, J. Hashimoto, M. Terauchi, Y. Honda, M. Nishitani, S. Hamaguchi, Sputtering Yields of CaO, SrO, and BaO by Monochromatic Noble Gas Ion Bombardment, Jpn. J. Appl. Phys. 51 (2012) 08HB02-1-4.

[30] https://www.bolsig.laplace.univ-tlse.fr/

[31] S. S. Yang, J. K. Lee, S. W. Ko, H. C. Kim, J. W. Shon, Two-Dimensional Kinetic and Three-Dimensional Fluid-Radiation Transport Simulations of Plasma Display Panel, Contrib. Plasma Phys. 44 (2004) 536-541.

[32] Q. Wei, K.-D. Li, J. Lian, L. Wang, Angular dependence of sputtering yield of amorphous and polycrystalline materials, J. Phys. D: Appl. Phys. 41 (2008) 172002-1-4.

[33] K. Ikuse, S. Yoshimura, M. Kiuchi, M. Terauchi, M. Nishitani, S. Hamaguchi, Sputtering

yields of magnesium hydroxide [$Mg(OH)_2$] by noble-gas ion bombardment, J. Phys. D: Appl. Phys. 45 (2012) 432001-1-5.

[34] M. El Marsi, R. Moultif, S. Lahlou, S. Rochd, A. Dezairi, Monte Carlo simulations of MgO and $Mg(OH)_2$ thin films sputtering yields by noble-gas ion bombardment in plasma display panel PDP, Nucl. Inst. Methods Phys. Res. B 430 (2018) 72-78.

[35] J. Meunier, Ph. Belenguer, J. P. Boeuf, Numerical model of an ac plasma display panel cell in neon-xenon mixtures, J. Appl. Phys. 78 (1995) 731-745.

[36] G. Oversluizen, T. Dekker, M. F. Gillies, S. T. de Zwart, High-Xe-content high-efficacy PDPs, J. Soc. Inf. Disp. 12 (2004) 51-55.

[37] Z. Liu, W.-B. Hu, C.-L. Liu, Luminance and Luminous Efficacy Improvement of Mercury-Free Flat Fluorescent Lamp With Arclike Electrode, IEEE Trans. Plasma Sci. 38 (2010) 2860-2866.

[38] J. W. Lee, Calculation of the Secondary Electron Emission Coefficients of MgO, MgBeO, MgCaO, MgSrO and MgBaO Induced by Auger Neutralization of He^+, Ne^+, Ar^+ and Xe^+ Ions, New Phys.: Sae Mulli 68 (2018) 939-944.

[39] T. Shinoda, H. Uchiike, S. Andoh, Low-Voltage Operated AC Plasma-Display Panels, IEEE Trans. Electron Devices 26 (1979) 1163-1167.

[40] S.-K. Kwon, S.-S. Yang, J.-H. Kim, B.-H. Ha, C.-H. Bae, J.-W. Seo, J.-W. Woo, J.-S. Ahn, Y.-L. Cho, Y.-K. Jung, S.-G. Choi, High Luminous Efficacy and Low Power Consumption Plasma TV, SID Int. Symp. Dig. Tech. Pap. 42 (2011) 741-744.

[41] K. A. Lee, B. K. Min, Y. S. Byeon, J. H. Choi, R. J. Jung, H. S. Uhm, E. H. Choi, Measurement of Energy Band Structure of MgO, MgSrO and MgCaO Thin Film by their

Secondary Electron Emission Coefficient due to Auger Neutralization, J. Phys.: Conf. Ser. 417 (2013) 012009-1-11.

[42] H. K. Yu, W.-K. Kim, J.-L. Lee, J. S. Kim, J. H. Ryu, The Effect of Doping to MgO Protection Layer on Secondary Electron Emission Property, SID Int. Symp. Dig. Tech. Pap. 37 (2006) 544-546.

[43] S. Rauf, M. J. Kushner, Dynamics of a coplanar-electrode plasma display panel. II. Cell optimization, J. Appl. Phys. 85 (1999) 3470-3476.

[44] K. C. Choi, N. H. Shin, K. S. Lee, B. J. Shin, S.-E. Lee, Study of Various Coplanar Gaps Discharges in ac Plasma Display Panel, IEEE Trans. Plasma Sci. 34 (2006) 385-389.

[45] S. Hori, T. Murakoso, E. Otani, K. Amemiya, R. Murai, Improvement of Luminous Efficiency Using New Structure in AC-PDPs, SID Int. Symp. Dig. Tech. Pap. 42 (2011) 745-747.

[46] S. B. Shim, S.-Y. Cho, D. K. Lee, I. C. Song, C. H. Park, H.-J. Lee, H. J. Lee, The effects of permittivity and thickness of dielectric layers on micro dielectric barrier discharges, Thin Solid Films 518 (2010) 3037-3041.

[47] P. Zhang, Y. Tu, L. Yang, Simulation studies of the dielectric layer effect on the discharge characteristics of the shadow mask plasma display panel, J. Vac. Sci. Technol. B 29 (2011) 04E105-1-5.

Chapter 4

Degradation of phosphor excitation efficiency by adsorption of organic compounds on phosphors by VUV irradiation

In this chapter, the mechanism for the degradation of a phosphor excitation efficiency in flat panel plasma discharge devices was investigated. It is found that remaining organic compounds contained in the binders of phosphors were transformed to VUV absorbing substances by prolonged aging, which reduces the excitation efficiency of a phosphor, especially in the shorter wavelength VUV range. Organic residues are shown to degrade not only the discharge voltage but also the phosphor excitation efficiency by prolonged aging. Appropriate annealing of the panels is required to suppress these degradation phenomena for a (Mg,Ca)O protective layer because of high reactive property for organic compounds.

4.1 Introduction

In this chapter, the effects of internal residual impurities on the characteristics of flat panel plasma discharge devices are investigated. The modification of panel characteristics by residual gases such as H_2O, CO_2 [1,2], O_2 [3], H_2 [4,5], and N_2 [6,7] have widely been studied. However, there have been few reports scrutinizing the effects of residual organic compounds in spite of the fact that many organic compounds can also remain in the panel as a result of insufficient decomposition or oxidation of organic binder or solvent during the annealing process in production [8]. In order to reduce the effects of the residual gas, introducing getters in the panel is proposed [9,10]. However, this approach is hard to be applied owing to forming unstable discharge due to desorption of gettered gas by thermal effects and ion sputtering during operation. A sealing process in vacuum is also proposed to decrease the residual impurities [11,12], but the practical applications are not realized owing to the high process cost and the small throughput. Therefore, it is very helpful to investigate the quantitative effects of the residual organic compounds in order to control the characteristics modification of plasma discharge devices because a (Mg,Ca)O protective layer has a larger potential of adsorption of impurity gas than a conventional MgO layer [13-15].

As described in Chapter 2, the author first demonstrated the modification of the chemical state at the surface of a (Mg,Ca)O protective layer by organic gas. The modified chemical state results in the larger ionization potential and then the degraded discharge voltage. In present work, the effect on the luminous efficiency is investigated by measuring the photoluminescence (PL) from the samples with organic contaminants on the phosphors. VUV radiation can be absorbed by the contaminants to a significant extent. Thus, the absorption of VUV light by organic contaminants can be a factor in luminous degradation due to a decreased phosphor excitation efficiency.

Table 4.1: Specifications of the test back panels used in this study.

Back Panel	
Address electrode width	80 μm
Dielectric layer thickness	10 μm
Barrier rib height	120 μm
Barrier rib width	50 μm
Phosphor thickness	10 μm
Pixel size	675×300 μm^2

The purpose of present work is to demonstrate the modification of luminance by the residual organic compounds. PDPs are employed to assess the panel characteristics as model flat panel plasma discharge devices. It is found that loss of luminance due to organic residues occurs as a result of the absorbance of VUV radiation by prolonged VUV irradiation. The results suggest that the consequent formation of byproducts reduces a phosphor excitation efficiency by absorbing the shorter wavelength VUV light.

4.2 Experimental Methods

The luminous degradation of plasma discharge devices by organic compounds was assessed using the back panels for 42-inch high-definition (HD) AC PDPs. (Y,Gd)BO_3:Eu^{3+} (YGB), a mixture of YBO_3:Tb^{3+} (YBT) and Zn_2SiO_4:Mn^{2+} (ZSM), and $BaMgAl_{10}O_{17}$:Eu^{2+} (BAM) were employed as red, green, and blue phosphors on the back panel, respectively. The specifications of the test back panels used in this study are shown in Table 4.1. The panels were then cut into the pieces at the size of a few cm^2 for the following measurements.

PL measurements in the visible range were carried out by irradiating the back panel samples

with VUV light in a vacuum chamber. The pressure in the chamber was approximately 1×10^{-2} Torr and the VUV radiation was provided by the 147 nm line of a Xe excimer lamp (SUS07, USHIO) and the 173 nm line of a Kr excimer lamp (SUS03, USHIO) attached to the chamber. The intensity of the excitation light was adjusted by irradiating $CaCO_3$ powder as a stable reference and monitoring the reflection intensity of the near infrared light emitted from the lamps. The PL spectra of various samples were acquired using a grating monochromator together with a photodiode array coupled to the chamber via an optical fiber. The spectral response of the detection system was calibrated with a standard W lamp reference spectrum.

The amounts of organic residues adsorbed on the samples were determined by thermal desorption spectrometry (TDS; TDS1200, ESCO). Residual gases in the measurement chamber were removed by heating the chamber prior to each measurement. The base pressure prior to each trial was $\sim 1.5 \times 10^{-9}$ Torr and the sample surface temperature was increased at a rate of 10.5 °C/min. The mass of thermally desorbed molecules was identified with a quadrupole mass spectrometer.

4.3 Results and Discussion

Figure 4.1 shows the PL spectra of the back panel sample in response to 147 and 173 nm VUV excitation. The red phosphors generate peaks at 593, 612, and 627 nm, due to $^5D_0 \rightarrow {}^7F_1$ and $^5D_0 \rightarrow {}^7F_2$ transitions of Eu^{3+} [16]. In the case of the green phosphor, 527 and 543 nm peaks are observed, corresponding to $^4T_{1s} \rightarrow {}^6A_{1g}$ transition of Mn^{2+} and $^5D_4 \rightarrow {}^7F_5$ transition of Tb^{3+}, respectively [17]. The 450 nm peak produced by the blue phosphor is caused by the transition from $4f^6 5d^1$ excited state to the $4f^7$ ground state of Eu^{2+} [16].

Here, the effect of organic residues on the luminous intensity modification of the phosphors is now considered. The deposition of organic compounds were simulated by exposing the back

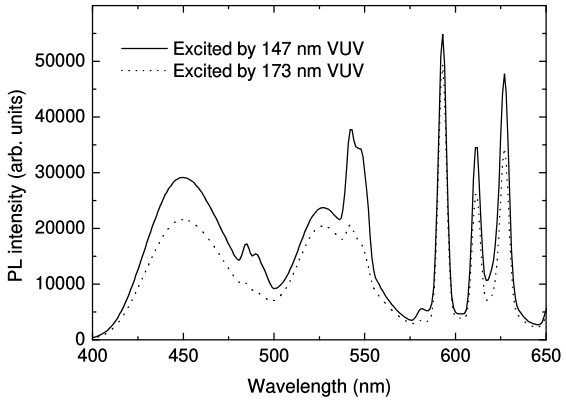

Figure 4.1: PL spectra acquired from the back panel. The solid and dotted lines correspond to excitation by 147 and 173 nm VUV, respectively.

panels to an atmosphere containing α-terpineol (TP) vapor for 0.5 or 2 h after annealing in air at 470°C (see Fig. 4.2). TP is often used as an organic solvent for the phosphor paste binder, and so can be present as an organic residue in the panels. The structural formula of TP is shown in Fig. 4.3. These test specimens were irradiated with 147 nm VUV light in a vacuum chamber after the exposure to the TP vapor.

Figures 4.4(a)-4.4(c) summarize the normalized PL intensities at 593, 543, and 450 nm with respect to the initial intensities for the TP-contaminated samples over time in response to continuous irradiation by 147 nm VUV, respectively. The PL intensities of the non-exposed and 0.5 h-exposed samples initially decrease but then recover during 6 h of VUV irradiation. However, the luminous intensity of the sample exposed for 2 h continually drops, especially at 593 nm. These results suggest that the luminous degradation was not caused by phosphor damages but

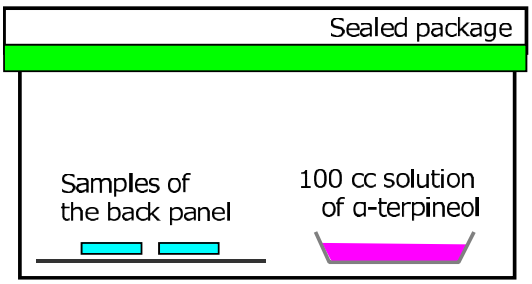

Figure 4.2: Schematic of the apparatus used to expose the back panel samples to α-terpineol vapor.

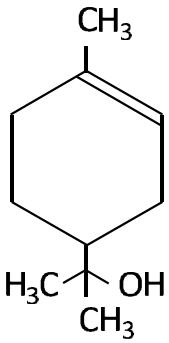

Figure 4.3: The molecular structure of α-terpineol.

by organic residues which were modified due to the 147 nm VUV radiation. It should be noted that these experiments were carried out in a vacuum chamber, not in a discharge gas atmosphere as found in a plasma discharge device. The luminance recovery described above is therefore attributed to desorption of the organic residues in the vacuum environment, meaning that luminous degradation could occur in an actual panel even in the case of a small amount of organic residues.

The effects of the organic residues on luminous intensity were assessed by following variations in the intensity in response to 147 and 173 nm excitation for the untreated sample and the sample exposed to the TP vapor for 2 h and to 147 nm VUV irradiation for 6 h, as in Fig. 4.5. There is obvious degradation of the luminous intensity in the red wavelength region compared with the green and blue regions in the case of 147 nm excitation. In contrast, 173 nm excitation results in minimal loss of luminance over the entire wavelength range. These results demonstrate that the drop in red luminous intensity solely by 147 nm excitation is not caused by phosphor damages but is rather due to reduction of 147 nm excitation. This could occur because of the formation of materials absorbing at 147 nm during VUV irradiation to the organic residues.

The VUV irradiation to hydrocarbons tends to generate high molecular weight compounds. As an example, in the case of CH_4, the reaction $n\mathrm{CH_4} + h\nu \rightarrow \mathrm{C}_n\mathrm{H}_{(2n+2)} + (n-1)\mathrm{H_2}$ occurs [18]. This transformation has been shown to increase the absorption of VUV light at shorter wavelengths [19]. Thus, similar reactions are believed to have occurred on the TP-contaminated phosphors used in this study. That is, the TP was transformed to higher molecular weight byproducts during 147 nm VUV irradiation and so the transmittance in the shorter wavelength region decreased. This process in turn degraded the luminous intensity of the phosphors due to a decreased excitation efficiency by the 147 nm VUV light.

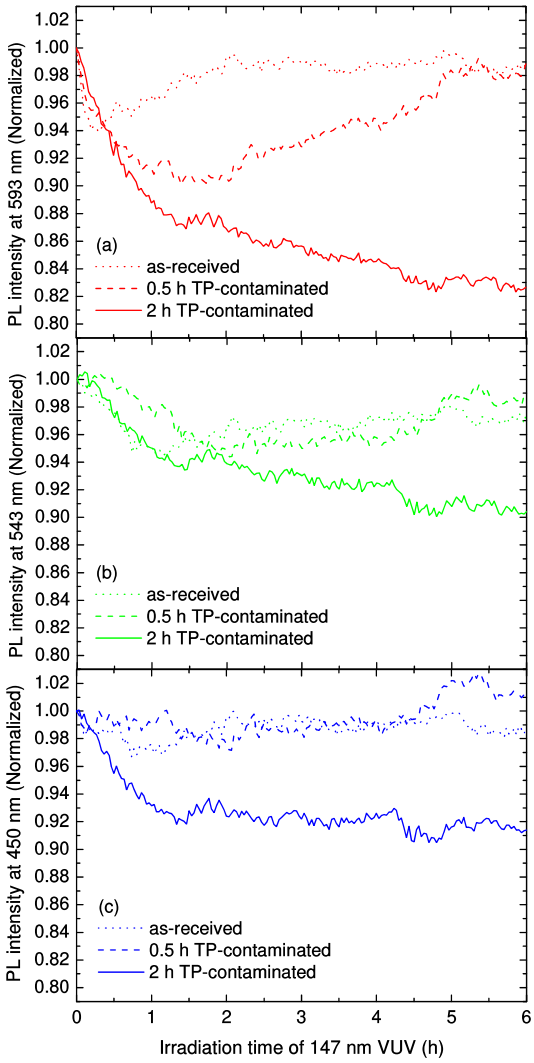

Figure 4.4: Normalized PL intensities at (a) 593, (b) 543, and (c) 450 nm with respect to the initial intensities during continuous irradiation by 147 nm VUV light. Dotted lines correspond to data for as-received samples, while dashed and solid lines indicate data for 0.5 and 2 h TP-contaminated samples, respectively.

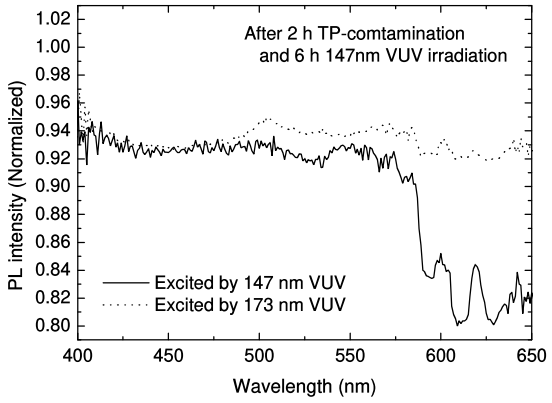

Figure 4.5: Variations in PL intensities after 2 h exposure to TP and 6 h irradiation with 147 nm VUV light. The solid line corresponds to data for 147 nm VUV excitation, while the dotted line indicates data for 173 nm VUV excitation.

Figure 4.6 presents TDS curves acquired from samples of the red, green, and blue phosphors annealed in air after the exposure to the TP vapor. During TDS, the loss of fragments of the organic deposits, including $^{16}CH_4$ (m/z = 16), $^{28}C_2H_4$ (m/z = 28), and $^{44}C_3H_8$ (m/z = 44), could be detected. However, since the peaks for these fragments overlap with those generated by H_2O and CO_2 (^{16}O, ^{28}CO, and $^{44}CO_2$), it is difficult to use these peaks to make a conclusive evaluation. Thus, the fragment at m/z =15 ($^{15}CH_3$) was employed, even though its intensity was relatively weak. It is evident that there was a greater release of organic residues from the red phosphors, indicating that more organic compounds were deposited on these sites. To determine the potential of the physical adsorption on each phosphor, the specific surface area was analyzed using the Brunauer-Emmett-Teller (BET) method, giving values of 2.2, 1.2, 1.4,

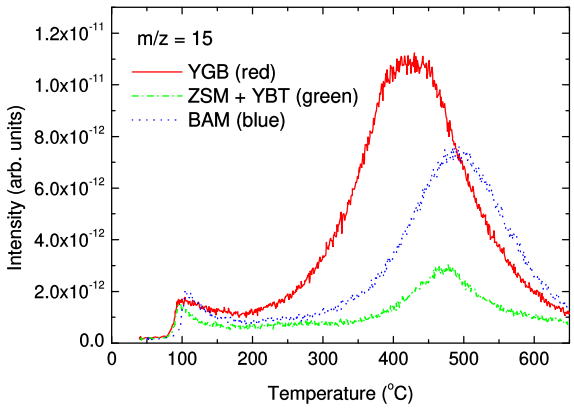

Figure 4.6: TDS curves at m/z = 15 for air-annealed samples of the red, green, and blue phosphors.

and 1.7 m^2/g for the YGB, YBT, ZSM, and BAM phosphors, respectively. These surface areas are well correlated with the amounts of organic desorption seen in Fig. 4.6. Consequently, the red phosphors are considered to have the largest amount of organic residues because of the widest surface area compared with other phosphors, resulting in reduced 147 nm excitation due to reaction of the organic residues on the red phosphors in response to continuous VUV irradiation.

Residual organic compounds are provided from not only phosphor binders at the back panel but also glass pastes of the dielectric layer at the front panel and glass frits for panel sealing [8]. An oxide protective layer can act as a getter of these organic residues during degassing process and the gettering amounts are more enhanced for a (Mg,Ca)O layer than for a conventional MgO layer because the chemical reactivity of CaO is larger than that of MgO even for

organic compounds [20,21]. The gettered species are desorbed by ion sputtering during discharge, resulting in the more residual impurities in the panel. This means that the degradation of a phosphor excitation efficiency by prolonged aging proceeds more readily for a (Mg,Ca)O protective layer than for a MgO protective layer. Therefore, it is necessary to assess the amount of organic residues in the panel during production and remove all impurities by appropriate annealing processes in order to introduce a (Mg,Ca)O protective layer.

4.4 Conclusions

The mechanism for the degradation of a phosphor excitation efficiency in plasma discharge devices by 147 nm VUV radiation was investigated. It is demonstrated that the luminance of the devices was degraded by prolonged VUV irradiation because of the presence of organic residues adsorbed on the phosphors. The obtained results suggest that the organic compounds were converted to substances which absorb VUV light in the shorter wavelength range. According to the results in Chapters 2 and 4, it is first demonstrated that not only the discharge voltage but also the phosphor excitation efficiency are degraded by organic residues in the panel by prolonged aging. A (Mg,Ca)O protective layer can promote the degradation owing to large adsorption of organic compounds. Sufficient annealing to remove the organic impurities is required for realization of high efficient plasma discharge devices with (Mg,Ca)O protective layers.

References

[1] W. E. Ahearn, O. Sahni, Effect of Reactive Gas Dopants on the MgO Surface in AC Plasma Display Panels, IBM J. Res. Dev. 22 (1978) 622-625.

[2] K. Yoshino, Y. Morita, T. Nagatomi, M. Terauchi, T. Tsujita, Y. Doi, T. Nakayama, Y. Yamauchi, M. Nishitani, M. Kitagawa, Y. Yamauchi, Y. Takai, Changes in ionization potentials of MgO and CaO films upon heating in air and vacuum investigated by metastable de-excitation spectroscopy, Appl. Surf. Sci. 259 (2012) 135-141.

[3] Y. Kamiya, Y. Hirano, O. Akinori, K. Ishii, Y. Murakami, H. Hiramoto, Influence of Gas Impurities on the Discharge Characteristics of an AC PDP, Proc. 16th Int. Disp. Workshops 2 (2009) 919-922.

[4] T. Okada, T. Komaki, Influence of H_2 Addition to Xe-Ne Gas Mixtures for the Voltage Lowering of AC Plasma Display Panels, SID Int. Symp. Dig. Tech. Pap. 36 (2005) 1245-1247.

[5] Wei, S. Jian, G. Eingang, The influence of H_2 addition on the discharge characteristics of Ne-Xe in color alternate current plasma display panel, EPJ Appl. Phys. 37 (2007) 331-334.

[6] D.-K. Lee, Y.-M. Jang, H.-D. Park, H.-J. Kim, J.-H. Lee, W.-Y. Choi, C.-S. Park, S.-B. Yoo, H. J. Lee, H.-J. Lee, The effect of N_2 gas mixture ratio on discharge characteristics of an AC PDP cell, SID Conf. Rec. Int. Disp. Res. Conf. 2005 (2005) 279-282.

[7] A. Oda, Y. Hirano, K. Ishii, Computational study on influence of N_2 addition on discharge characteristics of AC PDPs in Xe/Ne gas mixture, Proc. 20th Int. Disp. Workshops 1 (2013) 673-676.

[8] M. Uchidoi, Critical Aspects of the Plasma Display Panel Manufacturing Process, IEEE Trans. Plasma Sci. 34 (2006) 287-293.

[9] R. M. Caloi, C. Carretti, Getters and gettering in plasma display panels, J. Vac. Sci. Technol. A 16 (1998) 1991-1997.

[10] S. Tominetti, M. Amiotti, Getters for Flat-Panel Displays, Proc. IEEE 90 (2002) 540-558.

[11] C.-S. Park, H.-S. Tae, Y.-K. Kwon, E. G. Heo, Discharge Characteristics of AC Plasma Display Panel Prepared Using Vacuum Sealing Method, IEEE Trans. Plasma Sci. 36 (2008) 1925-1929.

[12] K. Uchida, G. Uchida, T. Yano, H. Kajiyama, T. Shinoda, PDP manufacturing system under vacuum condition, Proc. 15th Int. Disp. Workshops 3 (2008) 1899-1902.

[13] G. Pacchioni, C. Sousa, F. Illas, F. Parmigiani, P. S. Bagus, Measures of ionicity of alkaline-earth oxides from the analysis of *ab initio* cluster wave functions, Phys. Rev. B 48 (1993) 11573-11582.

[14] G. Pacchioni, J. M. Ricart, F. Illas, Ab Initio Cluster Model Calculations on the Chemisorption of CO_2 and SO_2 Probe Molecules on MgO and CaO (100) Surfaces. A Theoretical Measure of Oxide Basicity, J. Am. Chem. Soc. 116 (1994) 10152-10158.

[15] M. B. Jensen, L. G. M. Pettersson, O. Swang, U. Olsbye, CO_2 Sorption on MgO and CaO Surfaces: A Comparative Quantum Chemical Cluster Study, J. Phys. Chem. B 109 (2005) 16774-16781.

[16] R. P. Rao, Phosphors for plasma display panels, in: W. M. Yen, S. Shionoya, H. Yamamoto (Eds.), Phosphor Handbook, second ed., CRC Press, New York, 2006, pp. 745-768.

[17] R. Sato, S. Takeshita, T. Isobe, T. Sawayama, S. Niikura, Photoluminescence Properties of Green-Emitting YBO_3:Ce^{3+},Tb^{3+} Phosphor for near UV Excitation, ECS J. Solid State Sci. Tech. 1 (2012) R163-R168.

[18] A. R. Derk, H. H. Funke, J. L. Falconer, Methane Conversion to Higher Hydrocarbons by UV Irradiation, Ind. Eng. Chem. Res. 47 (2008) 6568-6572.

[19] H. Okabe, D. A. Becker, Vacuum Ultraviolet Photochemistry. VII. Photolysis of *n*-Butane, J. Chem. Phys. 39 (1963) 2549-2555.

[20] C.-W. Hu, H.-Q. Yang, N.-B. Wong, Y.-Q. Chen, M.-C. Gong, A.-M. Tian, C. Li, W.-K. Li, Theoretical Study on the Mechanism of the Reaction of CH_4 + MgO, J. Phys. Chem. A 107 (2003) 2316-2323.

[21] H.-Q. Yang, C.-W. Hu, S. Qin, Theoretical study on the reaction mechanism of CH_4 with CaO, Chem. Phys. 330 (2006) 343-348.

Chapter 5

Degradation of phosphor excitation efficiency by re-deposition of the sputtered protective layer on the phosphors

In this chapter, another mechanism for the degradation of a phosphor excitation efficiency in flat panel plasma discharge devices was investigated. It is quantitatively demonstrated that a sputtered (Mg,Ca)O protective layer is re-deposited onto the internal phosphors by prolonged aging. The results indicates that the re-deposition on the phosphors increases in proportion to the device aging time, which reduces the luminescence excitation efficiency due to the absorption of short wavelength VUV radiation by the layer. It is also shown that increasing a Xe content in discharge gas and CaO concentration of (Mg,Ca)O protective layer suppress the sputtering of the protective layer, which reduces the re-deposition on the phosphors.

5.1 Introduction

The device degradation mechanism on a luminous efficiency is also a focal issue of this chapter. Boeuf reported two degradation mechanisms associated with sputtering of the protective layer and damages of the phosphors [1]. In one mechanism, the plasma discharge burns out when the protective layer is eroded out by prolonged sputtering. In the second mechanism, the luminescence quantum efficiency is deteriorated by surface damages of the phosphors induced by both VUV irradiation and ion sputtering. Although many groups have studied these degradation mechanisms and proposed processes to improve the protective layer [2-4] and phosphors [5-7], there have been few reports scrutinizing other degradation mechanisms.

It has already been demonstrated that organic residues in the panel can be a cause of luminous degradation by consequent formation of byproducts which reduce a phosphor excitation efficiency by absorbing the shorter wavelength VUV light in Chapter 4. In present chapter, the mechanism distinct from those described above is investigated, which is luminous degradation via the re-deposition of a sputtered protective layer on the phosphors by discharge. Ha *et al.* reported that luminous degradation was suppressed by MgO deposition on phosphors prior to panel sealing due to reduced sputtering damages of the phosphors [8]. However, the same group also reported that the MgO layer on the phosphor affected the luminosity because of the absorption of VUV radiation used for the excitation. The sputtered protective layer generated in the panel as a result of discharge aging is re-deposited on the phosphors located at the other side of the device. Uchidoi also reported that the re-deposition led to a loss of the luminosity of the plasma discharge device because the re-deposition of the sputtered protective layer increases over time [9]. However, detailed quantitative analyses of the relationship between this re-deposition process and luminous degradation have yet to be performed. Moreover, the conditions for suppression of the re-deposition have never been investigated well.

The purpose of present work is to extensively study the the potential degradation mechanism due to the re-deposition of the sputtered protective layer on the phosphors based on experiments with PDPs as model Xe DBD devices. The results demonstrated that the extent of re-deposition of the sputtered protective layer on the phosphors increased as the device aged, thus reducing the luminance via the absorption of the shorter wavelength VUV radiation. The specifications of the discharge gas and the protective layer to reduce the re-deposition are also proposed by calculations.

5.2 Experimental Methods

The degradation of plasma discharge devices was assessed using 42-inch AC PDPs with HD. (Mg,Ca)O films with a thickness of 800 nm were deposited on the dielectric layer of the front panel of each experimental unit by electron beam evaporation, so as to form a protective layer. During the deposition process, the substrate was maintained at 350°C and O_2 gas was continuously flowed into the chamber at 20 sccm. The evaporation targets used to generate (Mg,Ca)O were sintered mixtures of MgO and CaO. The CaO concentration in the resulting films was experimentally determined to be approximately 9 mol% by XPS (PHI Quantera SXM, ULVAC PHI). After the (Mg,Ca)O deposition, MgO powders were dispersed on the protective layer to improve the statistical discharge delay [10]. YGB, a mixture of YBT and ZSM, and BAM were employed as red, green, and blue phosphors on the back panel, respectively. A Ne:Xe mixture was used as the discharge gas, at a pressure in the panel of 450 Torr and a Xe concentration of 20%. The specifications of the test panels used in this study are shown in Table 5.1. Panel aging tests were carried out under accelerated conditions, although the aging times reported herein correspond to the actual operational time spans. After the evaluations of the panel characteristics, the panels were dismantled and then cut into the pieces at the size of a few

Table 5.1: Specifications of the test panels used in this study.

Front Panel	
Bus electrode width	60 μm
Electrode gap	100 μm
Dielectric layer thickness	28 μm
Protective layer thickness	800 nm
Back Panel	
Address electrode width	80 μm
Dielectric layer thickness	10 μm
Barrier rib height	120 μm
Barrier rib width	50 μm
Phosphor thickness	10 μm
Pixel size	675×300 μm^2

cm^2 for the following measurement.

The amount of the sputtered protective layer re-deposited on the phosphors was estimated by XPS. The samples were excited by a monochromatic X-ray source (Al Kα line at 1486.7 eV), with irradiation at the center of each pixel using a spot size of 100 μm in diameter while monitoring an image of scanning X-ray microscope (SXM) attached to the XPS chamber. The sample surfaces were neutralized with a combination of electrons and an Ar^+ beam to suppress charging effects during the XPS measurements [11]. The photoelectron signals from the samples were detected at a take-off angle of 45° using a concentric hemispherical analyzer with a pass energy of 69 eV. Y- and Mg-related photoelectron spectra were analyzed to calculate the re-deposition amounts, employing XPS software (MultiPak, ULVAC PHI) to subtract background signals from narrow scan spectra according to the Shirley background [12]. Y and Mg signal intensities were corrected by setting the relative sensitivity factors over the regions being

assessed to 171.155 and 17.43 provided by the MultiPak software, respectively.

5.3 Results and Discussion

The test panel was aged for 2200 h and variations in the luminous intensity of the unit were evaluated. Figure 5.1 shows the relationship between the aging time span and the normalized intensities of red, green, blue, and white luminance with respect to the initial intensities. As expected, the intensities of all colors decrease with aging. In this trial, the effect of the organic residues described in Chapter 4 is excluded because the front and back panels were annealed in air enough to remove the residues prior to the panel sealing. Moreover, the degradation of the discharge intensity by prolonged aging is limited in the case of the pixel size of 42-inch HD and the dielectric layer of the front panel used in this study, confirmed by the work described in Chapter 3. The red luminance exhibits the lowest degree of degradation because the red phosphor used in the panel is relatively stable, even in response to VUV and plasma irradiation [5]. In addition to the degradation due to phosphor damages, re-deposition of the sputtered (Mg,Ca)O protective layer onto the phosphors degrades the emission efficiency.

The relationship between the loss of panel luminance and the quantity of the (Mg,Ca)O protective layer re-deposited on the phosphors during aging was assessed by dismantling panels and analyzing the surfaces of the phosphors on the back panels. Figure 5.2 shows a SXM image of the back panel sample. By monitoring the SXM image and irradiating the center regions locally in three consecutive pixels with a focused X-ray beam, the red, green, and blue pixels could independently be examined in no particular order. Analyzing the elements in these pixels with wide scan measurements enabled the corresponding colors of the pixels to be identified. The results of XPS analyses at red, green, and blue pixels on the back panels before and after aging are presented in Figs. 5.3(a)-5.3(c), respectively. Each spectrum is normalized by the

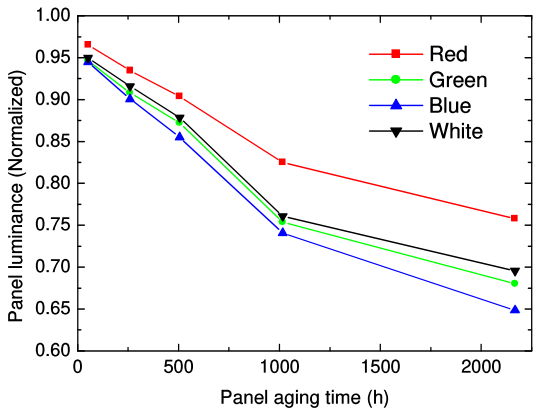

Figure 5.1: Normalized intensities of red, green, blue, and white luminance upon prolonged aging with respect to the initial intensities.

peak value of the O 1s photoelectron intensity, which is the most intense within the overall photoelectron kinetic energy range. Here, Mg peaks clearly appear in the spectra, which evidences the re-deposition of the sputtered (Mg,Ca)O protective layer onto the phosphors after aging.

The pixel color most suitable for quantifying the re-deposition amounts was subsequently determined by XPS analyses. In the case of the blue pixel, it is difficult to quantify the Mg amount because Mg is already present in the BAM, while in the green pixel spectrum, the Mg 2p and Mg 2s peaks are close to Y 4s and Zn 3p peaks arising from the YBT and ZSM, respectively. The red pixel spectrum contains a Mg 2p peak which is also close to the Y 4s peak generated by the YGB, but the Mg 2s peak is not overlapped. Therefore, the amounts of Mg in the re-deposition layer were quantified by analyzing the Mg 2s peaks produced by the red pixels. The signal intensities from the red phosphors were determined using the Y 3d peak,

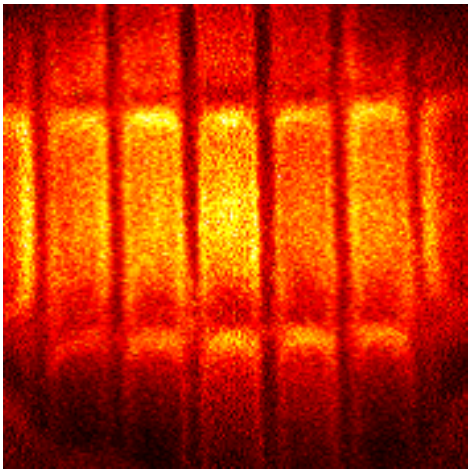

Figure 5.2: Scanning X-ray microscope image of the back panel sample.

which is not obscured by any other peaks either.

Determining the peak areas obtained from narrow scans allowed calculation of the ratios of the Mg 2s intensity from the re-deposition layer to the Y 3d intensity of the red phosphor itself (I_{Mg}/I_Y) during aging. Figure 5.4 plots the normalized red luminance with respect to the initial luminance (L/L_0) as a function of I_{Mg}/I_Y for various panel aging times. It is evident that the luminance decreased as the extent of re-deposition of the (Mg,Ca)O layer onto the red phosphors increased.

Figure 5.5 presents a schematic diagram showing photoelectron emissions during XPS analyses from the phosphors and the overlapped sputtered (Mg,Ca)O re-deposition layer. The signal intensity of Y 3d photoelectrons from the phosphors (I_Y) is decreased with increasing thickness of the re-deposition layer on the phosphor (d_R) due to attenuation on passing through the re-deposition layer. In contrast, the number of Mg 2s photoelectrons from the re-deposition layer (I_{Mg}) is increased with increasing d_R. In the region for which $d_R \lesssim 8$ nm, I_Y and I_{Mg} can be

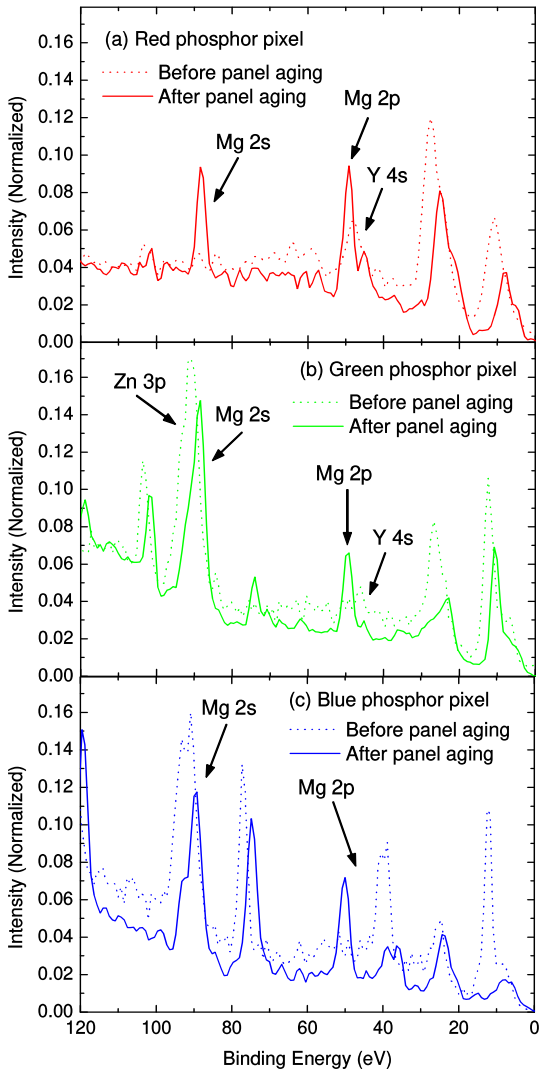

Figure 5.3: X-ray photoelectron spectra acquired from samples of the back panel before and after aging for (a) red, (b) green, and (c) blue phosphor pixels. The signal intensity in each spectrum is normalized with respect to the peak value of the O 1s photoelectron intensity.

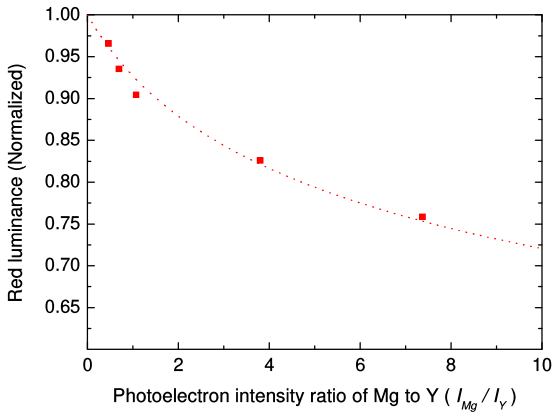

Figure 5.4: Relationship between the normalized red luminance with respect to the initial luminance and the Mg 2s to Y 3d photoelectron intensity ratio. Square data points correspond to experimental data, while the dotted line indicates the results of calculations using Eq. (5.4).

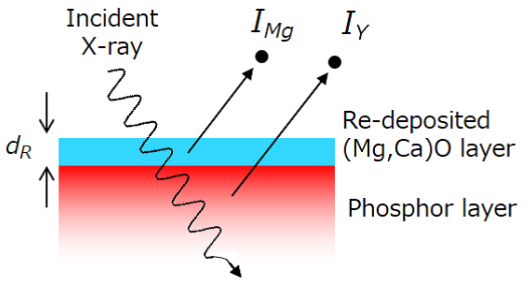

Figure 5.5: Schematic of photoelectron emissions from phosphors and the overlapped re-deposition layer generated by sputtered (Mg,Ca)O during XPS.

expressed as [13]

$$I_Y = I_Y^{bulk} \exp\left(-\frac{d_R}{A_R(E_Y)\cos\theta}\right), \tag{5.1}$$

and

$$I_{Mg} = I_{Mg}^{bulk}\left[1 - \exp\left(-\frac{d_R}{A_R(E_{Mg})\cos\theta}\right)\right], \tag{5.2}$$

where I_Y^{bulk} and I_{Mg}^{bulk} are the signal intensities of Y 3d photoelectrons from the red phosphors and Mg 2s photoelectrons from the (Mg,Ca)O layer in the bulk state, respectively, θ is the detection angle of the photoelectrons with respect to the surface normal (θ = 45° in this study), E_Y and E_{Mg} are the kinetic energies of the Y 3d and Mg 2s photoelectrons, respectively, and $A_R(E_Y)$ and $A_R(E_{Mg})$ are the attenuation lengths of photoelectrons moving through the re-deposition layer for E_Y and E_{Mg}, respectively. In this study, E_Y and E_{Mg} are similar ($\sim$ 1325 and 1395 eV based on Al Kα X-ray excitation with a 1486.7 eV line, respectively). Therefore, if it is assumed that $A_R(E_Y) \approx A_R(E_{Mg}) \approx \lambda_R$, which is the inelastic mean free path (IMFP) of electrons through the re-deposition layer, d_R can be expressed as [14]

$$d_R = \lambda_R \cos\theta \ln\left(\frac{I_Y^{bulk}}{I_{Mg}^{bulk}}\frac{I_{Mg}}{I_Y} + 1\right). \tag{5.3}$$

As particularly described in Chapter 4, the PL intensities of the red phosphor samples used in this study were degraded only minimally, even by VUV irradiation. Therefore, if it is assumed that the red luminance is proportional to the VUV excitation intensity and is affected only by modification of the VUV transmission according to changes in d_R, then L/L_0 will follow the Lambert-Beer's law, expressed as [15]

$$\frac{L}{L_0} = \exp(-\alpha_R d_R) = \exp\left[-\alpha_R \lambda_R \cos\theta \ln\left(\frac{I_Y^{bulk}}{I_{Mg}^{bulk}}\frac{I_{Mg}}{I_Y} + 1\right)\right], \tag{5.4}$$

where α_R is the VUV absorption coefficient of the re-deposition layer and $I_Y^{bulk}/I_{Mg}^{bulk} = 1.224$ (as obtained by analyzing unaged and aged back panel samples). The values calculated using

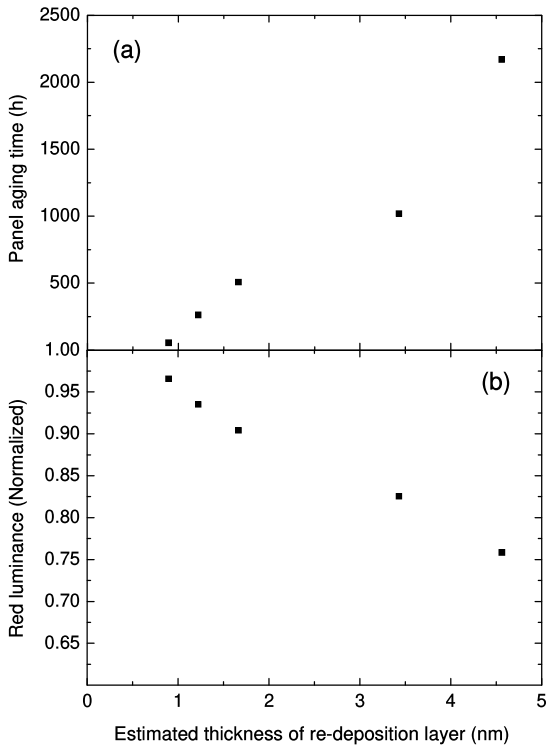

Figure 5.6: Relationships between (a) the panel aging time and (b) the normalized red luminance, and the estimated thickness of the re-deposition layer.

Eq. (5.4) are shown in Fig. 5.4 by the dotted line. The calculated results are seen to be in good agreement with the experimental data when the product of the absorption coefficient and IMFP ($\alpha_R \lambda_R$) is set to 0.137.

The IMFP values of Y 3d and Mg 2s photoelectrons passing through a MgO film can be estimated to be approximately 2.8 nm [16]. Therefore, α_R in this study is $\sim 4.89 \times 10^7$ m^{-1} based on $\alpha_R \lambda_R = 0.137$. In plasma discharge devices with Xe discharge gas, the phosphors are

excited primarily by VUV lines at 147 and 173 nm [17,18]. The sharp peak at 147 nm results from the transition from the Xe resonance level $Xe_r^*(^3P_1)$ to the ground state, while the broad peak at 173 nm arises from the excited molecular dimers $Xe_2^*(^1\Sigma_u^+)$ and $Xe_2^*(^3\Sigma_u^+)$ [19,20]. The adsorption coefficients of bulk MgO at 147 and 173 nm are approximately 4.94×10^7 m^{-1} and 4.64×10^3 m^{-1}, respectively [21]. Thus, the absorption of 147 nm VUV light by the re-deposition layer predominantly contributes to the α_R value cited above. This result indicates that degradation of the panel red luminous intensity can largely be attributed to the degradation of the VUV excitation efficiency of the phosphors due to the absorbance of 147 nm VUV light by the re-deposition layer. The 147 nm to 173 nm emission ratio is also changed upon varying the total pressure or the Xe concentration in the discharge gas [22,23]. Thus, the α_R value used above is not constant, but can be modified by changes in the discharge gas conditions.

Using Eq. (5.3), the d_R values for panels at various aging times can be calculated, and the relationships between the aging time and the normalized red luminance, and the estimated d_R are graphed in Figs. 5.6(a) and 5.6(b), respectively. Figure 5.6 demonstrates that d_R increases almost in proportion to the aging duration. Evidently, the degradation of the red luminance is correlated with increasing d_R due to a decreased VUV excitation efficiency in the shorter wavelength range. In this study, it should be noted that d_R is not increased from zero, but from a threshold thickness of ~ 0.8 nm, which is explained by previous re-deposition during pre-aging prior to the actual aging trials for stabilization of the discharge voltage.

In order to suppress the luminous degradation by the re-deposition, the sputtering rate of a protective layer during discharge must be reduced. The sputtering rate can be modified by the discharge conditions [24]. Thus, the quantitative changes in the sputtering yield of a (Mg,Ca)O protective layer by various conditions are estimated by the same procedure described in Chapter 3 [2]. Figures 5.7 and 5.8 show the estimated energy distributions $g(E)$ for Ne^+ and Xe^+

fluxes arriving at the (Mg,Ca)O layer surface at various Ne:Xe mixture ratios in discharge gas, CaO concentrations of (Mg,Ca)O protective layers, and applied voltages to the panel using Eq. (3.8) [25]. Although the approximative values in Figs. 5.7 and 5.8 are somewhat different from the actual values especially at the high-energy region due to frequent charge exchange collisions, the effects are limited for the following calculations because of much low amounts of the ions with high energy [26]. Employing the experimental values of sputtering yields $Y(E)$ of MgO and CaO described in Refs. [27,28], the calculated $Y(E)g(E)$ of MgO and CaO for Ne^+ and Xe^+ are shown in Figs. 5.9-5.12 at the same conditions in Figs. 5.7 and 5.8. Calculated results using Eqs. (3.7) and (3.10) with the various conditions are summarized in Table 5.2. Yoshino *et al.* reported that Ne:Xe gas mixture ratio modified the sputtering rate of a protective layer by the experiments [26]. However, the changes in not only a Xe content and pressure in discharge gas but also CaO concentration of a (Mg,Ca)O layer actually modify the discharge firing voltages, and thus it is difficult to change each parameter independently in the experiments. This makes the contributions of each factor impossible to be identified experimentally. Therefore, the calculated results in Table 5.2 help us to clarify the effects on the modification of the sputtering yields by changing each parameter for various conditions.

As can be seen in Table 5.2, the approaches to suppress the luminous degradation by the re-deposition is similar to those to enhance the energy efficiency. Increasing a Xe content in discharge gas clearly leads to lowering the sputtering yields due to low Xe^+ with high energy. Higher total pressure also reduces the sputtering yields due to lower Ne^+ and Xe^+ with high energy arising from more frequent charge exchange collisions. As shown in Fig. 3.9(b) in Chapter 3, CaO is less sputtered than MgO, which means that increasing CaO concentration in a (Mg,Ca)O protective layer results in decreasing the sputtering yields. On the other hand, absorption coefficients in a VUV region are larger for CaO than for MgO; approximately 1.8

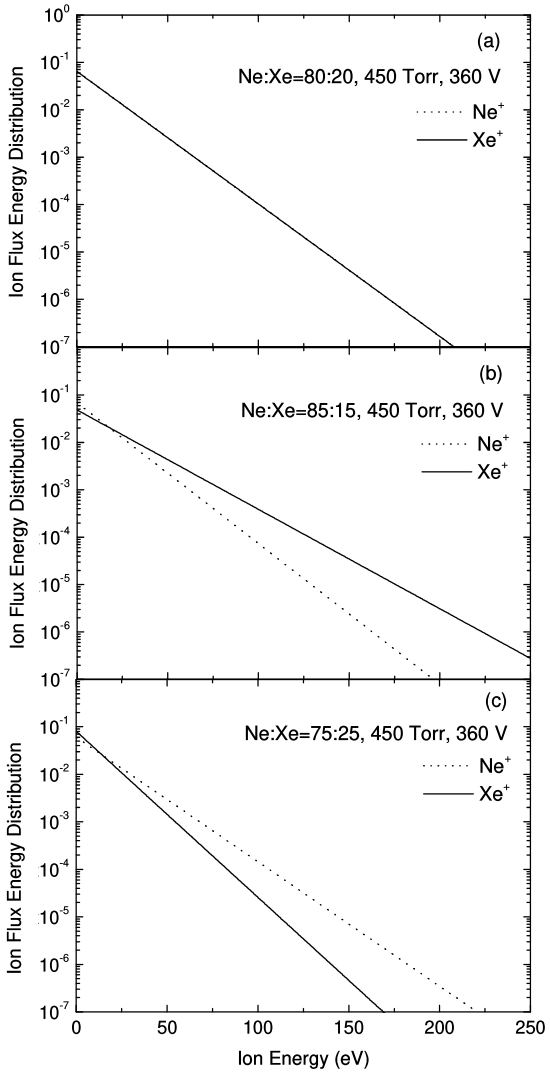

Figure 5.7: Estimated energy distributions $g(E)$ for Ne^+ and Xe^+ fluxes arriving at a (Mg,Ca)O layer surface for comparison of the changes in Xe contents in discharge gas using Eq. (3.8). (The $g(E)$ values for Ne^+ and Xe^+ in (a) are almost the same.)

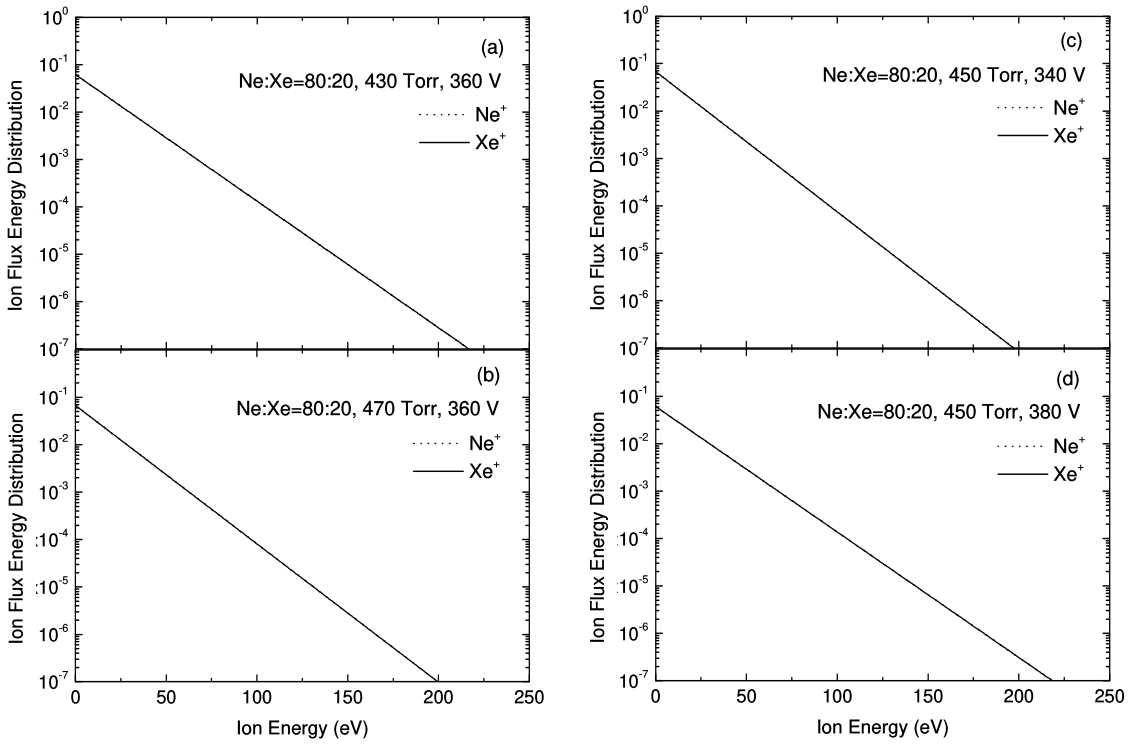

Figure 5.8: Estimated energy distributions $g(E)$ for Ne^+ and Xe^+ fluxes arriving at a (Mg,Ca)O layer surface for comparison of the changes in pressures of discharge gas and applied voltages to the panel using Eq. (3.8). (The $g(E)$ values for Ne^+ and Xe^+ in each figure are almost the same.)

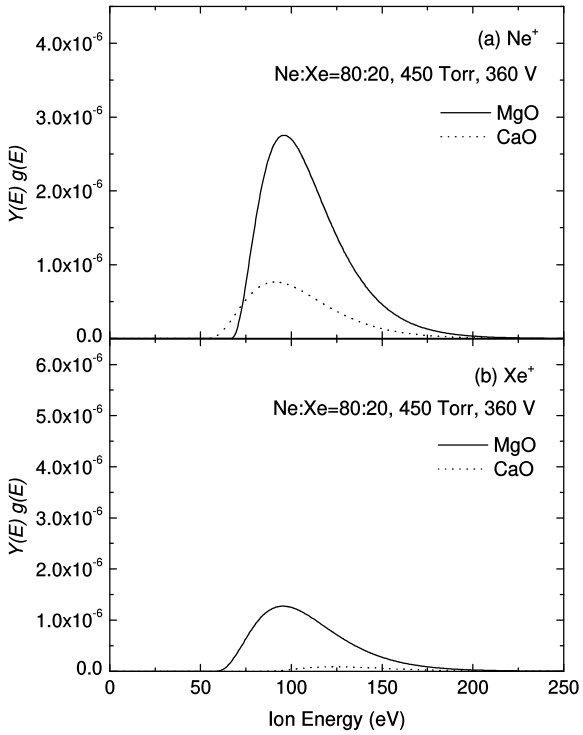

Figure 5.9: Calculated $Y(E)g(E)$ values of MgO and CaO for Ne^+ and Xe^+ at the standard condition of this trial.

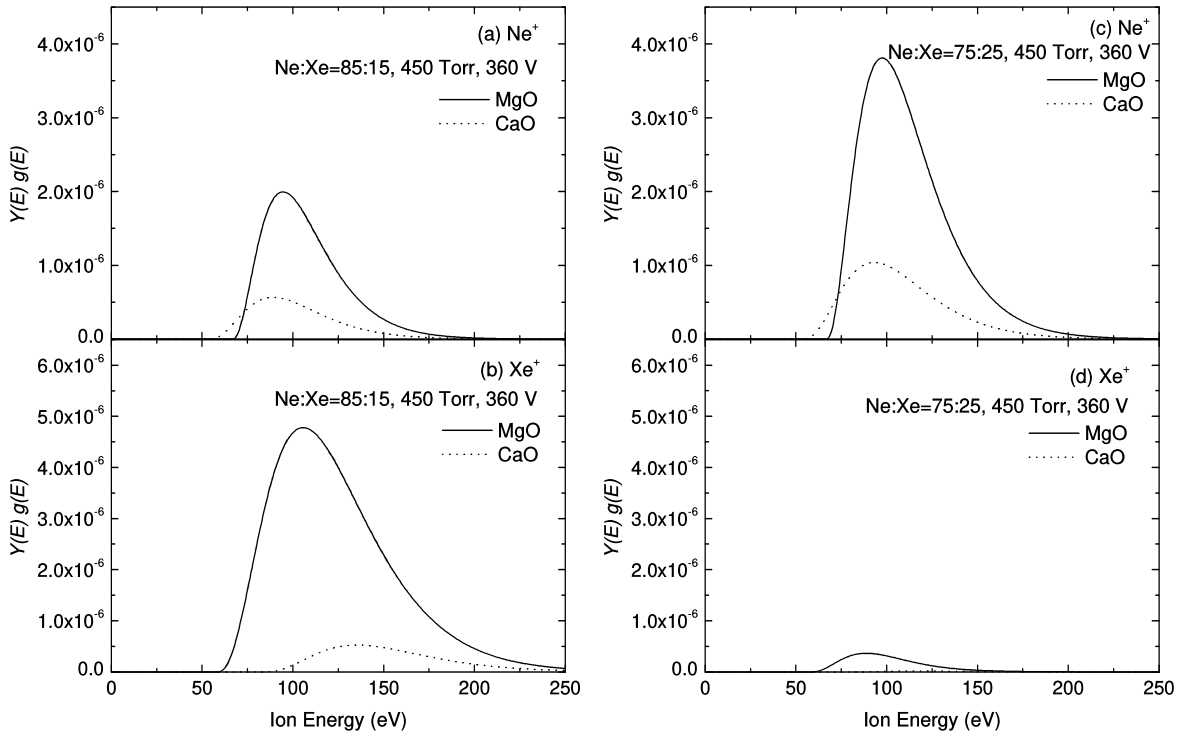

Figure 5.10: Calculated $Y(E)g(E)$ values of MgO and CaO for Ne^+ and Xe^+ for comparison of the changes in Xe contents in discharge gas.

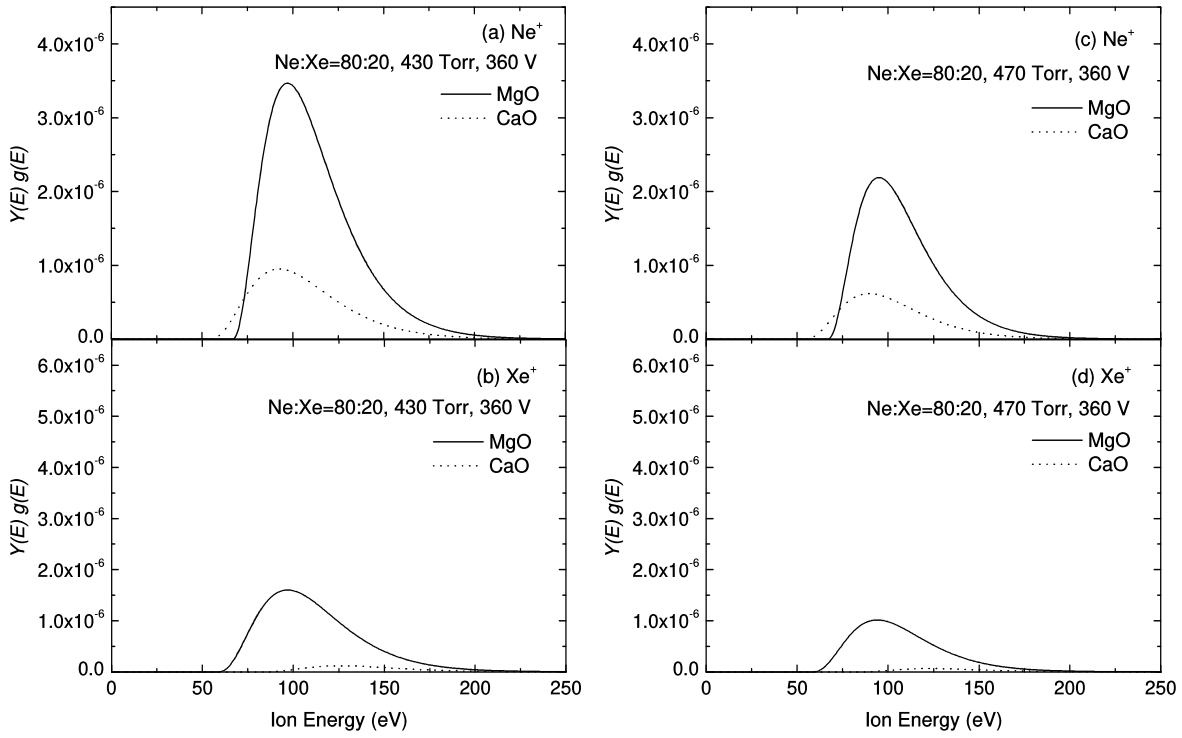

Figure 5.11: Calculated $Y(E)g(E)$ values of MgO and CaO for Ne^{+} and Xe^{+} for comparison of the changes in total pressures of discharge gas.

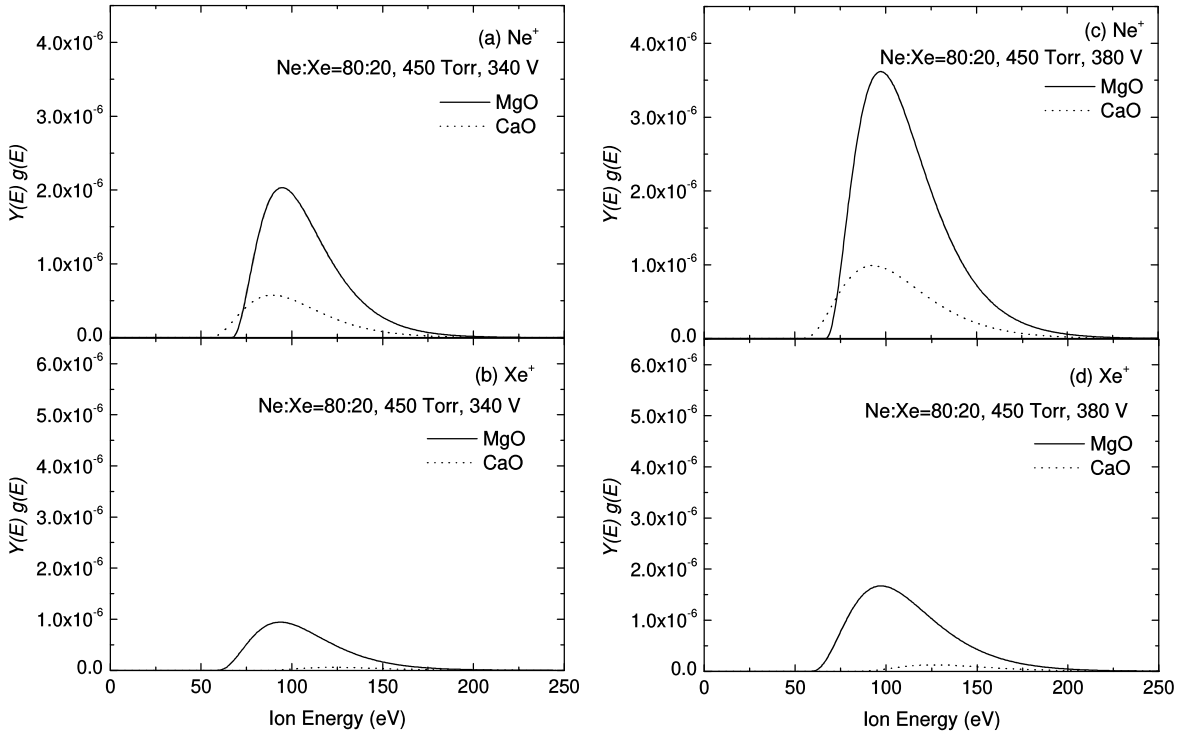

Figure 5.12: Calculated $Y(E)g(E)$ values of MgO and CaO for Ne^+ and Xe^+ for comparison of the changes in applied voltages to the panel.

Table 5.2: Calculated results of total sputtering yields for MgO, CaO, and (Mg,Ca)O using Eqs. (3.7) and (3.10). The data in the top row indicate the standard condition in this trial. Normalized γ'^{panel} values for the various conditions with respect to the γ'^{panel} value for (Mg,Ca)O at the standard condition are given in the last column.

Xe conc. (%)	Pressure (Torr)	CaO conc. (mol%)	Appl. voltage (V)	γ'^{Ne^+} ($\times 10^{-6}$)		γ'^{Xe^+} ($\times 10^{-6}$)		γ'^{panel} ($\times 10^{-6}$)			
				MgO	CaO	MgO	CaO	MgO	CaO	(Mg,Ca)O	Normalized
20	450	9	360	139	44.2	73.9	5.3	76.2	6.68	69.9	1
15	450	9	360	95.6	31	358	41.2	341	40.5	314	4.49
25	450	9	360	203	63.6	17.2	0.783	20.8	1.99	19.1	0.27
20	**430**	9	360	182	57.2	96.8	7.55	100	9.44	91.9	1.31
20	**470**	9	360	106	34.3	56.6	3.74	58.2	4.74	53.4	0.76
20	450	**6**	360	139	44.2	73.9	5.3	76.2	6.68	72	1.03
20	450	**12**	360	139	44.2	73.9	5.3	76.2	6.68	67.8	0.97
20	450	9	**340**	97.7	31.7	52	3.35	53.4	4.25	49	0.7
20	450	9	**380**	191	60	102	8.06	105	10.1	96.7	1.38

times larger in 147 nm and 2.3 times larger in 173 nm estimated by first-principle calculation [29], which may lead to larger absorption of VUV radiation by the (Mg,Ca)O re-deposition layer with higher CaO concentration. However, the degree of decreasing the sputtering yields is almost equivalent to that of increasing the absorption coefficients, i.e., in the case of changing the CaO concentration from 9 mol% to 12 mol%, approximately 3% decrease of the sputtering yield, 2% increase of the absorption coefficient of 147 nm, and 4% increase of the absorption coefficient of 173 nm. Finally, Ne^+ and Xe^+ with high energy are not excited by lowering the applied voltage to the panel, which reduces the sputtering yields of a protective layer. This means that increasing γ of a (Mg,Ca)O protective layer with high CaO concentration is also effective because of a decreased discharge firing voltage.

In addition to the above-mentioned factors, the physical properties of a protective layer also modify the sputtering rate [24]. The sputtering rate is decreased by lowering the density of the protective layer, which also leads to increasing the firing voltage [30]. This means that it is required to determine the appropriate density by changing the deposition conditions of the protective layer. Surface contaminations on the protective layer promote the forming of amorphous phase by destruction and reconstruction of the layer surface during discharge [31]. The formed amorphous phase results in increase of the sputtering rate [9]. Therefore, appropriate annealing processes to remove the impurity species are highly required for decreasing not only the discharge voltage but also the sputtering rate of the protective layer.

5.4 Conclusions

Another mechanism for the degradation of a phosphor excitation efficiency in plasma discharge devices by 147 nm VUV radiation was investigated. XPS analyses indicated that the re-deposition of a sputtered (Mg,Ca)O protective layer on the phosphors increased in proportion to the time period over which the panel was aged. Phosphor excitation was suppressed by this re-deposition layer since the layer absorbed VUV radiation, especially at shorter wavelengths. Increasing the Xe content and the CaO concentration is effective for not only improving the luminous efficiency but also suppressing the degradation of a phosphor excitation efficiency by the re-deposition.

References

[1] J. P. Boeuf, Plasma display panels: physics, recent developments and key issues, J. Phys. D: Appl. Phys. 36 (2003) R53-R79.

[2] S. J. Yoon, I. Lee, Theory of the lifetime of the MgO protecting layer in ac plasma display panels, J. Appl. Phys. 91 (2002) 2487-2492.

[3] L. C. Pitchford, J. Wang, D. Piscitelli, J. P. Boeuf, Ion and Neutral Energy Distributions to the MgO Surface and Sputtering Rates in Plasma Display Panel Cells, IEEE Trans. Plasma Sci. 34 (2006) 351-359.

[4] M. El Marsi, R. Moultif, S. Lahlou, S. Rochd, A. Dezairi, Monte Carlo simulations of MgO and $Mg(OH)_2$ thin films sputtering yields by noble-gas ion bombardment in plasma display panel PDP, Nucl. Inst. Methods Phys. Res. B 430 (2018) 72-78.

[5] C. H. Ha, B. Y. Han, J. S. Yoo, H. S. Bae, K.-W. Whang, Characteristics of Phosphor Degradation in AC-Driven Plasma Display Panels, J. Electrochem. Soc. 155 (2008) J230-J234.

[6] K. Sawada, S. Adachi, Unique photoluminescence degradation/recovery phenomena in trivalent ion-activated phosphors, J. Appl. Phys. 118 (2015) 103106-1-7.

[7] L. Amidani, K. Korthout, J. J. Joos, M. van der Linden, H. F. Sijbom, A. Meijerink, D. Poelman, P. F. Smet, P. Glatzel, Oxidation and Luminescence Quenching of Europium in $BaMgAl_{10}O_{17}$ Blue Phosphors, Chem. Mater. 29 (2017) 10122-10129.

[8] C. H. Ha, J. S. Kim, D. C. Jeong, K. W. Whang, The improvement of discharge characteristics and lifetime of alternate current plasma display panel by MgO deposition on the phosphor, J. Appl. Phys. 96 (2004) 4807-4810.

[9] M. Uchidoi, Critical Aspects of the Plasma Display Panel Manufacturing Process, IEEE Trans. Plasma Sci. 34 (2006) 287-293.

[10] M. Amatsuchi, A. Hirota, H. Lin, T. Naoi, E. Otani, H. Taniguchi, K. Amemiya, Discharge Time Lag Shortening by Using a New Material Layer in AC PDP, Proc. 12th Int. Disp. Workshops 1 (2005) 435-438.

[11] P. E. Larson, M. A. Kelly, Surface charge neutralization of insulating samples in x-ray photoemission spectroscopy, J. Vac. Sci. Technol. A 16 (1998) 3483-3489.

[12] D. A. Shirley, High-Resolution X-Ray Photoemission Spectrum of the Valence Bands of Gold, Phys. Rev. B 5 (1972) 4709-4714.

[13] M. Seah, L. D. Chiffre, Surface and Interface Characterization, in: H. Czichos, T. Saito, L. Smith (Eds.), Springer Handbook of Materials Measurement Methods, Springer Science+Business Media Inc., Würzburg, 2006, pp. 229-280.

[14] A. Jablonski, Photoelectron emission from thin overlayers, J. Electron Spectrosc. Relat. Phenom. 185 (2012) 498-508.

[15] G. Chartier, Introduction to Optics, Springer Science+Business Media Inc., New York, 2005, pp. 351-377.

[16] S. Gurban, G. Gergely, J. Toth, D. Varga, A. Jablonski, M. Menyhard, Experimental determination of the inelastic mean free path (IMFP) of electrons in selected oxide films applying surface excitation correction, Surf. Interface Anal. 38 (2006) 624-627.

[17] D. Zhu, L. Song, X. Zhang, H. Kajiyama, Vacuum ultra-violet emission of plasma discharges with high Xe partial pressure using a cathode protective layer with high secondary electron emission, J. Appl. Phys. 115 (2014) 063302-1-7.

[18] H. Loukil, A. Belasri, K. Khodja, Z. Harrache, Theoretical Kinetics Investigation of Xenon Dielectric Barrier Discharge for Excimer Lamp, IEEE Trans. Plasma Sci. 42 (2014) 712-720.

[19] Y. Ikeda, J. P. Verboncoeur, P. J. Christenson, C. K. Birdsall, Global modeling of a dielectric barrier discharge in Ne-Xe mixtures for an alternating current plasma display panel, J. Appl. Phys. 86 (1999) 2431-2441.

[20] K. Tachibana, S. Feng, T. Sakai, Spatiotemporal behaviors of excited Xe atoms in unit discharge cell of ac-type plasma display panel studied by laser spectroscopic microscopy, J. Appl. Phys. 88 (2000) 4967-4974.

[21] D. M. Roessler, D. R. Huffman, Magnesium Oxide (MgO), in: E. D. Palik (Ed.), Handbook of Optical Constants of Solids II, Academic Press, Orlando, 1991, pp. 919-955.

[22] J. H. Seo, H. S. Jeong, J. Y. Lee, C. K. Yoon, J. K. Kim, K.-W. Whang, Vacuum ultraviolet emission characteristics from He-Ne-Xe gas discharge in an alternating current plasma display panel cell, J. Appl. Phys. 88 (2000) 1257-1262.

[23] K.-H. Bu, T. H. Shin, B. K. Kim, J. S. Choi, J. D. Kim, Influence of He-Ne-Xe gas composition on vacuum ultraviolet ray spectra in plasma-display panels, J. Soc. Inf. Disp. 10 (2002) 157-162.

[24] S. Ho, T. Tamakoshi, M. Ikeda, Y. Mikami, K. Suzuki, Net sputtering rate due to hot ions in a Ne-Xe discharge gas bombarding an MgO layer, J. Appl. Phys. 109 (2011) 084908-1-14.

[25] W. D. Davis, T. A. Vanderslice, Ion Energies at the Cathode of a Glow Discharge, Phys. Rev. 131 (1963) 219-228.

[26] K. Yoshino, K. Nomoto, M. Goto, R. Murai, T. Tsujita, M. Terauchi, Y. Morita, M. Nishitani, M. Kitagawa, Effects of Ne/Xe Gas Mixture Ratio on Sputtering Rate of MgO Protective Layer, Proc. 18th Int. Disp. Workshops 2 (2011) 689-692.

[27] K. Hine, S. Yoshimura, K. Ikuse, M. Kiuchi, J. Hashimoto, M. Terauchi, M. Nishitani, S. Hamaguchi, Experimental evaluation of MgO sputtering yields by monochromatic Ne, Kr, or Xe ion beams, Thin Solid Films 517 (2008) 835-840.

[28] S. Yoshimura, K. Hine, M. Kiuchi, J. Hashimoto, M. Terauchi, Y. Honda, M. Nishitani, S. Hamaguchi, Experimental evaluation of CaO, SrO and BaO sputtering yields by Ne^+ or Xe^+ ions, J. Phys. D: Appl. Phys. 44 (2011) 255203-1-5.

[29] M. Dadsetani, R. Beiranvand, Optical properties of alkaline-earth metal oxides from first principles, Solid State Sci. 11 (2009) 2099-2105.

[30] M. J. Lee, S. Y. Park, S. G. Kim, H. J. Kim, S. H. Moon, J. K. Kim, Effect of stress and density on the electrical and physical properties of MgO protecting layer for alternating current-plasma display panels, J. Vac. Sci. Technol. A 23 (2005) 1192-1196.

[31] M. Kubo, K. Serizawa, H. Kikuchi, R. Sahnoun, M. Koyama, H. Tsuboi, N. Hatakeyama, A. Endou, H. Takaba, C. A. D. Carpio, H. Kajiyama, T. Shinoda, A. Miyamoto, Effect of surface contamination on destruction and recrystallization dynamics of MgO protecting layer in plasma display panel by molecular dynamics simulation method, Proc. 14th Int. Disp. Workshops 2 (2007) 787-790.

Chapter 6

Overall Conclusion

In this thesis, the characteristics of plasma discharge devices with high-γ (Mg,Ca)O protective layers and high Xe contents in discharge gas were investigated. The mechanisms for the degradation of a discharge voltage, a discharge property, and a luminous efficiency were quantitatively investigated to realize the performance improvement. In addition, appropriate annealing processes and device specifications to suppress the degradation were demonstrated by experiments and calculations.

In Chapter 2, the degradation of a discharge voltage for (Mg,Ca)O protective layers in plasma discharge devices was investigated. It is shown that the variation in the discharge voltage was much larger than that of a conventional MgO protective layer. The quantitative relationship between the Ca carbonation ratio in the protective layer and the discharge voltage indicates that the increase of the discharge voltage is due to carbonation of Ca. In order to suppress the progression of the carbonation, dry air is more acceptable for exposure after the deposition than humid air. The carbonated species in (Mg,Ca)O are not decarbonated only by annealing in air at an accessible temperature. The additional annealing in vacuum after annealing in air is required to realize both the decarbonation of (Mg,Ca)O films and the removal of organic residues on the protective layer during production.

In Chapter 3, the modification of the discharge area in flat panel plasma discharge devices with (Mg,Ca)O protective layers by prolonged aging was investigated. Shrinkage of the dis-

charge area was observed after aging, which resulted in the decreased discharge intensity. The increase of local Ca concentration by preferential sputtering of MgO leads to the shrinkage due to the locally modified γ distribution in the pixel. By adjusting the characteristics of the dielectric layer under the protective layer, the discharge modification during prolonged aging due to variations in the initial discharge area are also demonstrated. The reduced permittivity of the dielectric layer expanded the discharge area, which leads to the long-life operation of the plasma discharge devices by the suppression of the degradation of the discharge intensity.

In Chapter 4, the mechanism for the degradation of a phosphor excitation efficiency in plasma discharge devices with (Mg,Ca)O protective layers was investigated. By continuous 147 nm VUV irradiation, the luminance of organic-contaminated sample is strongly decreased in response to 147 nm VUV excitation, but not in response to 173 nm VUV excitation. It is suggested that VUV-irradiated organic resides are converted to substances which absorb VUV light in the shorter wavelength range. Not only the discharge voltage but also the phosphor excitation efficiency are shown to be degraded by organic compounds in the panel by prolonged aging. The degradation by the organic residues should be suppressed by appropriate annealing of the panels especially in the case of (Mg,Ca)O protective layers owing to high reactive property for organic compounds.

In Chapter 5, another mechanism for the degradation of a phosphor excitation efficiency in plasma discharge devices with (Mg,Ca)O protective layers was investigated. During aging, the sputtered (Mg,Ca)O layer is re-deposited onto the internal phosphors in proportion to the aging time. The re-deposition layer reduces the phosphor excitation efficiency due to the absorption of short wavelength VUV radiation by the layer. The specifications of the discharge gas and the protective layer for realization of the long-life devices are also investigated by the calculations. Increasing a Xe content in discharge gas and a CaO concentration of a (Mg,Ca)O protective

layer are proposed to reduce the the re-deposition of the protective layer and suppress the degradation of the phosphor excitation efficiency, which are compatible with the enhancement of the energy efficiency of plasma discharge devices.

Overall, accomplishments of this thesis will lead to further improvement and reliability of the performance of plasma discharge devices with (Mg,Ca)O protective layers. The proposed approaches can also be applied for other upcoming candidates of higher-γ complex oxide protective layers such as (Mg,Sr)O, (Mg,Ca,Sr)O, (Mg,Ba)O, and (Sr,Ca)O. The obtained results should be valuable during the further developments and practical applications of these complex oxide protective layers having high-γ values for not only plasma displays but also other plasma discharge devices together with a low discharge voltage, a long lifespan, and an increased luminous efficiency.

Acknowledgments

I would like to express my deepest gratitude to Prof. Minoru Fujii (Graduate School of Engineering, Kobe University) for the detailed reading of this thesis and the useful discussions leading this thesis to valuable one. His excellent tutelage to complete my bachelor, master, and doctoral degrees creates a strong foundation for my career as a professional research engineer in material science and applied physics.

I would like to give my deepest appreciation to Dr. Yukihiro Morita (Technology Innovation Division, Panasonic Corporation, and Graduate School of Engineering, Osaka University) for his heartfelt supports and instructive discussions. His empathetical assistance increases the quality of this thesis, and offers mental and spiritual sustenance for completion of my doctoral degree.

This work was mainly carried out by the PDP Advanced Development Group, PDP Devices Business Unit, Visual Products and Display Devices Business Group, AVC Networks Company of the Panasonic Corporation under the strong management and leadership by Dr. Masatoshi Kitagawa and Mr. Ryuichi Murai. The research was partly supported by the PDP Materials Technology Group, PDP Devices Business Unit, Visual Products and Display Devices Business Group, AVC Networks Company, the AVC Devices Development Center, Technology Planning and Development Center, AVC Networks Company, the Image Devices Development Center, Corporate R&D Division, and the Production Engineering Laboratory, Manufacturing Technology and Engineering Division of the Panasonic Corporation. I wish to express my deep gratitude

to my ex-supervisors in the PDP Advanced Development Group, Dr. Tetsuo Kawakita, Dr. Hiroyuki Kado, Dr. Masashi Goto, and Mr. Hiroyuki Ajiki, for their excellent technical assistance on the research and development of plasma discharge devices. I deeply thank all ex-coworkers in the PDP Advanced Development Group and the related departments for their encouraging supports and useful discussions, especially to Dr. Kyohei Yoshino, Dr. Takehiro Zukawa, Dr. Takuji Tsujita, Mr. Tasuku Ishibashi, Mr. Hai Lin, Dr. Hikaru Nishitani, Mr. Jun Hashimoto, and Mrs. Yukako Doi.

Furthermore, I greatly appreciate the understanding and cooperation from all supervisors and coworkers in the Optical System Development Department, Sensing Solution Development Center, Engineering Division, Automotive & Industrial Systems Company, the Indoor Air Quality Research Laboratory and the Smart Optics Research Laboratory, Institute for Sensors and Devices, Technology Innovation Division, and the related departments of the Panasonic Corporation. I am also very grateful for the warm welcome by all members in the Mesoscopic Materials Research Laboratory, Department of Electrical and Electronic Engineering, Graduate School of Engineering, Kobe University.

Finally, I am deeply indebted to my wife Miyuki, and to all my family and friends for their endless support and hearty encouragement until now.

List of Achievements

Journal Papers

* Papers relevant to this thesis.

[1] Kenji Imakita, Minoru Fujii, Toshihiro Nakamura, Satoru Miura, Eiji Takeda, and Shinji Hayashi, "Enhancement of Radiative Recombination Rate of Excitons in Si Nanocrystals on Au Film", Japanese Journal of Applied Physics, Vol. 45, No. 8A, pp. 6132-6136 (2006).

[2] Eiji Takeda, Toshihiro Nakamura, Minoru Fujii, Satoru Miura, and Shinji Hayashi, "Surface Plasmon Polariton Mediated Photoluminescence from Excitons in Silicon Nanocrystals", Applied Physics Letters, Vol. 89, pp. 101907-1-3 (2006).

[3] Eiji Takeda, Minoru Fujii, Toshihiro Nakamura, Yugo Mochizuki, and Shinji Hayashi, "Enhancement of Photoluminescence from Excitons in Silicon Nanocrystals via Coupling to Surface Plasmon Polaritons", Journal of Applied Physics, Vol. 102, pp. 023506-1-6 (2007).

[4] * Eiji Takeda, Takehiro Zukawa, Takuji Tsujita, Kyohei Yoshino, and Yukihiro Morita, "Annealing process for recovery of carbonated (Mg,Ca)O protective layer for plasma discharge device", Japanese Journal of Applied Physics, Vol. 57, No. 9, pp. 096001-1-7 (2018). (Chapter 2)

[5] * Eiji Takeda, Takehiro Zukawa, Tasuku Ishibashi, Kyohei Yoshino, Yukihiro Morita, and Minoru Fujii, "Mechanisms for the degradation of phosphor excitation efficiency by short wavelength vacuum ultraviolet radiation in plasma discharge devices", Journal of Physics and Chemistry of Solids, Vol. 124, pp. 274-280 (2019). (Chapters 4 and 5)

[6] * Eiji Takeda, Takehiro Zukawa, Tasuku Ishibashi, Kyohei Yoshino, Naoki Kosugi, Yukihiro Morita, and Minoru Fujii, "Shrinkage and expansion of discharge areas in plasma discharge devices having complex oxide protective layers", Journal of Physics and Chemistry of Solids, Vol. 130, pp. 172-179 (2019). (Chapter 3)

Conference Papers

[1] Kimihisa Matsumoto, Eiji Takeda, Kenji Imakita, Minoru Fujii, and Shinji Hayashi, "Luminescence Properties of Er and Si Nanoparticles Co-doped Aluminum Silicate Thin Films", Transactions of the Materials Research Society of Japan, Vol. 32, No. 2, pp. 441-443 (2007).

[2] (Invited Paper) Hiroshi Hayashi, Yoshiaki Nakazaki, Tomoaki Izumi, Atsushi Sasaki, Tetsuroh Nakamura, Eiji Takeda, Tohru Saitoh, Masashi Goto, and Hiroyoshi Takezawa, "Highly Reliable InGaZnO Thin Film Transistor Backplane for 55-inch 4K2K Organic Light-Emitting Diode Display", SID International Symposium Digest of Technical Papers, Vol. 45, Issue 1, pp. 853-856 (2014).

Presentations (International Conference)

[1] Kimihisa Matsumoto, Kenji Imakita, Eiji Takeda, Minoru Fujii, and Shinji Hayashi, "Effects of Al doping on luminescence properties of SiO_2 thin films containing Er and Si nanoparticles", The 23th International Conference on Defects in Semiconductors, Abstract p. 338, Awaji Yumebutai International Conference Center, Awaji Island, Hyogo, Japan, July 24-29, 2005, Poster Presentation.

[2] Minoru Fujii, Kenji Imakita, Toshihiro Nakamura, Satoru Miura, Eiji Takeda, and Shinji Hayashi, "Enhancement of Radiative Recombination Rate of Excitons in Si Nanocrystals on Au Thin Films", Materials Research Society 2005 fall meeting, Symposium P "Quantum Confined Semiconductor Nanostructures -Fabrication, Physical Properties, and Application", P9.23, Abstract p. 377, Hynes Convention Center, Boston, Massachusetts, USA, November 28 - December 02, 2005, Oral Presentation.

[3] Eiji Takeda, Toshihiro Nakamura, Minoru Fujii, Satoru Miura, and Shinji Hayashi, "Surface Plasmon Polariton Mediated Photoluminescence from Excitons in Silicon Nanocrystals", 9th International Conference on Near-field Optics, Nanophotonics & Related Techniques, Session Tu2 "Quantum systems A", Tu2-4, Abstract p. 111, Swiss Federal Institute of Technology in Lausanne, Lausanne, Switzerland, September 10-15, 2006, Oral Presentation.

[4] (Invited Talk) Hiroshi Hayashi, Yoshiaki Nakazaki, Tomoaki Izumi, Atsushi Sasaki, Tetsuroh Nakamura, Eiji Takeda, Tohru Saitoh, Masashi Goto, and Hiroyoshi Takezawa, "Highly Reliable InGaZnO TFT Backplane for 55-in. 4K × 2K OLED Display", SID Display Week 2014, Session 58 "OLED TV II", 58.3, Digest pp. 853-856, San Diego Convention Center, San Diego, California, USA, June 1-6, 2014, Oral Presentation.

Presentations (Domestic Conference)

[1] 武田 英治, 今北 健二, 藤井 稔, 林 真至,“ Al と Si と Er^{3+} を含む SiO_2 薄膜の光学特性”, 第 52 回応用物理学関係連合講演会, 予稿集第 3 分冊 p. 1631, 埼玉大学, 2005 年 3 月 29 日～4 月 1 日, Oral Presentation.

[2] 武田 英治, 今北 健二, 藤井 稔, 林 真至,“ Er と Si ナノ粒子を同時ドープした SiO_2 薄膜への Al 添加効果”, 第 1 回シリコン・フォトニクス研究会（電子情報通信学会）, 予稿集 pp. 11-15, 電気通信大学スカイオフィス, 2005 年 4 月 22 日, Oral Presentation.

[3] 松本 公久, 武田 英治, 今北 健二, 藤井 稔, 林 真至,“Luminescence properties of Er and Si nanoparticles co-doped aluminum silicate thin film”, 第 17 回日本 MRS 学術シンポジウム, 予稿集 p. 155, 日本大学, 2006 年 12 月 8 日～12 月 10 日, Oral Presentation.

[4] 望月 有吾, 武田 英治, 中村 俊博, 藤井 稔, 林 真至,“ 表面プラズモンポラリトン励起による Si ナノ結晶の発光増強”, 第 54 回応用物理学関係連合講演会, 予稿集第 3 分冊 p. 1100, 青山学院大学 相模原キャンパス, 2007 年 3 月 27 日～3 月 30 日, Oral Presentation.

[5] (Invited Talk) 藤井 稔, 中村 俊博, 武田 英治, 三浦 智, 乾 真規, 望月 有吾, 石倉 伸幸, 林 真至,“ 表面プラズモンポラリトン励起によるシリコンナノ結晶の発光増強”, ナノオプティクス研究グループ第 16 回研究討論会, 神戸大学瀧川記念学術交流会館, 2007 年 7 月 13 日～7 月 14 日, Oral Presentation.

Patents (PCT International Application)

[1] Jun Hashimoto, Masashi Goto, Eiji Takeda, and Shimamura Takayuki,“ Plasma display panel having a plurality of aggregated particles attached to a protective layer at a face

confronting a discharge space formed between a first substrate and a second substrate ”, PCT/JP2009/006834, December 15, 2008.

[2] Eiji Takeda, Takuji Tsujita, and Masashi Goto, “Method for producing plasma display panel”, PCT/JP2011/001525, March 26, 2010.

[3] Eiji Takeda, Takuji Tsujita, Jun Hashimoto, and Masashi Goto, “Method for producing plasma display panel”, PCT/JP2011/001526, March 26, 2010.

[4] Hai Lin, Takehiro Zukawa, Eiji Takeda, Tasuku Ishibashi, Kyohei Yoshino, Kazuya Nomoto, and Takuji Tsujita, “Method for producing plasma display panel”, PCT/JP2011/001527, March 26, 2010.

[5] Eiji Takeda, Takuji Tsujita, Jun Hashimoto, and Masashi Goto, “Method for producing plasma display panel”, PCT/JP2011/001528, March 26, 2010.

[6] Eiji Takeda, and Tohru Saitoh, “Method of evaluating thin-film transistor, method of manufacturing thin-film transistor, and thin-film transistor”, PCT/JP2014/003395, September 3, 2013.

[7] Tomoaki Izumi, Mami Nonoguchi, Eiji Takeda, and Tatsuya Yamada, “Thin film transistor and method for manufacturing same”, PCT/JP2014/003638, October 10, 2013.

[8] Eiji Takeda, and Takahiro Kawashima, “Method for producing thin film transistor”, PCT/JP2014/003507, October 24, 2013.

[9] Seiji Imanaka, Eiji Takeda, and Takahiro Kawashima, “Sputtering apparatus”, PCT/JP2014/003392, November 14, 2013.

[10] Yuuki Abe, Kazuhiro Yokota, Yasuharu Shinokawa, Ko Sugano, and Eiji Takeda, “Organic EL element and method for manufacturing organic EL element”, PCT/JP2015/002533, May 21, 2014.

[11] Atsushi Sasaki, Eiji Takeda, Masashi Goto, and Yuta Sugawara, “Method for manufacturing thin film transistor”, PCT/JP2015/004989, October 10, 2014.

[12] Eiji Takeda, and Hitoshi Noguchi, “Laser radar”, PCT/JP2018/048174, May 8, 2018.

[13] Hitoshi Noguchi, and Eiji Takeda, “Laser radar”, PCT/JP2018/048175, May 8, 2018.

Patents (Domestic Application)

[1] 橋本 潤, 後藤 真志, 武田 英治, 島村 隆之, “プラズマディスプレイパネル”, 特願 2008-317942, 2008 年 12 月 15 日.

[2] 島村 隆之, 橋本 潤, 武田 英治, 頭川 武央, 吉野 恭平, “プラズマディスプレイパネル”, 特願 2009-194002, 2009 年 8 月 25 日.

[3] 石橋 将, 吉野 恭平, 頭川 武央, 林 海, 阿部 裕之, 辻田 卓司, 武田 英治, “プラズマディスプレイパネル”, 特願 2010-59038, 2010 年 3 月 16 日.

[4] 石橋 将, 吉野 恭平, 頭川 武央, 林 海, 阿部 裕之, 辻田 卓司, 武田 英治, “プラズマディスプレイパネル”, 特願 2010-59039, 2010 年 3 月 16 日.

[5] 石橋 将, 吉野 恭平, 頭川 武央, 林 海, 阿部 裕之, 辻田 卓司, 武田 英治, “プラズマディスプレイパネル”, 特願 2010-59040, 2010 年 3 月 16 日.

[6] 石橋 将, 吉野 恭平, 頭川 武央, 林 海, 阿部 裕之, 辻田 卓司, 武田 英治, “プラズマディスプレイパネル”, 特願 2010-59041, 2010 年 3 月 16 日.

[7] 石橋 将, 吉野 恭平, 頭川 武央, 林 海, 阿部 裕之, 辻田 卓司, 武田 英治, “プラズマディスプレイパネル”, 特願 2010-59042, 2010 年 3 月 16 日.

[8] 武田 英治, 西谷 輝, “プラズマディスプレイパネルの製造方法”, 特願 2010-131705, 2010 年 6 月 9 日.

[9] 武田 英治, 辻田 卓司, 島村 隆之, 後藤 真志, 河原崎 秀司, “プラズマディスプレイパネルの製造方法”, 特願 2010-207508, 2010 年 9 月 16 日.

[10] 武田 英治, 安喰 博之, “蛍光体材料およびそれを用いたプラズマディスプレイパネル”, 特願 2011-127877, 2011 年 6 月 8 日.

[11] 武田 英治, 安喰 博之, “プラズマディスプレイパネル”, 特願 2011-188408, 2011 年 8 月 31 日.

[12] 頭川 武央, 吉野 恭平, 大江 良尚, 河原崎 秀司, 武田 英治, 林 海, “プラズマディスプレイパネル”, 特願 2012-15168, 2012 年 1 月 27 日.

[13] 安喰 博之, 秋山 利幸, 武田 英治, 泉 知明, “プラズマディスプレイパネル”, 特願 2012-199149, 2012 年 9 月 11 日.

[14] 武田 英治, 佐々木 厚, 原田 健史, 林 海, 三浦 正範, 川島 孝啓, “薄膜トランジスタ”, 特願 2014-183647, 2014 年 9 月 9 日.

[15] 原田 健史, 武田 英治, 川島 孝啓, “薄膜トランジスタ及びその製造方法”, 特願 2014-223591, 2014 年 10 月 31 日.

[16] 武田 英治, 岡本 庄司, “液滴吐出ヘッド”, 特願 2017-012696, 2017 年 1 月 27 日.

[17] 武田 英治, 野口 仁志, 村上 公博, “レーザレーダ”, 特願 2018-226854, 2018 年 12 月 3 日.

[18] 野口 仁志, 武田 英治, 張替 貴聖, 高山 了一, “レーザレーダ”, 特願2019-018812, 2019年2月5日.

[19] 野口 仁志, 武田 英治, 張替 貴聖, 高山 了一, “レーザレーダ”, 特願2019-024095, 2019年2月14日.

[20] 武田 英治, “バイオセンサ”, 特願2019-124407, 2019年7月3日.

Awards

[1] 武田 英治, KTC 竹水会 優秀論文賞, “修士論文題目：表面プラズモン励起による Si ナノ結晶の発光増強に関する研究”, 2007年3月23日.

[2] 野口 康幸, 吉野 恭平, 大植 利泰, 橋本 伸一郎, 辻田 卓司, 頭川 武央, 前田 憲輝, 林 海, 土居 由佳子, 石橋 将, 三浦 正範, 武田 英治, Hoang Minh Hiep, 阿部 裕之, 豊田 誠司, 平岡 知己, 天野 邦晶, 西谷 輝, パナソニック株式会社 AVC ネットワークス社 映像・ディスプレイデバイス事業グループ 2008年度第3四半期チャレンジ表彰団体賞, “PDP における新保護膜材料の基本技術を確立しパネルの大幅な省電力化を実現した功績”, 2009年2月2日.

Doctor Thesis, Kobe University

“ Development of Highly Reliable Plasma Discharge Devices with (Mg,Ca)O Protective Layers

((Mg,Ca)O 保護膜を用いたプラズマ放電デバイスの信頼性向上に関する研究) ”, 155 pages

Submitted on July, 16, 2019

The date of publication is printed in cover of repository version published in Kobe University

Repository Kernel.